European Commission

JRC SCIENCE AND POLICY REPORTS

Neutron Resonance Spectroscopy for the Characterisation of Materials and Objects

P. Schillebeeckx
B. Becker
H. Harada
S. Kopecky

2014

Report EUR 26848 EN

Joint Research Centre

European Commission
Joint Research Centre
Institute for Reference Materials and Measurements

Contact information
Peter Schillebeeckx
Address: Joint Research Centre, Retieseweg 111, 2440 Geel, Belgium
E-mail: Peter.Schillebeeckx@ec.europa.eu
Tel.: +32 (0)14 571 475

https://ec.europa.eu/jrc

JRC91818

EUR 26848 EN

ISBN 978-92-79-41179-3 (PDF)
ISBN 978-92-79-41180-9 (print)

ISSN 1831-9424 (online)
ISSN 1018-5593 (print)

doi: 10.2787/98278

Luxembourg: Publications Office of the European Union, 2014

Abstract

The use of neutron resonance spectroscopy to investigate and study properties of materials and objects is the basis of neutron resonance transmission analysis (NRTA) and neutron resonance capture analysis (NRCA). NRTA and NRCA are non-destructive methods to determine the elemental and isotopic composition without the need of any sample preparation and resulting in a negligible residual activity. The basic principles of NRTA and NRCA are explained. The use of NRTA and NRCA to determine the elemental composition of archaeological objects and to characterise nuclear materials is reviewed. Other applications of neutron resonance spectroscopy such as imaging, detection of explosives and drugs and thermometry are briefly discussed. A combination of NRTA and NRCA, referred to as Neutron Resonance Densitometry (NRD), is presented as a non-destructive method to quantify nuclear material, in particular the amount of special nuclear material in particle-like debris of melted fuel that is formed in severe nuclear accidents. Finally the importance of accurate nuclear resonance parameters for these applications is discussed and the performance of NRTA for the characterisation of nuclear material in the presence of matrix material is assessed.

Neutron Resonance Spectroscopy for the Characterisation of Materials and Objects

P. Schillebeeckx[a], B. Becker[a], H. Harada[b] and S. Kopecky[a]

[a] European Commission, Joint Research Centre, Institute for Reference Materials and Measurements, Retieseweg 111, B – 2440 Geel, Belgium

[b] Japan Atomic Energy Agency, Tokai-mura, Naka-gun, Ibarkai 319 – 1195, Japan

Executive Summary

The use of neutron resonance spectroscopy to investigate and study properties of materials and objects is the basis of neutron resonance transmission analysis (NRTA) and neutron resonance capture analysis (NRCA). NRTA and NRCA are non-destructive methods to determine the elemental and isotopic composition without the need of any sample preparation and resulting in a negligible residual activity. The basic principles of NRTA and NRCA are explained. The use of NRTA and NRCA to determine the elemental composition of archaeological objects and to characterize nuclear materials is reviewed. Other applications of neutron resonance spectroscopy such as imaging, detection of explosives and drugs and thermometry are briefly discussed. A combination of NRTA and NRCA, referred to as Neutron Resonance Densitometry (NRD), is presented as a non-destructive method to quantify nuclear material, in particular the amount of special nuclear material in particle-like debris of melted fuel that is formed in severe nuclear accidents. Finally the importance of accurate nuclear resonance parameters for these applications is discussed and the performance of NRTA for the characterisation of nuclear material in the presence of matrix material is assessed.

Contents

1 Introduction

The probability that neutrons interact with nuclei strongly depends on the energy of the incoming neutron. This is illustrated in Fig. 1, which compares the total cross section for neutron induced reactions in ^{1}H, ^{6}Li, ^{10}B, ^{59}Co, ^{131}Xe, ^{208}Pb, ^{235}U, ^{238}U and ^{239}Pu. The cross sections reveal the presence of resonances, which are related to excited states of the compound nucleus just above the neutron separation energy. Resonance structured cross sections can be parameterized based on the R-matrix nuclear reaction formalism [1, 2]. Resonances are characterized by a set of resonance parameters, i.e. the resonance energy E_μ and partial widths (e.g. neutron width Γ_n, capture width Γ_γ, fission width Γ_f, ...), the total angular momentum J and the orbital angular momentum ℓ of the neutron-nuclear system. The partial widths express the relative probability for a specific reaction to occur. The total width Γ, which is the sum of the partial widths, is inversely proportional to the life time of the excited state. The smooth part of the total cross section is due to scattering from the nuclear potential and its magnitude depends on the scattering radius, which might depend on the orbital angular momentum ℓ. At relatively low energies the level density is low and the average distance D between resonances is large compared to the total width Γ. With increasing energy the average level distance decreases while the total width increases. Eventually, the level distance becomes smaller than the total width, such that resonance structures in the cross sections disappear and they are observed as a continuum [3].

Since resonances appear at energies that are specific for each nuclide, they can be used to determine the elemental and in some cases even the isotopic composition of materials and objects [4, 5]. The resonance structures in total and capture cross sections are the basis of Neutron Resonance Transmission Analysis (NRTA) and Neutron Resonance Capture Analysis (NRCA), respectively [4, 5]. Resonance structures can be revealed by applying the time-of-flight (TOF) technique [6]. In general the level density increases with the mass of the target nucleus, except for nuclei with a magic neutron and/or proton number (2, 8, 20, 28, 50, 82, and 126). Hence, the upper limit of the resonance region, i.e. the region where $D > \Gamma$, increases with mass. Fig. 1 also illustrates that for a light nucleus and nuclei with a magic proton and/or neutron number the first resonances appear at higher energies. These features of the cross sections as function of energy define the mass and energy region where NRCA and NRTA can be applied. NRCA and NRTA are applicable to almost all medium-weight and heavy elements. Due to the difference in experimental method, results obtained by NRTA will always be more accurate compared to those resulting from NRCA. In addition, NRTA is more applicable in case of radioactive samples. Hence, they provide complementary data. To improve the accuracy and detection limits, the two methods can be combined. A combination of NRTA, NRCA and Prompt Gamma ray Analysis (PGA) [7], referred to as Neutron Resonance Densitometry (NRD), is proposed as a non-destructive method to characterize particle-like debris of melted fuel [8, 9].

This report is used as the introduction in the compilation of resonance parameters for neutron induced reactions which is part of the Landolt-Bornstein series on Numerical Data and Functional Relationships in Science and Technology - Subvolume I/26A [].

2 Methodology

Both NRTA and NRCA are non-destructive methods which are based on well-established methodologies that are applied for neutron induced cross section measurements in the resonance region. They rely on the time-of-flight (TOF) technique, which is a standard technique for neutron resonance spectroscopy [6, 10, 11]. The resonance profiles that are observed in a TOF-experiment will be different from those in the nuclear cross sections shown in Fig. 1. They will be affected by experimental effects such as the thermal motion of the target nuclei, the finite resolution of the time-of-flight spectrometer, the sample characteristics, dead time effects and background contributions. To reduce bias effects and produce accurate results these effects have to be understood and taken into account in the data reduction and analysis procedures.

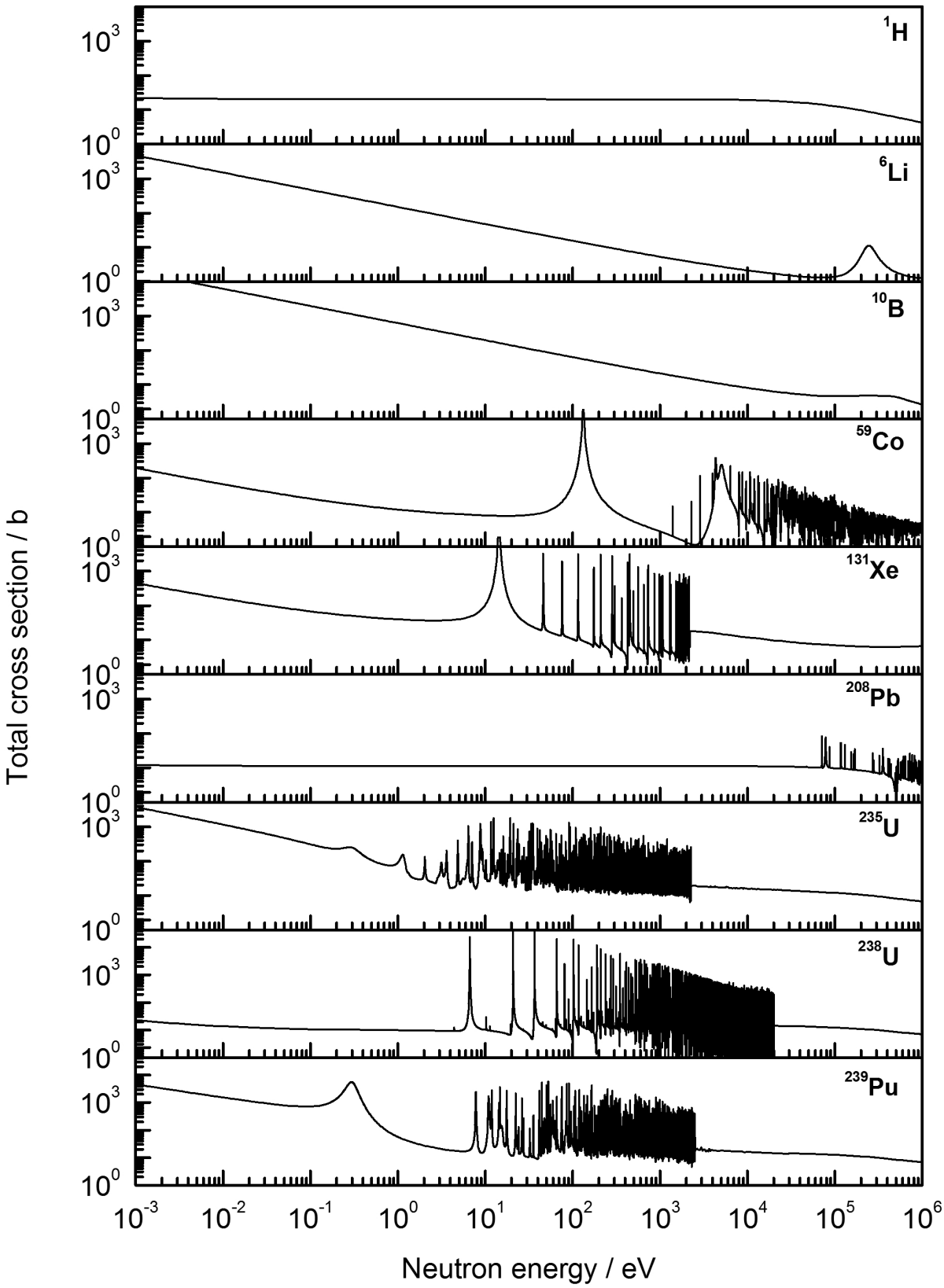

Fig. 1: Total cross section for neutron induced reactions in ^{1}H, ^{6}Li, ^{10}B, ^{59}Co, ^{131}Xe, ^{208}Pb, ^{235}U, ^{238}U and ^{239}Pu. It should be noted that the cross sections are based on calculations. In the region where resonances cannot be resolved experimentally, resonance fluctuations are not included in the calculations.

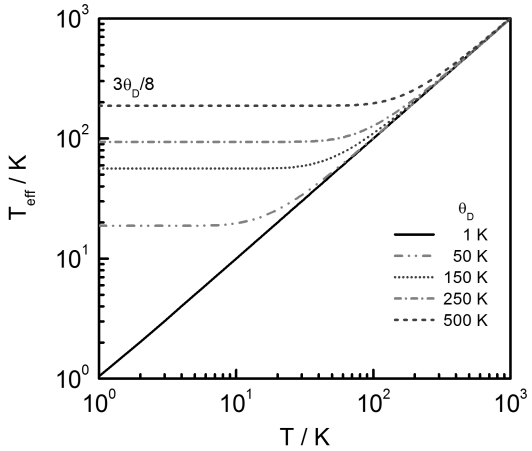

Fig. 2: Effective temperature T_{eff} as a function of the sample temperature T for different Debye temperatures θ_D using Eq. (7).

2.1 Doppler broadening

When a nuclear reaction takes place the atomic nuclei are not at rest. They have thermal motion in the lattice of the sample material. This motion will cause a shift in the relative kinetic energy or velocity of the neutron. Since the thermal motion is a statistical process, the relative energy will be distributed and the observed resonance profile will be broadened, which is known as Doppler broadening. A Doppler broadened cross section $\overline{\sigma}$ can be obtained from the convolution of the cross section σ for a target nucleus at rest with an energy transfer function $S(E, E')$ that accounts for the movement of the target nuclei [12]:

$$\overline{\sigma}(E) = \int dE' S(E, E')\sigma(E'). \tag{1}$$

For a mono-atomic free gas the thermal motion of the target nuclei can be described by a Maxwellian distribution. Within the free gas model (FGM) and for energies much larger than the Doppler width $E \gg \Delta_D$, a Doppler broadened cross section can be approximated by Gaussian broadening of the reaction rate, that is, by a convolution of $\sqrt{\frac{E'}{E}}\sigma(E')$ with a Gaussian distribution [3, 13, 14]:

$$\overline{\sigma}(E) \approx \frac{1}{\Delta_D\sqrt{\pi}} \int_{-\infty}^{\infty} dE'\, e^{-\left(\frac{E'-E}{\Delta_D}\right)^2} \sqrt{\frac{E'}{E}}\sigma(E'), \tag{2}$$

with the Doppler width Δ_D defined as:

$$\Delta_D = \sqrt{\frac{4Ek_BT}{M/m}}. \tag{3}$$

The rest mass of the target nucleus and neutron are denoted by M and m , respectively, and k_B is the Boltzmann constant. The Doppler width is related to the Full Width at Half Maximum (FWHM) of the Gaussian distribution by:

$$\text{FWHM} = 2\sqrt{\ln 2}\Delta_D. \tag{4}$$

It has been shown by Lamb [15] that the FGM approximation can also be applied for a crystalline solid by replacing the target temperature in Eq. (3) by an effective temperature T_{eff}. The latter is a measure of the mean kinetic energy of the atom in a material. Based on a Debye model of a crystal, the effective temperature T_{eff} can be related to the sample temperature T and the Debye temperature θ_D by [15]:

$$T_{eff} = 3\left(\frac{T}{\theta_D}\right)^3 T \int_0^{\theta_D/T} dt\, t^3 \left(\frac{1}{e^t - 1} + \frac{1}{2}\right) . \tag{5}$$

Table 1: Debye temperature Θ and effective temperature T_{eff} at 300 K of selected elements. The Debye temperatures were taken from Ref. [17]. The effective temperatures were calculated using Eq. (7).

Element	θ_D K	T_{eff} K	Element	θ_D K	T_{eff} K	Element	θ_D K	T_{eff} K	Element	θ_D K	T_{eff} K
C	2230	842.6	Mn	410	325.8	Ag	225	307.9	W	400	324.6
Mg	400	324.6	Fe	470	333.7	Cd	209	306.8	Au	165	304.2
Al	428	328.1	Co	445	330.3	In	108	301.8	Pb	105	301.7
Si	645	362.4	Ni	450	331.0	Cs	38	300.2	Th	163	304.1
V	380	322.2	Cu	343	318.2	Hf	252	309.9	U	207	306.7
Cr	630	359.6	Nb	275	311.7	Ta	240	308.9			

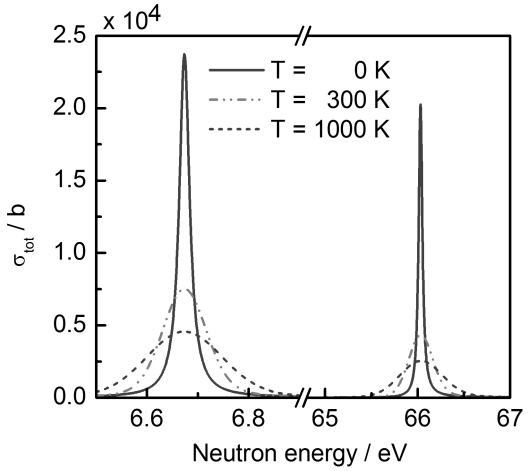

Fig. 3: Doppler broadened total cross sections around the 6.67 eV and 66.03 eV resonances of ^{238}U at 0 K, 300 K and 1000 K.

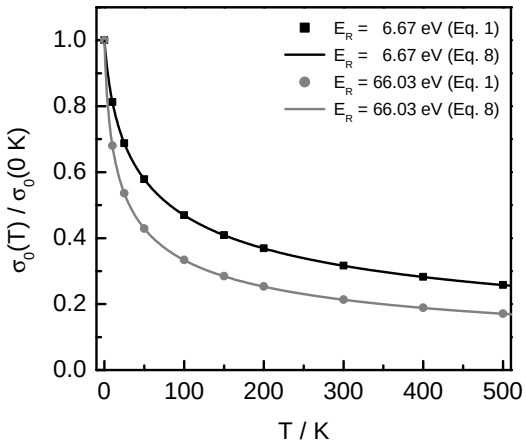

Fig. 4: Reduction of the peak total cross section for the 6.67 eV and 66.03 eV resonances of ^{238}U as a function of temperature.

Eq. (5) can be rewritten introducing the heat capacity C_v [16]:

$$T_{eff} = \frac{C_v\left(\theta_D/T\right)}{24} + \frac{3\theta_D/T}{4\left[e^{\theta_D/T}-1\right]} + \frac{3\theta_D/T}{8}. \tag{6}$$

Neglecting the first term in Eq. (6) the effective temperature can be approximated by:

$$T_{eff} \approx \frac{3}{8}\theta_D \coth\left(\frac{3}{8}\theta_D/T\right). \tag{7}$$

For elemental solid samples with minor components dissolved in the lattice, it may be assumed that the effective temperature of the lattice material can be used. Debye temperatures for some elements together with the resulting effective temperatures for a sample at 300 K are listed in Table 1. In Fig. 2 the effective temperature is plotted as a function of the sample temperature for different Debye temperatures. It should be noted that owing to zero point motion the effective temperature for a zero sample temperature is $3\theta_D/8$.

For many elements the Debye temperature is significantly lower than the room temperature. In all these cases the effective temperature for the FGM is just slightly higher than the room temperature and the FGM is a good approximation to account for the Doppler effect. This has been demonstrated by results of transmission measurements for ^{241}Am in Ref. [18]. For a strong lattice binding, low crystal

Fig. 5: Photograph of the time-of-flight facility GELINA of the EC-JRC-IRMM in Geel, Belgium.

temperatures and poly-atomic crystalline lattices, however, the Doppler profile is more complex and a more sophisticated theory or model is required (see e.g. Refs. [15, 19–23]).

The total cross section for a target at rest (0 K) and the Doppler broadened cross section at 300 K and 1000 K for ^{238}U are compared in Fig. 3. The cross sections are shown in the energy region around the 6.67 eV and 66.03 eV resonance of ^{238}U. This figure illustrates that due to the Doppler effect a resonance profile is broadened and the peak cross section is lowered. In case of an isolated resonance the capture cross section close to the resonance can be parameterized by the single level Breit-Wigner formula and the Doppler broadened resonance profile within the FGM approximation can be represented by a Voigt line shape [3]. For such a Voigt profile the reduction of the peak cross section becomes:

$$\psi(\beta) = \frac{\sqrt{\pi}}{\beta} \exp\left(\frac{1}{\beta^2}\right) \operatorname{erfc}\left(\frac{1}{\beta}\right), \tag{8}$$

where erfc is the complementary error function and $\beta = 2\Delta_D/\Gamma$. The reduction factors as a function of sample temperature for the 6.67 eV and 66.03 eV resonances in ^{238}U are shown in Fig. 4. The reductions based on Eq. (1) are compared with the ones based on the Voigt profile.

2.2 Neutron time-of-flight spectroscopy

Neutron TOF experiments can be carried out at a continuous neutron source using a chopper [24] or at a neutron source driven by an accelerator that is operated in pulsed mode [11, 25]. Due to the limited resolution, experiments using a chopper are only useful to study resonance structures in the low energy region, which limits their applicability. Time-of-flight measurements at a pulsed white neutron source are preferred when a wide range of elements or applications has to be covered. Pulsed neutron sources can be produced at electron- and proton-based accelerators. In electron-based accelerators high-energy electrons are stopped in a target that is usually made out of material with a high mass number. The resulting Bremsstrahlung radiation generates neutrons via photonuclear reactions. High energy proton accelerators produce neutrons by the spallation process in a metal target with a high mass number. Neutrons produced by the spallation process and photonuclear reactions have energies in the MeV region. Such an energy spectrum is not directly exploitable for neutron resonance spectroscopy. A moderator of hydrogen rich material is mostly used to produce a broad neutron spectrum ranging from thermal up to the MeV region. In Ref. [6, 26, 27] characteristics of some TOF-facilities are given. A photograph of the GELINA facility

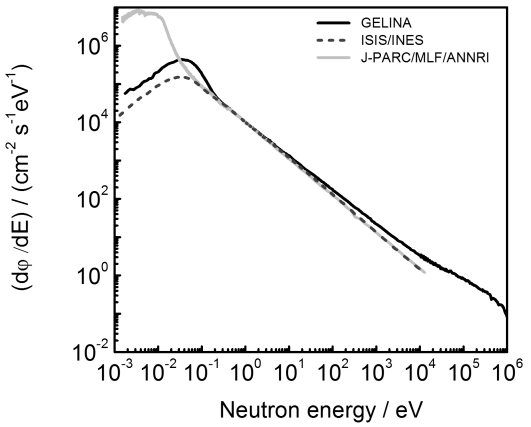

Fig. 6: Comparison of the neutron flux spectrum at GELINA, ISIS and J-PARC/MLF/ANNRI. The spectra are normalized to a neutron flux of 10^4 s^{-1} cm^{-2} eV^{-1} at 1 eV. The spectrum for J-PARC/MLF/ANNRI is based on calculations reported by Kino et al. [31].

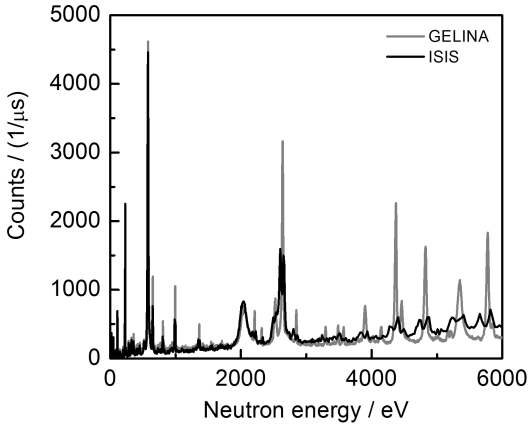

Fig. 7: Results of capture measurements of a bronze sample carried out at a 12.5 m station of GELINA and a 22.8 m station of ISIS. Data taken from Ref. [34]

installed at the EC-JRC-IRMM is shown in Fig. 5. A detailed description of this facility can be found in Ref. [28].

Fig. 6 compares the energy dependence of the neutron spectrum at GELINA with the one at the INES diffractometer of ISIS [29] and J-PARC/MLF/ANNRI [30, 31]. These moderated neutron spectra can be approximated by a Maxwellian distribution in the thermal region, an additional Maxwellian (or even better Watt) function in the fast region and a 1/E$^\alpha$ dependence in the epi-thermal region, with $\alpha \sim 0.85$ for GELINA and $\alpha \sim 0.95$ for ISIS/INES and J-PARC/MLF/ANNRI. The spectrum at GELINA is given for a flight path viewing the two water-filled beryllium containers, which are placed above and below the neutron producing uranium target. A Cu and Pb bar acts as a shielding against the direct beam from the uranium target. The beam at the INES station is a decoupled moderated neutron beam. The moderator is water that is poisoned with Gd. The beam at J-PARC/ANNRI is a coupled water moderated neutron beam. The data in Fig. 6 have been normalized to a neutron flux of 10^4 cm^{-1}s^{-1}eV^{-1} at 1 eV. This value corresponds to a nominal neutron output at GELINA for measurements at 10 m distance with the accelerator operating at 800 Hz and an average current of 70 μA. For a similar distance and normal operation conditions, i.e. 50 Hz operating frequency, the output at ISIS and J-PARC/MLF/ is larger by about a factor 450.

Neutron spectroscopy applying the TOF technique relies on a measurement of the time t that a neutron needs to travel a given distance L. The time t and distance L are related to the velocity v and kinetic energy E of the neutron by:

$$v = \frac{L}{t} \tag{9}$$

and

$$E = mc^2(\gamma - 1), \tag{10}$$

respectively, with γ the Lorentz factor:

$$\gamma = \frac{1}{\sqrt{1 - (v/c)^2}}, \tag{11}$$

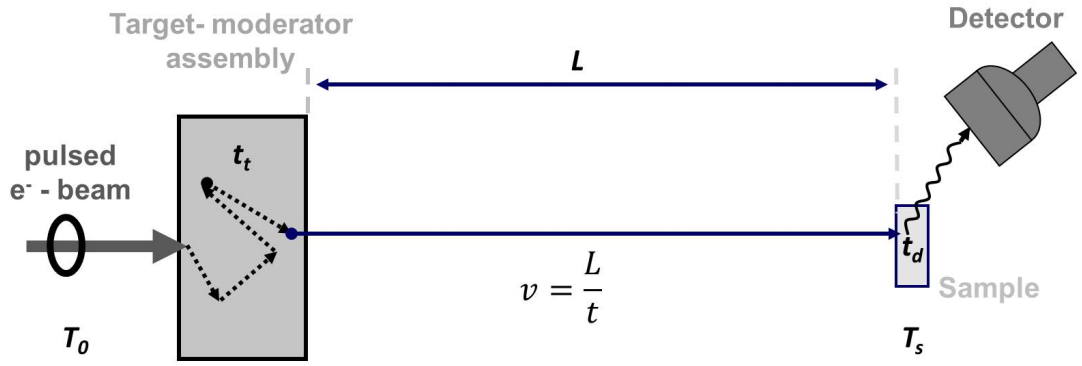

Fig. 8: Schematic representation of the time-of-flight technique. The symbols are explained in the text.

and c the speed of light. Experimentally a time-of-flight t_m is derived from the difference between a start T_0 and stop T_S signal:

$$t_m = (T_S - T_0) + t_0, \tag{12}$$

where t_0 is a time-offset. This offset is mostly due to a difference in cable lengths. For scintillator detectors the off-set can be deduced accurately from a measurement of the TOF of the γ-ray flash produced in the target. For other detectors, e.g. solid state or gaseous neutron or charged particle detectors, the time-offset derived from the γ-ray flash might be biased due to the difference between the energy-loss process of a γ-ray and a charged particle and the time-offset is best derived from transmission dips or resonance peaks of high energy resonances for which the resonance energies are accurately known.

The observed time-of-flight t_m is related to the time t that a neutron, leaving the target-moderator assembly with a velocity v, needs to travel the distance L (see Fig. 8) [6]:

$$t_m = t + t_t + t_d, \tag{13}$$

where t_t is the time difference between the moment that the neutron is created and the time it leaves the target-moderator assembly and t_d is the difference between the time of detection and the moment the neutron enters the detector (transmission) or sample (capture). The conversion of the neutron energy E into the observed time-of-flight t_m defines the response function $R(t_m, E)$ of the TOF-spectrometer. This response function, which expresses the probability that a neutron with energy E is observed with a TOF t_m, can be considered as a convolution of different independent contributions due to [6]:

- the finite duration of the start pulse (T_0);
- the time resolution of the detector and electronics (T_s);
- the neutron transport in the neutron producing target (t_t); and
- the neutron transport in the detector or sample (t_d).

The probability distribution of T_0 strongly depends on the type of accelerator or on the characteristics of the chopper for measurements at a continuous beam. At GELINA this component can be represented by a normal distribution with a FWHM of about 1 ns [28]. At J-PARC/MLF this contribution depends on the time structure of the proton pulse produced by the 3 GeV synchrotron. It is a double pulse structure that can be approximated by the sum of two normal distributions which are separated by approximately 0.6 μs and with a FWHM of about 0.1 μs [32, 33]. A similar double pulse structure is also present at the ISIS facility [34]. The impact of this structure is shown in Fig. 7, where the response of a capture detection system for measurements with a bronze sample at a 12.5 m station of GELINA and at the 22.8 m INES station of ISIS is compared. The random time jitter of the detector and electronics, determining the broadening of T_S, is mostly described by a normal distribution with a width that is independent of time. The contributions of T_0 and T_S are often lumped together into one distribution.

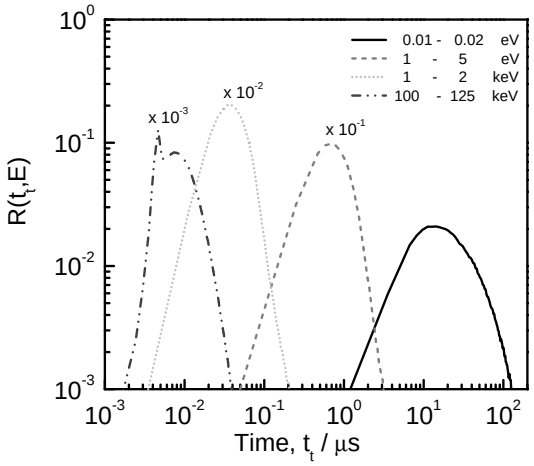

Fig. 9: The probability distribution of the time t_t that a neutron spends in the target-moderator assembly of GELINA [6].

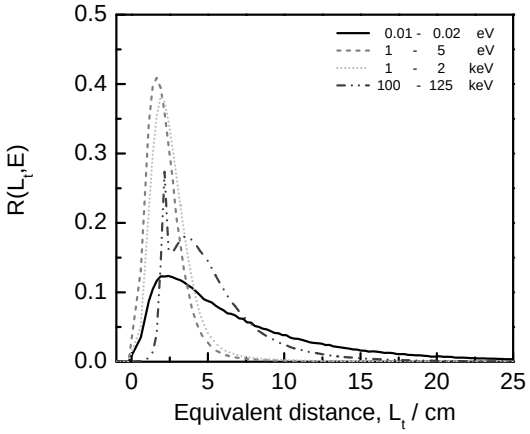

Fig. 10: The probability distribution of the equivalent distance L_t that a neutron travels in the target-moderator assembly of GELINA [6].

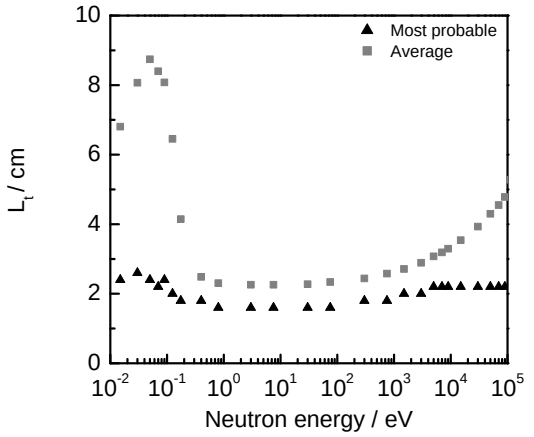

Fig. 11: The average and most probable equivalent distance as a function of neutron energy for the target-moderator assembly of GELINA [6].

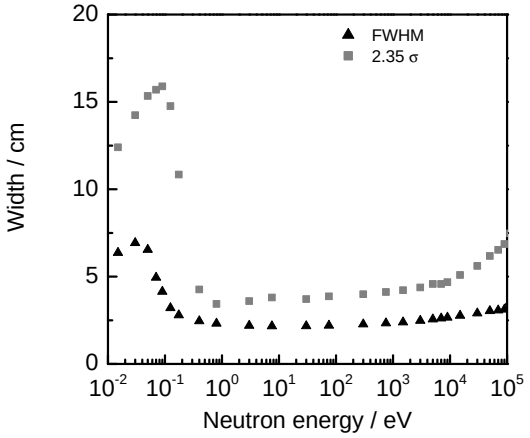

Fig. 12: Width if the equivalent distance distribution as a function of neutron energy for the target-moderator assembly of GELINA [6].

For a moderated neutron beam the response function is predominantly determined by the neutron transport in the target-moderator assembly, i.e. by the probability distribution of t_t. Therefore, this contribution strongly depends on the neutron physics properties and geometry of the assembly. Response functions due to the neutron transport are mostly represented by introducing an equivalent distance L_t [35, 36]. The equivalent distance is defined as $L_t = vt_t$, where v is the velocity of the neutron at the moment it escapes from the target-moderator assembly. Such a transformation of variables results in probability distributions of L_t which are less dependent on the neutron energy [6]. They can be obtained from stochastic calculations or approximated by analytical expressions. Monte Carlo (MC) simulations to determine the probability distribution of the time the neutron spends in the target-moderator assembly have been carried out for e.g. GELINA [37, 38], J-PARC/MLF/ANNRI [32], J-PARC/MLF/NOBORU [33], n_TOF [39], ORELA [40] and RPI [41]. Examples of response functions as a function of the time t_t and the equivalent distance L_t for GELINA are shown in Fig. 9 and 10, respectively. The distributions result from MC simulations for a moderated neutron beam at GELINA and a flight path that forms an

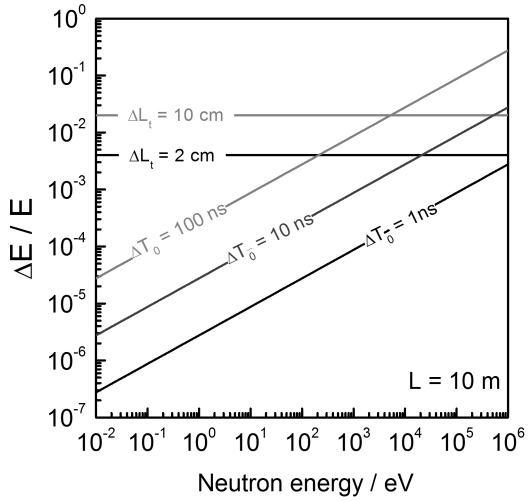

Fig. 13: Energy resolution broadening due to neutron transport in the target-moderator assembly (ΔL_t) and due to the finite duration of the start pulse (ΔT_0) as function of neutron energy for a flight path distance of 10 m.

angle of 0° with the normal to the exit face of the moderator viewing the flight path. The distributions expressed as a function of the time t_t strongly depend on the neutron energy. This dependence is much weaker when they are expressed as a function of the equivalent distance. This can also be concluded from the average and most probable time t_t and distance L_t as a function of neutron energy and from the corresponding FWHM as a function of neutron energy. The increase in average distance and FWHM for energies below 1 eV is due to fully thermalized neutrons, also referred to as neutron storage in the moderator. Fig. 12 reveals that for energies above 1 eV the FWHM at GELINA is about 2.5 cm and almost independent of neutron energy. The figure also shows that due to the tail in the distribution the variance is considerable greater than that for a Guassian distribution with same FWHM.

Several analytical expressions have been proposed to describe the response due to the target/moderator assembly [32, 33, 42, 43]. Most of them are based on an exponential tail due to the primary neutron production and a χ^2-distribution to describe the moderation process, as suggested by Groenewold and Groendijk [35]. For neutron energies below 1 eV an additional storage term has to be taken into account as demonstrated by Ikeda and Carpenter [44]. This approach has been applied for e.g. GELINA [42], ORELA [43] and J-PARC/MLF/ANNRI [32]. The function proposed by Cole and Windsor [45], was used in Ref. [33] to describe the response for the NOBORU beam line at J-PARC/MLF. Using this function the results obtained by Monte Carlo simulations were slightly better reproduced compared to a function based on a χ^2-distribution combined with the storage term of Ref. [44]. On the other hand Kino et al. [32] observed a good agreement between response functions of the ANNRI beamline of J-PARC/MLF obtained with Monte Carlo simulations and those resulting from the χ^2-distribution combined with the storage term of Ref. [44].

All the components (T_S,T_0,t_t,t_d) contribute to the final energy or velocity resolution of the spectrometer. The energy resolution ΔE is related to the velocity resolution Δv by:

$$\frac{\Delta E}{E} = (\gamma + 1)\gamma \frac{\Delta v}{v}. \tag{14}$$

At low velocities ($\gamma \approx 1$) the relative energy resolution is twice the relative velocity resolution. Supposing that the different contributions follow a Gaussian distribution, the velocity resolution is:

$$\frac{\Delta v}{v} = \frac{1}{L}\sqrt{(v\Delta T_S)^2 + (v\Delta T_0)^2 + \Delta L_t^2 + \Delta L_d^2}. \tag{15}$$

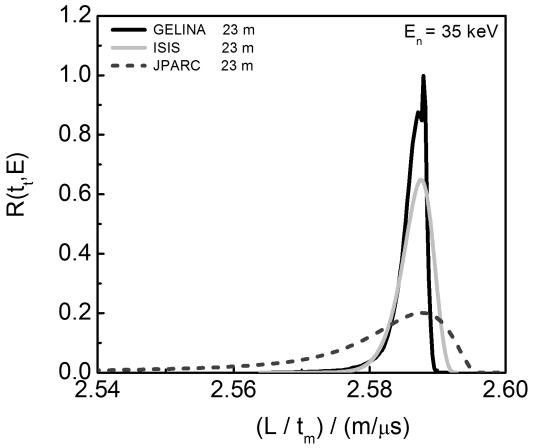

Fig. 14: Response function for TOF measurements of a 35 keV neutron at a 23 m station GELINA, ISIS and J-PARC. The distributions were normalized to have the same area and scaled to align the time t_m with the highest probability.

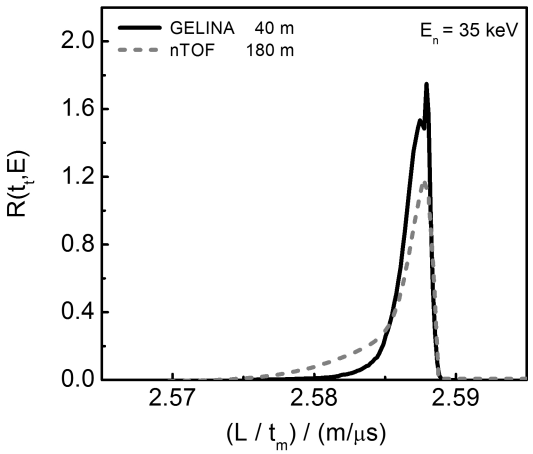

Fig. 15: Response function for TOF measurements of a 35 keV neutron at a 40 m station of GELINA and a 180 m station of n_TOF. The distributions were normalized to have the same area and scaled to align the time t_m with the highest probability.

where the broadening due to the neutron transport in the target-moderator assembly and the detector (or sample) are expressed by an equivalent distance $L_t = vt_t$ and $L_d = vt_d$, respectively. The components (ΔT_S, ΔT_0, ΔL_t, ΔL_d) in Eq. (15) are in first approximation independent of the neutron energy. Hence, for a fixed velocity or energy the resolution improves with increasing distance. The impact of the different components to the total resolution is shown in Fig. 13, where the resolution for a flight path of 10 m is plotted as a function of energy for different values of ΔL_t and ΔT_0. The results in Fig. 13 reveal that at low energies the component ΔL_t dominates and the width of the charged particle pulse is less important. At higher energies, however, the component ΔT_0 determines the broadening of the observed profile.

Differences in resolution due to the neutron production are illustrated in Figs. 14 and 15. In these figures the responses for TOF measurements of a 35 keV neutron only due to the neutron transport in the target/moderator assembly are shown. Fig. 14 compares the response for measurements at a 23 m station of GELINA, ISIS and J-PARC/MLF/ANNRI. The response for measurements at a 40 m station of GELINA and a 180 m station of n_TOF are compared in Fig. 15. These figures clearly demonstrate the superior resolution of a white neutron source resulting from photonuclear reactions, such as GELINA, compared to the resolution of a spallation source. The differences in resolution can be expressed by the FWHM of the equivalent distance distribution which are $\sim$ 2.5 cm for GELINA, $\sim$ 5 cm for ISIS/INES and $\sim$ 13 cm for J-PARC/MLF/ANNRI and n_TOF. Besides the substantial increase in FWHM, the response at J-PARC/MLF/ANNRI and n_TOF are affected by a pronounced contribution of a tail on the low energy side.

The impact of both the Doppler effect and the response function on resonance profiles is illustrated in Fig. 17 and 16. Theoretical profiles for ^{238}U resonances in two different energy regions are shown. The calculations were carried out with REFIT [42] based on response functions of GELINA for a time-of-flight distance of L = 5, 10 and 30 m. These figures illustrate that for low energy resonances the broadening is primarily due to the Doppler effect. At higher energies, the resolution of the TOF-spectrometer starts to dominate and the width of the observed profile will strongly depend on the distance. Since the neutron flux at TOF-facilities is in first approximation inversely proportional to the square of the distance, a compromise between resolution and intensity has to be made when choosing the flight path distance.

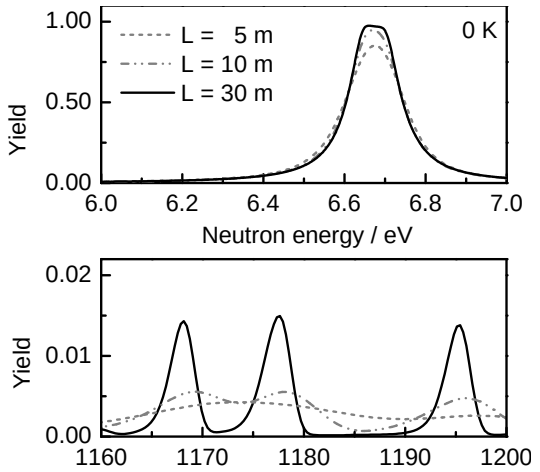

Fig. 16: Theoretical capture yield of a ^{238}U sample with an areal density of 1.0×10^{-3} at/b at T_{eff} = 0 K with a flight path distance of 5 m, 10 m, and 30 m.

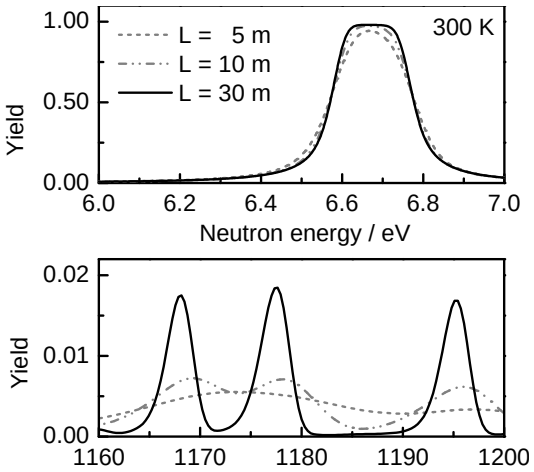

Fig. 17: Theoretical capture yield of a ^{238}U sample with an areal density of 1.0×10^{-3} at/b at T_{eff} = 300 K with a flight path distance of 5 m, 10 m, and 30 m.

All count rate spectra obtained from a TOF experiment require a correction due to the dead time of the detection system consisting of the detector, electronics, digitizers and data acquisition system. In case of a fixed (non-extendable) dead time, the correction is well understood. In Ref. [46] models to correct for the dead time are given. Assuming a stable beam the corrected counts $N_c(i)$ in channel i are given by:

$$N_c(i) = N_0(i) / \left(1 - \sum_{j=i_0}^{i-1} N_0(j)/N_b - N_0(i)/2N_b \right) , \tag{16}$$

where N_b is the total number of bursts. In case of a varying beam intensity the corrected counts $N_c(i)$ can be determined by:

$$N_c(i) = N_b \left\{ -\ln \left(1 - \frac{N_0(i)/N_b}{\left[1 - \sum_{j=i_0}^{i-1} N_0(j)/N_b \right]} \right) \Bigg/ \left[1 - \sigma \, \tanh \left(\sigma \sum_{j=i_0}^{i-1} N_c(j)/N_b \right) \right] \right\} , \tag{17}$$

where σ^2 is the relative variance of the beam intensity. It has been demonstrated in Refs. [6, 47] that in case of a fixed dead time bias effects due to the dead time correction can be reduced to $\leq 0.3\%$ when the corrections are smaller than a factor 1.3.

2.3 Neutron resonance transmission analysis

NRTA is based on the analysis of characteristic dips in a transmission spectrum resulting from a measurement of the attenuation of a neutron beam by the sample under investigation [4, 5]. These dips are observed at TOF values that correspond to resonance energies.

The quantity of interest in a transmission experiment is the fraction of the neutron beam traversing the sample without any interaction. For a parallel neutron beam which is perpendicular to a slab of material, this fraction or transmission T is given by:

$$T = e^{-\sum\limits_{k} n_k \overline{\sigma}_{tot,k}} , \tag{18}$$

where $\overline{\sigma}_{tot,k}$ is the Doppler broadened total cross section and n_k is the number of atoms per unit area of nuclide k. The transmission is directly related to the total cross section and the areal density of the nuclides present in the sample. Assuming that the total cross sections of the materials present in the sample are known, a measurement of the attenuation of an incident neutron beam can be used for elemental and isotopic analysis.

The experimental transmission T_{exp} is derived from the ratio of the counts of a sample-in measurement C_{in} and a sample-out measurement C_{out}, both corrected for their background contributions B_{in} and B_{out}, respectively:

$$T_{exp} = N_T \frac{C_{in} - k_T B_{in}}{C_{out} - k_T B_{out}}. \tag{19}$$

The experimental TOF-spectra (C_{in}, B_{in}, C_{out}, B_{out}) in Eq. (19) are corrected for losses due to the dead time in the detector and electronics chain and all spectra are normalized to the same neutron intensity and TOF-bin width. Such a normalization is mostly based on measurements with additional beam monitors. The uncertainty due to this normalization can be reduced to less than 0.25% by alternating sequences of sample-in and sample-out measurements, such that systematic effects due to slow variations in time of both the beam intensity and detector efficiency are avoided. To account for this uncertainty the normalization factor N_T = 1.0000 $\pm$ 0.0025 can be introduced in Eq. (19) [6, 48]. The factor k_T in Eq. (19) introduces a correlated uncertainty component accounting for systematic effects due to the background model.

Eq. (19) reveals that the experimental transmission is deduced from a ratio of counting spectra. Therefore, it is independent of the detector efficiency and incoming neutron flux. Hence, no absolute measurement of the neutron flux or additional calibration measurements to determine the detection efficiency are needed. In addition, the experimental transmission T_{exp} is a direct measure of the theoretical transmission (Eq. (18)) if the measurements are performed in a good transmission geometry, that is, when [6]:

- the sample is perpendicular with respect to a parallel incoming neutron beam;
- all neutrons that are detected have passed through the sample; and
- neutrons scattered by the sample and collimators are not detected.

The conditions of an ideal or good transmission geometry can be achieved by a proper collimation of the neutron beam at both the sample and detector position. A schematic view of a transmission set-up in good geometry is shown in Fig. 18. It shows the experimental geometry of a 50 m station at GELINA [48]. An ideal transmission geometry also requires a constant homogeneous spatial distribution of the sample material. Problems in case of heterogeneous samples will be discussed in detail in Sec. 5.3.

For neutron energies below 1 MeV, Li-glass scintillators enriched in ^{6}Li are mostly used [48–50]. The time resolution of such detectors depends predominantly on the neutron transport within the detector. The contribution to the final response function is also best expressed by an equivalent distance L_d. The probability distribution of the time t_d (or of the equivalent distance L_d) will depend on the size, material density and cross sections of the main components with which the neutron interacts in the detector. Examples of a response for a 6.35-mm thick and 152.4-mm diameter Li-scintillator, enriched to 95% in ^{6}Li, that is used at a 50 m transmission station of GELINA are shown in Figs. 19 and 20 for neutrons with an energy of 10 and 100 eV, respectively. Response functions obtained by Monte Carlo simulations are compared with the results of analytical expressions which are implemented in the resonance shape analysis code REFIT [42].

The background in a TOF transmission measurement can be considered as a sum of various contributions due to the detection of γ-rays and neutrons that have lost the correlation in time. Their origin and relative contribution strongly depends on the accelerator characteristics, neutron source and detector properties [6]. The background is mostly expressed as an analytical expression and determined by the

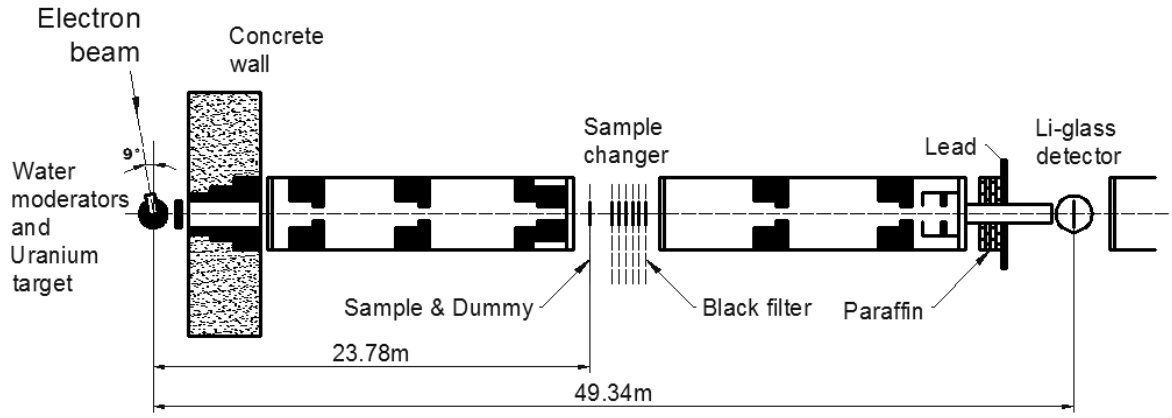

Fig. 18: Schematic representation of a transmission measurement set-up at GELINA [48].

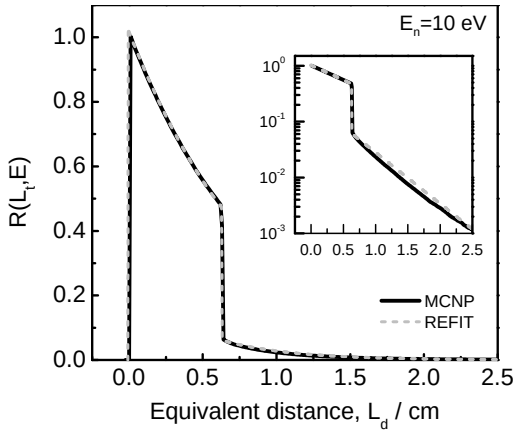

Fig. 19: Response function of a 6.35-mm thick and 152.4-mm diameter Li-scintillator, enriched to 95% in ^{6}Li, for neutron with an energy of 10 eV.

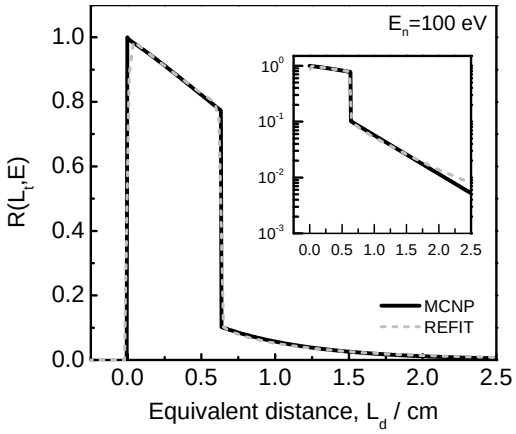

Fig. 20: Response function of a 6.35-mm thick and 152.4-mm diameter Li-scintillator, enriched to 95% in ^{6}Li, for neutron with an energy of 100 eV.

black resonance technique. For this technique, samples of elements with strong absorption resonances, which are referred to as black resonance filters, are inserted into the beam. The free parameters in the analytical expression are determined by a least squares fit to saturated resonance dips observed in the TOF-spectra due to the presence of the filters. An example of a sample-in and sample-out spectrum together with their background contributions is shown in 21 and 22. The spectra were taken to determine the transmission through a sample of tungsten. The measurements were performed at a 25 m station of GELINA with a 12.7-mm thick and 101.6-mm diameter Li-glass scintillator enriched to 95% in ^{6}Li and the accelerator operating at 800 Hz [51]. The background as a function of TOF was parameterized by an analytical expression consisting of a constant and three exponentials:

$$B(t) = b_0 + b_1 e^{-\lambda_1 t} + b_2 e^{-\lambda_2 t} + b_3 e^{-\lambda_3 (t+t_0)} \; . \tag{20}$$

The parameter b_0 is the time independent contribution. The first exponential is due to the detection of 2.2 MeV γ-rays resulting from neutron capture in hydrogen present in the moderator. The time dependence of this background component was verified by Monte Carlo simulations and confirmed by measurements with polyethylene filters in the beam. As mentioned in Ref. [6, 48], the polyethylene filter is used to scatter neutrons out of the beam and enhance the ratio of the γ-ray to neutron intensity. The second exponential originates predominantly from neutrons scattered inside the detector station.

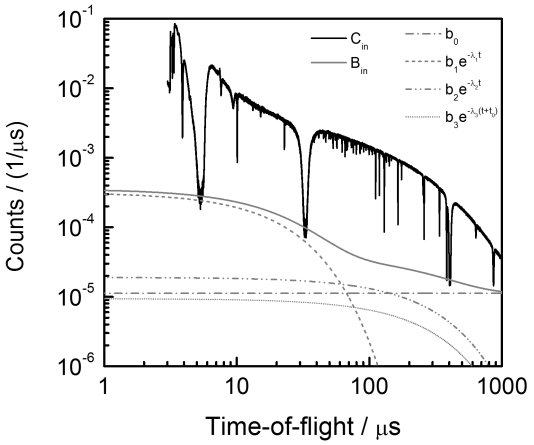

Fig. 21: TOF-spectra taken with a Li-glass detector resulting from transmission measurements of a ^{nat}W sample at a 25 m station of GELINA [51]. The sample-in spectrum is shown together with the total background and its components.

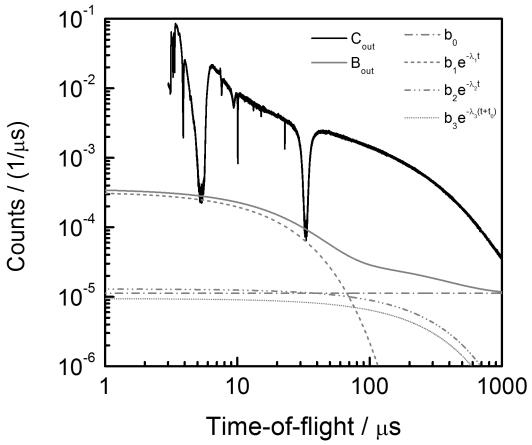

Fig. 22: TOF-spectra taken with a Li-glass detector resulting from transmission measurements of a ^{nat}W sample at a 25 m station of GELINA [51]. The sample-out spectrum is shown together with the total background and its components.

The last time dependent component accounts for the contribution due to slow neutrons from previous accelerator cycles. This contribution was estimated by an extrapolation of the TOF spectrum at the end of the cycle. It was approximated by an exponential, with t_0 related to the operating frequency of the accelerator ($t_0 = 1.25$ ms for 800 Hz). The time dependence of the background was derived from dedicated measurements with S, Na, Co, W and Ag black resonance filters in the beam. During the regular sample-in and sample-out runs, the S and Na black resonance filters were kept in the beam to continuously monitor the background at 2.85 keV and 102 keV and to account for the dependence of the background level on the presence of the sample. Applying such a procedure the uncertainty due to the background model can be reduced to less than 3% [6]. This uncertainty component can be included in the data reduction process by introducing the factor k_T = 1.00 $\pm$ 0.03 in Eq. (19).

2.4 Neutron resonance capture analysis

NRCA relies on the analysis of resonance peaks in TOF spectra resulting from the detection of prompt γ-rays, which are emitted after a neutron capture reaction in the sample under investigation [4,5,52]. The observable of interest is the capture yield, which is the fraction of the incident neutron beam undergoing a capture reaction in the sample. The theoretical capture yield Y_γ can be expressed as a sum of primary $Y_{0,k}$ and multiple interaction events $Y_{m,k}$ for each nuclide present in the sample:

$$Y_\gamma = \sum_k Y_{\gamma,k} = \sum_k (Y_{0,k} + Y_{m,k}). \tag{21}$$

Multiple interaction events result from a (n,γ) reaction after at least one neutron scattering in the sample. The primary yield $Y_{0,k}$ for a parallel uniform neutron beam and a homogeneous slab of material that is placed perpendicular to the neutron beam is :

$$Y_{0,k} = n_k \overline{\sigma}_{\gamma,k} F, \tag{22}$$

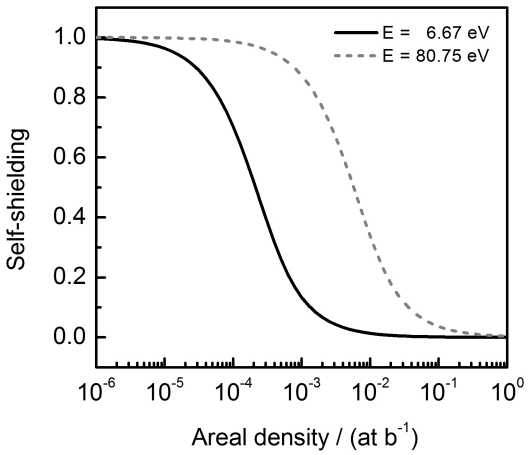

Fig. 23: Self-shielding F due to the peak cross section of the 6.67 eV and 80.75 eV resonance of ^{238}U as function of areal density.

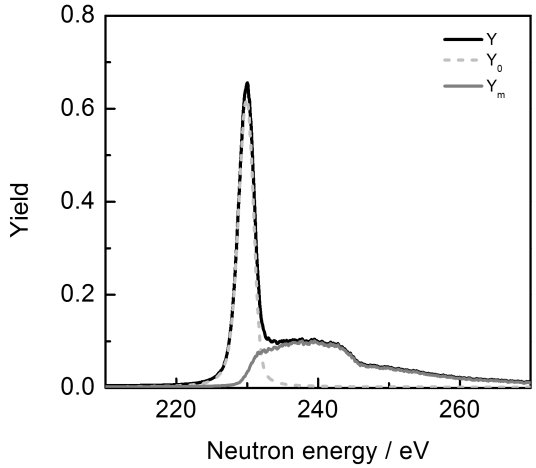

Fig. 24: Simulated capture yield Y for a 14-mm thick Cu sample in the region of the 230 eV resonance of ^{65}Cu is plotted as a function of neutron energy. The contributions of the primary yield Y_0 and the yield due to multiple interaction events Y_m are shown as well.

where $\overline{\sigma}_{\gamma,k}$ is the Doppler broadened capture cross section and F is the self-shielding caused by the attenuation of the neutron beam in the sample. The latter is defined by :

$$F = \frac{\left(1 - e^{-\sum\limits_{j} n_j \overline{\sigma}_{tot,j}}\right)}{\sum\limits_{j} n_j \overline{\sigma}_{tot,j}}. \tag{23}$$

This expression contains the sum over all nuclides contributing to the self-shielding. The self-shielding approaches unity and the capture yield is directly proportional to the product of the areal density and capture cross section, only for very thin samples and/or small cross sections, such that $\sum_j n_j \overline{\sigma}_{tot,j} \ll 1$. Fig. 23 shows the self-shielding for the peak cross section of the 6.67 eV and 80.75 eV resonances of ^{238}U as a function of the areal density. Evidently, the self-shielding strongly depends on the resonance strength.

For relative thick samples multiple interaction events have a substantial contribution to the total yield. This is illustrated in Fig. 24, where the capture yield for a 14-mm thick Cu sample in the region of the 230 eV resonance of ^{65}Cu is plotted as a function of neutron energy. The results have been obtained by Monte Carlo simulations.The contribution of the primary yield Y_0 and the yield due to multiple interaction events Y_m are shown. For a correct calculation of this yield the capture and scattering cross section is required. Therefore, the relation between the observable in a capture experiment and the areal densities n_k is more complex as compared to the relationship for a transmission experiment.

The experimental capture yield Y_{exp} is derived from the response of the capture detection system divided by the neutron flux φ and corrected for various quantities related to the detection of the prompt γ-rays:

$$Y_{exp} = \frac{C_\gamma - B_\gamma}{\epsilon_c \Omega P A \varphi}, \tag{24}$$

where C_γ and B_γ are the observed dead time corrected sample and background spectra, respectively. The effective area of the sample seen by the neutron beam is denoted by A, P is the probability that the prompt γ-rays escape from the sample, Ω is the solid angle between sample and detector and ϵ_c is the

probability to detect at least one γ-ray out of the γ-ray cascade following the neutron capture reaction. In most cases the parameters (A, P, Ω, ϵ_c) related to the detection of the prompt γ-rays and the absolute value of the neutron flux at a given energy are lumped together into one normalization factor N_γ and the experimental yield becomes:

$$Y_{exp} = N_\gamma \frac{C_\gamma - B_\gamma}{\varphi'}. \tag{25}$$

The normalization factor N_γ can be determined at an energy where the theoretical yield is known and only the shape of the neutron flux, i.e. its relative energy dependence denoted by φ', needs to be determined. Ideally, the data is normalized to a saturated resonance with $\Gamma_n << \Gamma_\gamma$, such that the normalization is independent of the sample thickness and of the resonance parameters [6, 53].

Eq. (25) can only be applied when the parameters (A, P, Ω, ϵ_c) are energy and nuclide independent. Mostly only the solid angle and effective area are independent of the energy of the incident neutron and special analysis procedures are required to account for the energy dependence of the other quantities [6]. For example, when the neutron beam shows an energy dependent spatial profile, the beam interception area A is energy dependent and corrections are required [54].

The detection efficiency ϵ_c to detect at least one γ-ray strongly depends on the method and the detection system. Ideally, a detection system is used with a very good time resolution, a low sensitivity to scattered neutrons and an efficiency ϵ_c that is independent of the γ-ray cascade, i.e. independent of multiplicity and energy spectrum [6]. The sensitivity has to be low for direct neutron detection and for indirect events due to neutrons which are scattered by the sample and subsequently captured in the detector or its environment. A detection efficiency independent of the γ-ray cascade can be realized by a total absorption detector with an almost 100% efficiency [55–59] or by applying the total energy detection principle [6, 60, 61], so that the detection efficiency becomes proportional to the total γ-ray energy produced in the capture event. The total energy detection principle requires a γ-ray detector with a relatively low detection efficiency that is proportional to the γ-ray energy [60, 61]. In principle, it is applicable for any conventional γ-ray detector when the pulse height weighting technique (PHWT) is applied. The PHWT relies on a mathematical manipulation of the response function of the detection system to achieve the proportionality between the detection efficiency and the γ-ray energy. This technique is based on a suggestion by Maier-Leibnitz and first applied by Macklin and Gibson [62]. Mostly C_6D_6 liquid scintillators are used. They are considered as one of the best detection systems for neutron capture cross section studies of non-fissile material in a broad energy region [6]. For these detectors accurate weighting functions can be obtained from Monte Carlo simulations, provided that the geometry description reflects the experimental conditions including the details of both detection system and the sample [6, 61]. More details about the different methods and principles can be found in Ref. [6].

The performance of BGO, BaF_2, YAP and YSO scintillation detectors for NRCA applications has been compared in Ref. [34], considering the response of a C_6D_6 liquid scintillator as a reference. The measurements were carried out at the GELINA facility. Figs. 25, 26, 27, 28, show the results from measurements with a 0.4-mm thick Cu sample containing Sn as an impurity. The results in Ref. [34] revealed that the time resolution of the above mentioned scintillators is sufficient for NRCA measurements in the epithermal region below 5 keV. However, BGO and BaF_2 detectors suffer in the energy region below 500 eV from neutron sensitivity, as shown in Figs. 25 and 27. The performance of YAP and YSO crystals in the energy region below 1 keV is comparable to the one of C_6D_6. Above 1 keV, the response of YAP and YSO detectors suffer from the high probability of neutrons interacting with yttrium.

The background for capture measurements is more complex compared to the one for transmission measurements. It consists of: (1) a time independent component due to ambient radiation and possible radioactivity in the sample; (2) a time dependent component independent of the sample and (3) a time dependent component depending on the sample characteristics. The relative contribution of these components strongly depends on the neutron facility and detection system that is used [6]. The first component can be estimated from measurements just after the accelerator is switched off, or in a TOF region

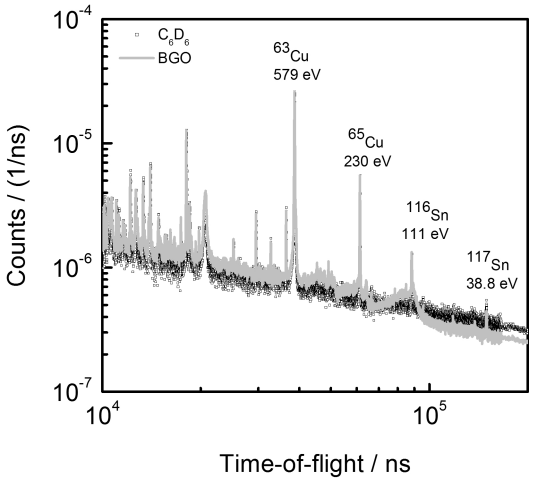

Fig. 25: Count rate spectra from capture measurements with a 0.4-mm Cu sample containing Sn using BGO and C_6D_6 scintillation detectors. Data taken from Ref. [34].

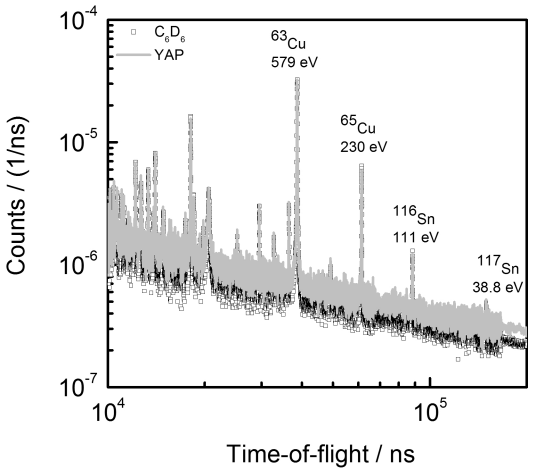

Fig. 26: Count rate spectra from capture measurements with a 0.4-mm Cu sample containing Sn using YAP and C_6D_6 scintillation detectors. Data taken from Ref. [34].

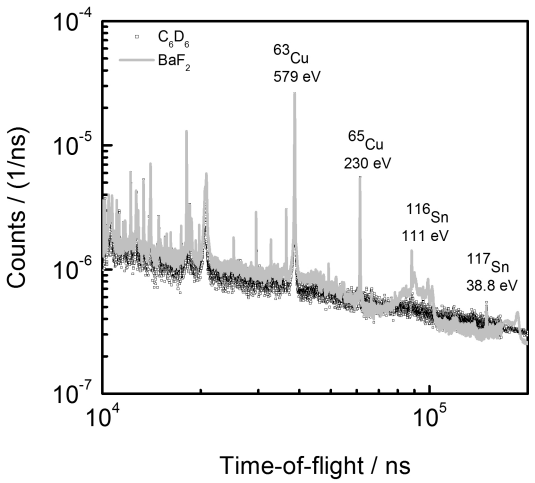

Fig. 27: Count rate spectra from capture measurements with a 0.4-mm Cu sample containing Sn using BaF_2 and C_6D_6 scintillation detectors. Data taken from Ref. [34].

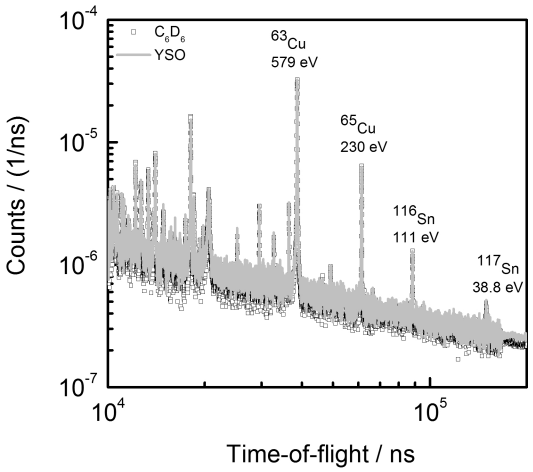

Fig. 28: Count rate spectra from capture measurements with a 0.4-mm Cu sample containing Sn using YSO and C_6D_6 scintillation detectors. Data taken from Ref. [34].

where the neutron flux is negligible. The time dependent component independent of sample properties results mainly from neutrons that are scattered inside the measurement station and at other flight paths in case of a multi-user facility. This contribution can be deduced from measurements without a sample in the beam. The last component is the most difficult one to quantify. It depends on the neutron and γ-ray scattering properties of the sample, on the neutron sensitivity of the detection system and the characteristics of the measurement station. The neutron sensitivity in this discussion is the detector response due to neutrons which are scattered from the sample and create a capture reaction in the sample-detector environment. One has to differentiate between a direct and a delayed component. The direct component originates from scattered neutrons which cause an immediate capture reaction in the detector assembly. This contribution follows the resonance structure of the cross section and is hard to distinguish from the response due to a (n,γ) reaction in the sample. The delayed component is due to neutrons that scatter

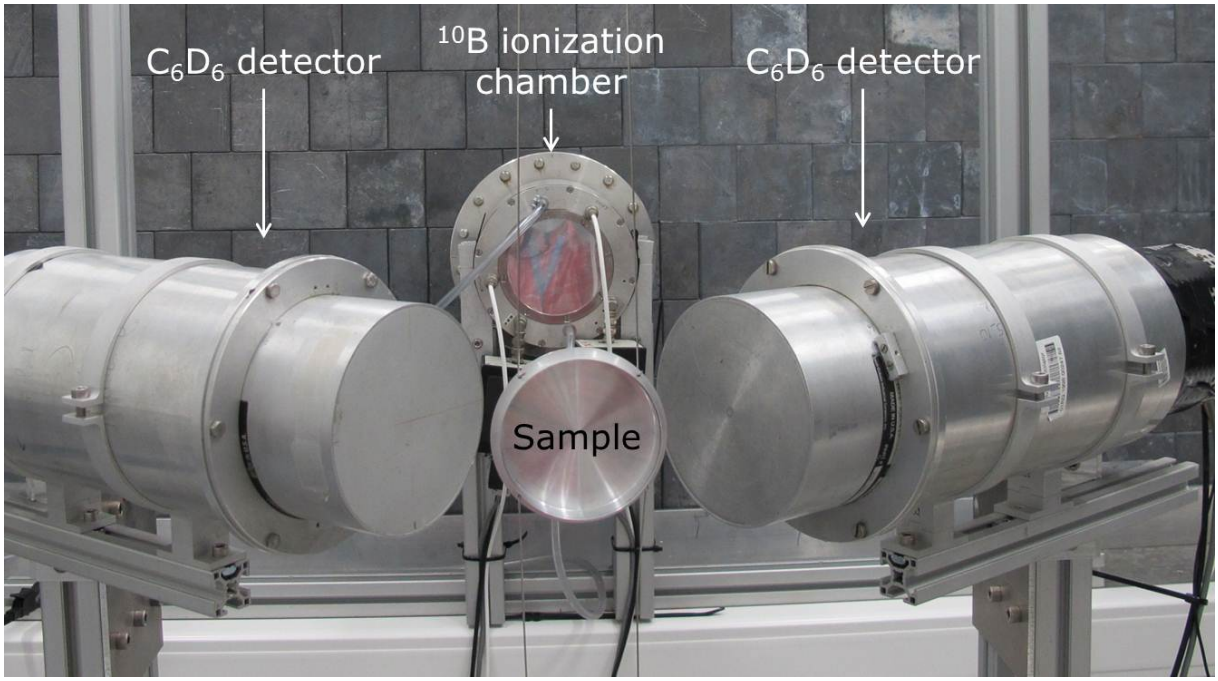

Fig. 29: Capture measurement set-up at a 12.5 m station of GELINA. The set-up consists of two C_6D_6 detectors and an ionisation chamber loaded with thin ^{10}B layers [18, 53].

from the sample, enter the measurement station or detector and slow down in the construction material of the measurement station or detector before creating a signal in the detector. The time and sample dependent component may be influenced by overlap neutrons. As with transmission measurements, the relative contribution of the different components strongly depends on the facility and detection system. The impact of overlap neutrons depends on the operating frequency and overlap filter that is used. The best way to determine this contribution is by measurements at a lower frequency as in e.g. Ref. [63, 64]. One way to assess the background due to scattered neutrons is by additional measurements with material for which the contribution due to the (n,γ) reaction can be neglected, e.g. ^{208}Pb or carbon. To separate the direct from the delayed component several measurements using various black resonance filters are required. When in beam γ-rays scattered by the sample also contribute to the background, the problem becomes even more complicated. The contribution due to in-beam γ-rays strongly depends on the type of neutron producing facility and will contribute in the low TOF (high energy) region. For example, the 2.2 MeV γ-ray can be an important background component for capture measurements, as in e.g. the capture experiments at the n_TOF facility presented in Ref. [54]. Its contribution stongly depends on the size of the moderator and can be reduced by adding a neutron poison to the moderator. This background contribution can be reduced by using borated water as a moderator [65].

A capture detection system consisting of two C_6D_6 detectors, installed at a 12.5m measurement station of GELINA, is shown in Fig. 29 [18, 53]. The background conditions for this system are given in Fig. 30. The response for a 1 mm-tick ^{197}Au sample is compared with the total background and its components. The measurements were performed with a fixed Na and S black resonance filter in the beam. These filters are used to control the background level and reduce bias effects due to the background correction. Due to the presence of a S black resonance filter the contribution of in-beam γ-rays scattered by the sample was strongly reduced. The total background B_γ can be estimated by [6, 53]:

$$B_\gamma = a_0 + k_1 C_0 + k_2 R_n (C_{Pb} - C_0) \tag{26}$$

where a_0 is the total time independent contribution, and C_0 and C_{Pb} are the TOF-spectra from measurements with no sample and with an almost purely scattering ^{208}Pb sample, respectively. The spectra

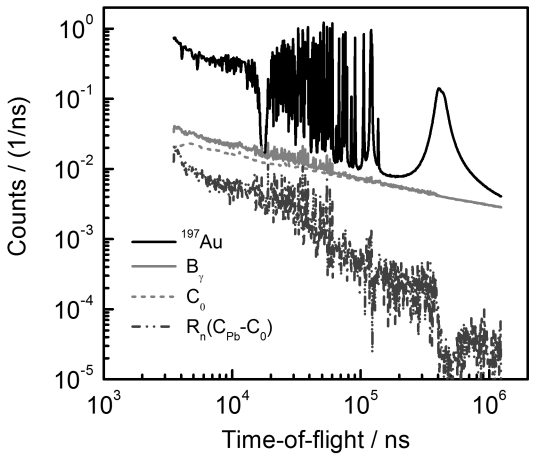

Fig. 30: The response of a C_6D_6 detector system as a function of TOF for a 1.0 mm ^{197}Au sample obtained at GELINA is compared with the contribution of the different background components. Data taken from Ref. [6]

are all normalized to the same total neutron intensity. The correction factor R_n accounts for the difference in scattering yield of the gold and lead samples.The background is clearly dominated by the time dependent and sample independent background component C_0. The contribution of the sample dependent component is over the whole energy range less than 1%. The factors k_1 and k_2 can be introduced to account for uncertainties due to systematic effects in the background model. It has been shown that uncertainties of 3% and 5% can be reached when fixed background filters are used, i.e. k_1 = 1.00 $\pm$ 0.03 and k_2 = 1.00 $\pm$ 0.05.

The energy dependence of the neutron flux can be determined by a measurement of a neutron induced reaction for which the energy dependence of the reaction cross section is well known [66]. To avoid artificial structures in the experimental yield Y_{exp}, reactions with a smooth cross section as function of neutron energy are preferred [6]. In the region below a few hundred keV flux measurements are predominantly based on the ^{6}Li(n,t)α, ^{10}B(n,α)^{7}Li and ^{10}B(n,$\alpha\gamma$)^{7}Li reactions. At energies above 0.5 MeV the ^{235}U(n,f) reaction is mostly used [67].

At GELINA double Frisch-gridded ionization chambers, with a common cathode, are mostly used to determine the neutron flux for neutron energies below 150 keV [18, 53, 67]. Thin layers of ^{10}B, with an areal density of about 40 μg/cm^2, are evaporated back-to-back on a 30-μm thick aluminum backing, which acts as the cathode. The chamber is almost transparent for the neutron beam. A back-to-back configuration, rules out a systematic bias effect related to the forward-to-backward emission ratio [68]. The background for flux measurements with such a chamber is determined by an analytical expression applying the black-resonance technique, similar as the background correction for transmission. The main difference with the Li-glass scintillator is that the contribution of the 2.2 MeV γ-ray can be neglected. Based on measurements using different combinations of black resonance filters, the uncertainty due to the background model was evaluated. Under the constraint of using at least one fixed background filter, this uncertainty is $\leq$ 3% [6].

2.5 Data reduction

The output in TOF-experiments are count rate spectra with a significant number of channels. The data reduction of these spectra is challenging, in particular when the full covariance of each step in the data reduction process is propagated. In addition, significant memory is required to store the covariance information of the final experimental observable as a covarinance matrix.

To process data from TOF-experiments the AGS concept and code package has been developed at

the EC-JRC-IRMM [69,70]. The concept is based on a compact formalism to propagate all uncertainties starting from uncorrelated uncertainties due to counting statistics. It stores the full covariance information after each operation in a concise, vectorized way and ensures that the resulting covariance matrix is always positive definite. The AGS code includes all arithmetic operations of spectra. In addition, more advanced operations as dead time correction, least squares background fitting, reading of data files in ENDF format, projection of spectra on different time axes and bin averaging can be executed. The AGS concept results in a substantial reduction of data storage volume and provides a convenient structure to verify the various sources of uncertainties through each step of the data reduction process. The use of the AGS concept has been recommended in a consultants' meeting organized by the IAEA [71] to report TOF cross section data in the EXFOR data library [72, 73].

Assuming that a spectrum denoted by the vector $\vec{z}$ of n channels is deduced using a parameter vector $\vec{p}$ with dimension m, which introduces m correlated uncertainty components, the covariance matrix $\boldsymbol{V}_{\vec{z}}$ of $\vec{z}$ can always be expressed as:

$$\boldsymbol{V}_{\vec{z}} = \boldsymbol{U}_{\vec{z}} + \boldsymbol{S}_{\vec{z}}\boldsymbol{S}_{\vec{z}}^{T} \tag{27}$$

where $\boldsymbol{U}_{\vec{z}}$ is a diagonal matrix with the uncorrelated variances as elements. The S-matrix $\boldsymbol{S}_{\vec{z}}$ is given by $\boldsymbol{S}_{\vec{z}}(\vec{p}) = \boldsymbol{D}_f(\vec{p})\boldsymbol{L}_{\vec{p}}$, where $\boldsymbol{D}_f$ is the sensitivity matrix of the functional data reduction step f with respect to the parameter vector $\vec{p}$ and $\boldsymbol{L}_{\vec{p}}$ is the Cholesky decomposition of the covariance matrix of the parameter vector. The S-matrix $\boldsymbol{S}_{\vec{z}}$ has the dimension $(n \times m)$. Each additional channel-to-channel operation introducing correlated uncertainties, increases the number of columns of the S-matrix by the number of parameter uncertainties, however, maintaining the structure given in Eq. (27). Also combining two spectra, each with a covariance in the form of Eq. (27), maintains the separation of uncorrelated uncertainty and the S-matrix.

When the number of channels is larger than the total number of parameters, the structure in Eq. (27) is much more efficient compared to the use of the full covarianc matrix of dimension $(n \times n)$. It requires the storage of the uncorrelated component $\boldsymbol{U}_{\vec{z}}$ as a vector with n entries and the matrix $\boldsymbol{S}_{\vec{z}}$ with dimension $(n \times m)$. In addition, the separation of the covariance matrix into the uncorrelated component and the S-matrix is very practical for further use of this matrix. For example in NRTA and NRCA the experimental observables (Y_{exp} and T_{exp}) are used to fit areal densities by a least squares adjustment of a model to the experimental data. The determination of the fitted areal densities together with their covariance matrix is mostly based on arithmetic expressions, which involve the inverse of the full data covariance matrix of the experimental observables. In case the experimental observable used in the fitting procedure consists of a significant number of channels, the inversion of the data covariance matrix is numerically challenging. Using the structure of Eq. (27) the inversion can be significantly simplified. By using the Woodbury matrix identity [74], the inverse of $\boldsymbol{V}_{\vec{z}}$:

$$\boldsymbol{V}_{\vec{z}}^{-1} = \left(\boldsymbol{U}_{\vec{z}} + \boldsymbol{S}_{\vec{z}}\boldsymbol{S}_{\vec{z}}^{T}\right)^{-1} , \tag{28}$$

becomes:

$$\boldsymbol{V}_{\vec{z}}^{-1} = \boldsymbol{U}_{\vec{z}}^{-1} - \boldsymbol{U}_{\vec{z}}^{-1}\boldsymbol{S}_{\vec{z}}\left(\boldsymbol{I} + \boldsymbol{S}_{\vec{z}}^{T}\boldsymbol{U}_{\vec{z}}^{-1}\boldsymbol{S}_{\vec{z}}\right)^{-1}\boldsymbol{S}_{\vec{Z}}^{T}\boldsymbol{U}_{\vec{z}}^{-1} , \tag{29}$$

with $\boldsymbol{I}$ being the identity matrix. In Eq. (29) only the uncorrelated part of the covariance matrix and the term $\left(\boldsymbol{I} + \boldsymbol{S}_{\vec{z}}^{T}\boldsymbol{U}_{\vec{z}}^{-1}\boldsymbol{S}_{\vec{z}}\right)$ need to be inverted. The latter is a $(m \times m)$ matrix with m being the total number of correlated uncertainty components. The inversion of these two terms is by far more efficient than inverting $\boldsymbol{V}_{\vec{z}}$. A similar procedure called implicit data covariance method has also been applied in Ref. [75].

3 Data analysis

Two different approaches to analyze NRTA and NRCA data can be distinguished. The first is based on a full methodological approach, in which the areal densities are derived from a resonance shape analysis based on a least squares adjustment to experimental data. The second, more empirical approach, relies

on the use of calibration samples of known compositions and the experimental signatures are the areas in the resonance dips and peaks present in the data for NRTA and NRCA, respectively.

3.1 Resonance shape analysis

The areal density of the nuclides present in the sample can be derived by a least squares adjustment, that is by minimizing the expression:

$$\chi^2(\vec{\theta}) = \left(\vec{z}_{exp} - \vec{z}_M(\vec{\theta})\right)^T \boldsymbol{V}_{\vec{z}_{exp}}^{-1} \left(\vec{z}_{exp} - \vec{z}_M(\vec{\theta})\right), \tag{30}$$

where $\vec{z}_M(\vec{\theta})$ is the model describing the experimental data $\vec{z}_{exp}$, with covariance matrix $\boldsymbol{V}_{\vec{z}_{exp}}$, and $\vec{\theta}$ are the model parameters. The minimum condition of Eq. (30) is equivalent to a maximum likelihood when the probability distribution of the observable is a normal distribution [3, 76]. Without any additional information on the probability distribution of $\vec{z}$ this can always be supposed based on the principle of maximum entropy [3,76]. The fitted parameters, describing in the best way the experimental data, can be found in an iterative way by searching for the steepest decent. For a linear model the minimum condition is also found for:

$$\vec{\theta} = \left(\boldsymbol{G}_{\vec{\theta}}^T \boldsymbol{V}_{\vec{z}}^{-1} \boldsymbol{G}_{\vec{\theta}}\right)^{-1} \left(\boldsymbol{G}_{\vec{\theta}}^T \boldsymbol{V}_{\vec{z}}^{-1} \vec{z}_{exp}\right). \tag{31}$$

The sensitivity matrix $\boldsymbol{G}_{\vec{\theta}}$ has as elements the partial derivatives of $\vec{z}_{exp}$ with respect to $\vec{\theta}$. In case the observables follow a normal distribution the quality of the fit can be verified by comparing the χ^2 per degree of freedom with its expectation value. For an adequate description of the data this value approaches unity for a large number of degrees of freedom. The quality of the fit can also be verified by the residual for each data point. The residual $\vec{r}$ is given by:

$$\vec{r} = \frac{\vec{z}_{exp} - \vec{z}_M(\vec{\theta})}{\vec{U}_{\vec{z}}}. \tag{32}$$

The covariance of the estimated parameters based on conventional uncertainty propagation (CUP) is given by:

$$\boldsymbol{V}_{\vec{\theta}} = \left(\boldsymbol{G}_{\vec{\theta}}^T \boldsymbol{V}_{\vec{z}}^{-1} \boldsymbol{G}_{\vec{\theta}}\right)^{-1}. \tag{33}$$

In case the covariance of the experimental data is given in the AGS format the covariance matrix of the adjusted parameters can be expressed as:

$$\boldsymbol{V}_{\vec{\theta}} = \boldsymbol{V}_{\vec{\theta}}^U + \boldsymbol{V}_{\vec{\theta}}^U \boldsymbol{K} \left(\boldsymbol{I} + \boldsymbol{S}_{\vec{z}}^T \boldsymbol{U}_{\vec{z}}^{-1} \boldsymbol{S}_{\vec{z}} - \boldsymbol{K}^T \boldsymbol{V}_{\vec{\theta}}^U \boldsymbol{K}\right)^{-1} \boldsymbol{K}^T \boldsymbol{V}_{\vec{\theta}}^U, \tag{34}$$

with the matrix $\boldsymbol{K}$ defined as:

$$\boldsymbol{K} = \boldsymbol{D}_F^T(\vec{\theta}) \boldsymbol{U}_{\vec{z}}^{-1} \boldsymbol{S}_{\vec{z}}. \tag{35}$$

The first term $\boldsymbol{V}_{\vec{\theta}}^U$ is due to the contribution of the uncorrelated uncertainty components:

$$\boldsymbol{V}_{\vec{\theta}}^U = \left(\boldsymbol{D}_F^T(\vec{\theta}) \boldsymbol{U}_{\vec{z}}^{-1} \boldsymbol{D}_F(\vec{\theta})\right)^{-1}. \tag{36}$$

The second term in Eq. (34) results from the contribution due to the correlated uncertainty components. Eqs.(34,35,36) show that the inversion of the full covariance matrix can be avoided when the experimental covariance is given in the AGS format and the calculation of the covariance matrix of optimized parameters is based on CUP. Becker et al. [70] have shown that the AGS format also provides a convenient format to determine the covariance matrix of the fitted parameters by Monte Carlo simulations [77] or marginalization [78].

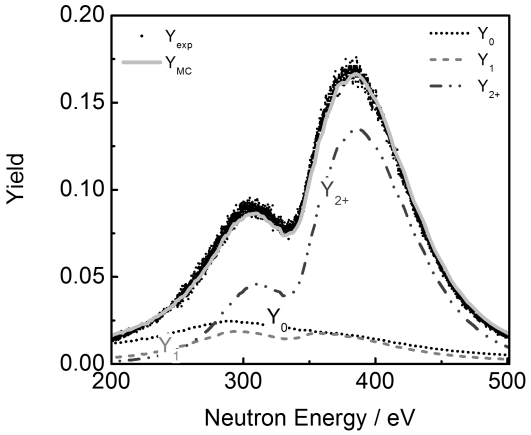

Fig. 31: Comparison of experimental capture yield for a 3-mm thick Mn target with the theoretical yield obtained from full Monte Carlo simulations. The contributions of primary events Y_0, capture after one scattering Y_1 and capture after at least two neutron scattering interactions Y_{2+} are shown.

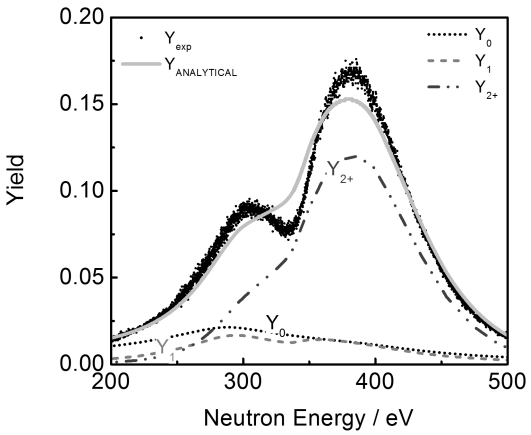

Fig. 32: Comparison of experimental capture yield for a 3-mm thick Mn target with the theoretical yield obtained from analytical approximations. The contributions of primary events Y_0, capture after one scattering Y_1 and capture after at least two neutron scattering interactions Y_{2+} are shown.

The model parameters $\vec{\theta} = (\vec{\eta}, \vec{\kappa})$ include reaction model parameters and experimental parameters which are represented by the vectors $\vec{\eta}$ and $\vec{\kappa}$, respectively. The theoretical estimate $\vec{z}_M(t, \vec{\theta}, \vec{\kappa})$ in Eq. (30) is the result of a folding to account for the response function of the TOF-spectrometer:

$$\vec{z}_M(t, \vec{\eta}, \vec{\kappa}) = \frac{\int R(t, E, \vec{\kappa}) \vec{z}'(E, \vec{\eta}, \vec{\kappa}) dE}{\int R(t, E, \vec{\kappa}) dE}, \tag{37}$$

where $R(t, E, \vec{\kappa})$ is the response function of the TOF-spectrometer. The latter depends on experimental conditions such as the accelerator pulse width, the target-moderator characteristics, flight path length and detector characteristics. The quantity $\vec{z}'(E, \vec{\eta}, \vec{\kappa})$ represents the theoretical estimate of the observable, i.e. the transmission $T(E, \vec{\eta}, \vec{\kappa})$ or reaction yield $Y(E, \vec{\eta}, \vec{\kappa})$. Its calculation requires a theoretical model including a nuclear reaction formalism (i.e. R-matrix formalism [2]) and models to account for experimental effects. Hence, the theoretical model depends on both resonance parameters, determining the cross sections, and experimental parameters. The latter describe the response function, detector characteristics and sample properties, including the areal density of the nuclides present in the sample.

The least squares adjustment can be performed by a resonance shape analysis (RSA) code, such as REFIT [42]. This code, which has been developed to parameterize cross section data in terms of resonance parameters, is based on the Reich-Moore approximation [79] of the R-Matrix formalism [2]. It accounts for various experimental effects such as sample inhomogeneities, Doppler broadening, and the response of the TOF spectrometer and detectors. For the analysis of capture data special modules have been included to account for self-shielding and multiple interaction events, to correct for γ-ray attenuation in the sample and for the neutron sensitivity of capture detection systems [6, 80].

The calculation of the theoretical capture yield, in particular the contribution of multiple interaction events, is rather complex. For a parallel neutron beam and samples with simple geometries and composition, analytical expressions have been implemented in REFIT [42]. In case of one scattering followed by a reaction event and a simple geometry, exact expressions can be derived based on asymptotic free gas scattering. For more than one scattering (m $\geq$ 2), an additional assumption is made that neutrons are uniformly distributed within the sample. In case of complex geometries, relatively thick samples and/or strong scattering resonances, Monte Carlo simulations are required to correctly describe

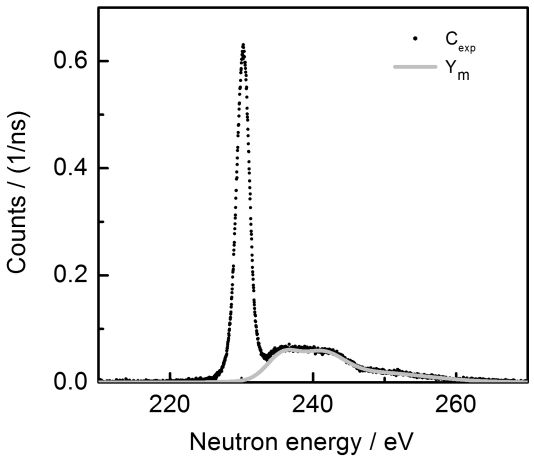

Fig. 33: Results from an analysis of the profile around the 230-eV Cu-resonance resulting from an NRCA measurement of a 14-mm-thick prehistoric axe. Data taken from Ref. [4].

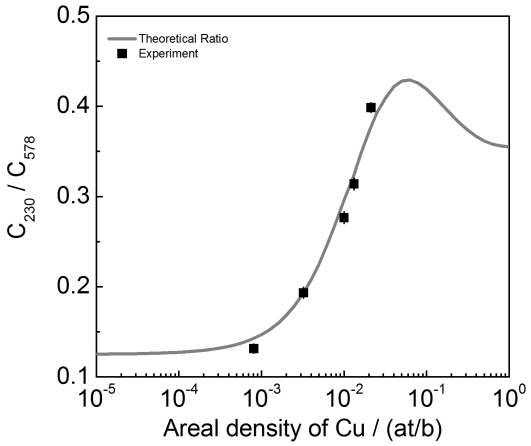

Fig. 34: Ratio of counting rates of two Cu-resonances (230 and 578 eV) as function of the areal density of Cu measured using copper plates with known thickness (symbols). The theoretical ratio was calculated using Eq. (39). The experimental data were taken from Ref. [81].

the capture yield [80]. This is illustrated in Figs. 31 and 32, which compare the experimental capture yield for a 3-mm thick Mn sample, the yield obtained with full Monte Carlo simulations and the yield based on an analytical approximation. The contribution of the different types of interactions, i.e. primary events Y_0, capture after one scattering Y_1 and capture after at least two neutron scattering interactions Y_{2+}, are given. This comparison demonstrates that the discrepancies between experimental yield and the one obtained from analytical approximations are primarily due to the contributions of the Y_{2+} events.

3.2 Calibration approach

A full methodological approach in case of NRCA is not always evident. Besides accurate resonance parameters it also requires a detailed information about the neutron beam characteristics, detection system and even sample properties. Therefore, a more empirical approach relying on the use of calibration samples of known composition, is often applied [4,52]. The experimental signature for such an approach is the net area of the peak of a resonance. The ratio of the areal density of nuclides X and Y present in the sample is derived from a ratio of net peak areas:

$$\frac{n_X}{n_Y} = K_{\mu,\lambda}\frac{F_\lambda}{F_\mu}\frac{C_\mu}{C_\lambda}, \tag{38}$$

with n_X and n_Y being the areal densities of nuclide X and Y, respectively. The net peak areas for the resonances μ and λ of nuclides X and Y, respectively, are denoted by C_μ and C_λ. The corresponding corrections for self-shielding are F_μ and F_λ. The calibration factor $K_{\mu,\lambda}$ is determined from measurements under identical experimental conditions using representative samples with a known composition and thickness. This factor accounts for the nuclear data and sample independent experimental parameters such as the the effective neutron flux and the detection efficiency and geometry.

The simplest approach to determine the area of a resonance peak is by summing up all counts under the resonance peak and subtracting the background contribution. In case of overlapping resonances and a substantial contribution from multiple interaction events, a fitting procedure based on Voigt profiles and a parametric description of the multiple interaction events can be applied. The width of the Voigt

profile accounts for both the resolution of the spectrometer and the Doppler broadening. An example of such a parameterization is shown in Fig. 33. In this figure the response in the region of the 230 eV resonance of Cu resulting from measurements of a 14-mm thick prehistoric axe [4] is given. There is a fairly good agreement with the profile obtained by Monte Carlo simulations shown in Fig. 24. Such a parameterization of the resonance profile is possible for resonances where the average neutron energy loss in a collision is larger than the width of the resonance. This is mostly the case at high energies and for light nuclei. For low energy resonances, however, a large fraction of multiple interaction events produces counts close to the resonance peak and a parametric fitting can not be applied. In that case, a resonance shape analysis has to be applied.

To determine the relative areal densities from Eq. (38) a correction for self-shielding is needed. The effective self-shielding correction F_μ is an average over the resonance μ of the self-shielding in Eq. (23):

$$F_\mu = \frac{\int \sigma_\gamma(E) F(E) dE}{\int \sigma_\gamma(E) dE}. \tag{39}$$

Applying Eq. (39) it is assumed that the flux is constant over the resonance. For inhomogeneous objects the self-shielding correction must be averaged over the areal density distribution. To account for the variation in areal density, the correction can be calculated based on the analytical expressions Eq. (23) and Eq. (39) using an effective areal density. The different behavior of the self-shielding as a function of the areal density in Fig. 23 suggests that the ratio of areas from resonances with different strengths for a given element can be used to determine the effective areal density [81]. This is illustrated in Fig. 34, where the ratio of the areas of the Cu resonances at 230 eV and 578 eV is plotted as a function of the areal density of Cu. The experimental data in Fig. 34 result from measurements with Cu samples of known thicknesses. The full line is based on the theoretical esimates using Eq. (23) and Eq. (39). In Ref. [81] the effective areal density derived from such a ratio together with the area of the object was used to determine the weight of an object. The resulting weight (13.0 ± 0.5 g) was in very good agreement with the actual weight 13.25 g of the object. On the other hand, the data in Fig.34 demonstrate that for relatively thick samples this procedure does not allow an uambiguous determination of the effective areal density. An alternative more accurate procedure, which has been proposed in Refs. [82, 83], is based on a least squares analysis of ratios of resonance areas with the relative abundances and an effective areal density as free parameters. To avoid large corrections for self-shielding and multiple interaction events, the analysis of weak resonances is mostly preferred.

Nevertheless, the occurence of resonances of different strenghts is a powerful feature of NRCA. Strong resonances are very suitable for detecting minor and trace elements, often in the ppm range. The weaker resonances are preferred to quantify the major elemental components of the object and the combination of resonances with different strengths can be used to correct for self-shielding. In case of stong overlapping resonances and a substantial contribution of multiple interaction events, the calibration approach is not applicable and a resonance shape analysis is required.

4 Applications

Neutron resonance spectroscopy can be applied for a variety of applications in diverse fields, such as archeological studies, determination of the fissile content of nuclear material for nuclear safeguards and security, characterisation of reference materials for cross section measurements and of organic samples in the biomedical field, combatting illicit traffick by detection of drugs and explosives, temperature measurements, and the study of fundamental properties of materials.

4.1 Archaeology

In the course of several years NRCA has been applied at GELINA to study objects of cultural heritage interest [4]. The majority of the data results from measurements at the 12.5 m capture measurement

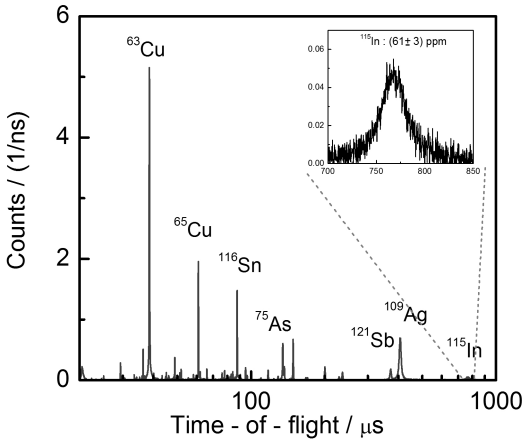

Fig. 35: Time-of-flight spectrum resulting from NRCA measurements on a fragment of a vessel or cauldron dated to the 7^{th} century BC. The results of these measurements have been reported in Ref. [81].

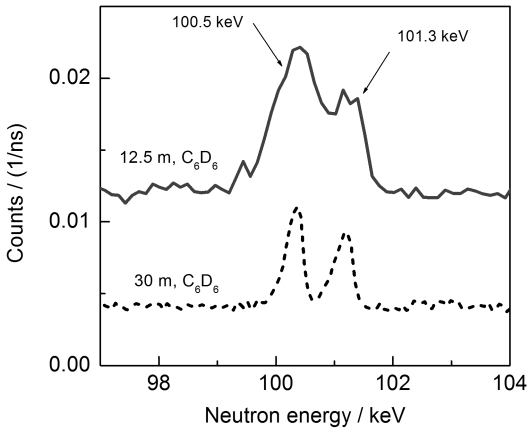

Fig. 36: Capture spectrum of a marble sample using C_6D_6 detection set-ups at a 14 m and a 30 m station of GELINA. The results of these measurements have been reported in Ref. [87].

station shown in Fig. 29. More details about this measurement station can be found in Refs. [18, 53]. Results from NRCA and Neutron Diffraction (ND), two complementary non-destructive neutron interrogation techniques, are often combined to study alloys in terms of both elemental and phase compositions and to provide information about the origin and usage of the objects, the fabrication methods and trade relations. Most of the archaeological applications so far are related to copper-alloy artefacts. Apart from Cu, they contain Sn or Zn as other major elements, and As, Ag, Sb, Co, Fe, In and Pb as minor or trace elements.

Fig. 35 shows a TOF-spectrum resulting from NRCA measurements by Postma et al. [81] on a fragment of a vessel (or cauldron) that was excavated at 60 km south of Rome (IT). The object dated from the 7^{th} century BC. The elemental composition deduced from this spectrum is given in Table 2. This example illustrates the potential of NRCA for elemental analysis and reveals that elements with resonances in the eV region can be detected in the parts per million range. Also in Ref. [84] the amount of In has been observed in a set of bronze artifacts down to a few parts per million. Fig. 35 evidences the advantage of NRCA compared to other active neutron interrogation techniques such as PGA [7]. Performing NRCA one can always select an optimum region in the TOF spectrum where the elements with a small contribution, e.g. In in Fig. 35, are not hampered by resonances of other elements with a large yield. In this region of the TOF-spectrum the response in the detector is fully dominated by the minor element. In a PGA experiment, which is also based on the detection of prompt γ-rays, the observed γ-ray spectrum will be dominated by the presence of the element with the largest cross section and this in almost the whole energy region. A detailed comparison between NRCA and PGA can be found in Ref. [52].

Postma et al. [85] verified the authenticity of a series of bronze statuettes from the National Museum of Antiquities in Leiden (NL). The statuettes were part of a collection of Etruscan objects. With the smelting technique used in the Etruscan period only minor amounts of zinc, with a relative abundance of less than 1 wt% are expected. Based on the elemental composition derived by NRCA, in particular the relative amount of zinc, it was possible to distinguish the fake from genuine statuettes.

The elemental composition and structure of a precious and very well preserved ceremonial sword of the Bronze-Age period was studied by Postma et al. [83] based on results of NRCA and ND experiments at GELINA and ISIS, respectively. This sword was on loan from the National Museum of Antiquities in Leiden (NL). The tin-bronze ratio and the relative amounts of some minor elements (Sb,

Table 2: Elemental composition of a fragment of a vessel (or cauldron) from the 7^{th} century BC deduced using NRCA. Data taken from Ref. [81]. Uncertainties are only due to counting statistics and background contributions.

Element	Isotope	Resonance eV	Fraction wt.%
Cu			77.76 ± 0.11
	^{63}Cu	579.0	
	^{65}Cu	230.0	
Sn			20.85 ± 0.10
	^{112}Sn	94.8	
	^{116}Sn	111.2	
	^{117}Sn	38.8	
	^{118}Sn	45.7	
	^{119}Sn	222.6	
	^{120}Sn	427.5	
	^{122}Sn	1756.0	
	^{124}Sn	62.0	
As			0.34 ± 0.01
	^{75}As	47.0	
Sb			0.196 ± 0.021
	^{121}Sb	6.24	
	^{123}Sb	21.4	
Ag			0.090 ± 0.21
	^{107}Ag	16.3	
	^{109}Ag	5.2	
Fe			0.770 ± 0.09
	^{56}Fe	1147.4	
In			0.0061 ± 0.0003
	^{115}In	1.46	

As, Ag, In) were determined. The presence of cobalt supported the assumption that the sword originated from the North Alps-Danuba region. They also studied the construction of the hilt-blade connection. From the elemental composition along the length of the sword and a radiograph, they concluded that the blade and the hilt were cast separately and that it was manufactured as a potentially functional weapon. The elemental composition of the blade and the hilt are compared in Table 3.

In Ref. [84] the bulk elemental composition of twelve socketed axes from the Late Bronze Age were determined by NRCA. In addition, information about the crystalline structure, the occurrence of sulfides and oxides and intermetallic compounds was obtained from ND. The relative amounts of Sb, As, Ag and Ni were deduced by NRCA. The Ni content was derived from capture measurements at a 30 m station of GELINA equipped with two C_6D_6 detectors. The results of the 30 m measurements were also used to derive upper limits for the amount of Fe and Pb.

Schut et al. [82] used results form NRCA and ND to study technological and metallurgical aspects of a series of Roman bronze water taps, which have been excavated in the Netherlands. Bulk elemental analysis by NRCA and phase analyses by ND were carried out to determine differences among the taps and to learn more about the fabrication process. An example of an elemental composition is reported in Table 4. This table illustrates that they were able to determine the relative amounts of Fe and Pb, which

Table 3: Elemental composition of a ceremonial sword of the Bronze-Age period deduced by NRCA. Data taken from Ref. [83]. Uncertainties are only due to counting statistics and background contributions.

Element	Composition blade wt.%	Composition hilt wt.%
Cu	88.44 ± 0.15	86.40 ± 0.15
Sn	11.06 ± 0.14	13.05 ± 0.15
Sb	0.172 ± 0.009	0.203 ± 0.017
As	0.080 ± 0.009	0.106 ± 0.017
Ag	0.056 ± 0.004	0.046 ± 0.007
In	0.011 ± 0.001	0.010 ± 0.002
Co	0.012 ± 0.003	0.004 ± 0.001
Zn	0.177 ± 0.053	0.181 ± 0.026

Table 4: Elemental composition of a Roman water tap determined by NRCA. Data taken from Ref. [82]. Uncertainties are only due to counting statistics and background contributions.

Element	Composition wt.%
Cu	69.92 ± 1.67
Sn	6.07 ± 0.22
Sb	0.117 ± 0.003
As	0.069 ± 0.003
Ag	0.067 ± 0.021
Zn	0.252 ± 0.022
Fe	0.084 ± 0.021
Pb	23.4 ± 1.8

Table 5: Ca/P ratio in a sample of hydroxyapatite powder and a cow rib and Cl/Ca ratio in marble based on results of NRCA compared with the results of a chemical analysis and neutron activation analysis. Data taken from Ref. [87]. Uncertainties are only due to counting statistics and background contributions.

Sample	Elemental Ratio	Composition (g/g) NRCA	Other Method	
Hydroxyapatite	Ca/P	2.0 ± 0.1	2.05 ± 0.02	Chemical Analysis
Cow Rib	Ca/P	2.2 ± 0.2	2.13 ± 0.32	NAA
Marble-Cl	Cl/Ca	0.0018 ± 0.0002	0.00171 ± 0.00006	NAA

were derived from measurements at the 30 m capture station. The determination of Pb by other active neutron interrogation techniques is not evident. NAA in a thermal neutron beam is almost excluded since a radioactive product can only be produced by a threshold reaction such as ^{204}Pb(n,2n)^{203}Pb [86]. The advantage of using a 30 m station to analyze high energy resonances was also demonstrated by Perego et al. [87]. They exploited the resolution of the 30 m capture station of GELINA to determine the Cl/Ca ratio in a piece of marble and the Ca/P in a sample of hydroxyapatite powder and a cow rib. The Cl/Ca and Ca/P ratios from NRCA are in good agreement with the values obtained by NAA and mass spectrometry as shown in Table 5. The difference in resolution resulting from measurements at the 12.5 m and 30 m station is illustrated in Fig. 36 for a measurement with the same marble sample and similar detection systems consisting of two C_6D_6 detectors.

The potential of NRTA to study bronze artefacts by a full methodological approach, i.e. applying a resonance shape analysis of the experimental transmission without any calibration requirements, has been demonstrated in Ref. [5]. A set of copper alloy reference objects, which have been certified for the amount of Cu and relative amounts of As, Pb, Sn and Zn, were measured at a 25 m transmission station of GELINA. The transmission as a function of neutron energy together with the result of a resonance shape analysis for two reference standards are shown in Figs. 37 and 38. The certified elemental compositions and the ones resulting from a resonance shape analysis are compared in Table 6. The data in Table 6 reveal a good agreement between the NRTA results and the certified values. For the analysis the reso-

Table 6: Elemental composition of two reference samples measured with NRTA and the certified values. Data taken from Ref. [5]. Uncertainties are only due to counting statistics and background contributions.

Element	Elemental composition (atomic fraction)			
	Standard A		Standard B	
	NRTA	Certified	NRTA	Certified
Cu	0.8553 ± 0.0043	0.8675 ± 0.0001	0.8360 ± 0.0042	0.8360 ± 0.0001
Sn	0.0391 ± 0.0004	0.0398 ± 0.0012	0.0092 ± 0.0005	0.0105 ± 0.0004
Zn	0.0718 ± 0.0010	0.0671 ± 0.0025	0.1480 ± 0.0007	0.1515 ± 0.0050
As	0.0019 ± 0.0001	0.0018 ± 0.0001	0.0013 ± 0.0001	0.0008 ± 0.0001
Pb	0.0259 ± 0.0026	0.0236 ± 0.0009	0.0012 ± 0.0001	0.0011 ± 0.0001
Sb	0.0032 ± 0.0012		0.0000 ± 0.0000	
Mn	0.0027 ± 0.0010		0.0048 ± 0.0005	

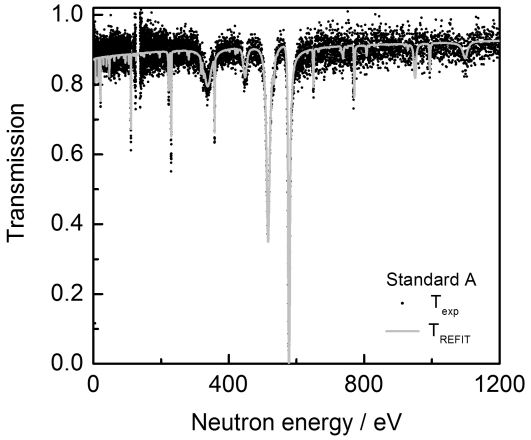

Fig. 37: Transmission as a function of neutron energy together with the result of a RSA using REFIT for reference sample A. Data based on Ref. [5].

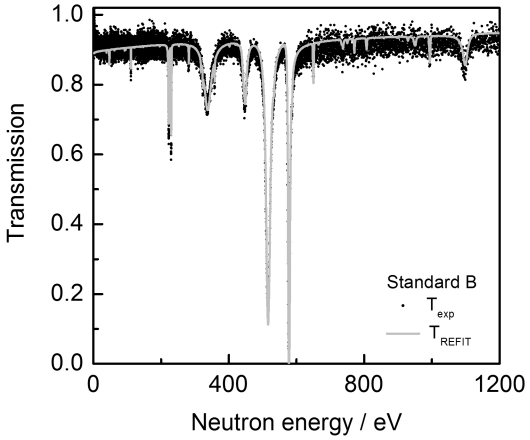

Fig. 38: Transmission as a function of neutron energy together with the result of a RSA using REFIT for reference sample B. Data based on Ref. [5].

nance parameters recommended in the JEFF-3.1.1 library were taken. However, to get a good agreement between the measured and fitted transmission most of the resonance energies had to be adjusted and for ^{63}Cu and ^{65}Cu the resonance parameters determined by Weigmann and Winter [88] were adopted. This suggests that an even better agreement can be obtained by improving the resonance parameters for these elements.

4.2 Characterisation of reference materials

NRCA and NRTA are very suitable to characterize reference materials which are used for cross section measurements [89]. NRCA is preferred for elements with resonances below 5 keV, while for light elements or elements with strong s-wave resonances NRTA is mostly used. NRCA is extremely practical for the identification and quantification of impurities which have a high capture cross section in the thermal and epi-thermal resonance region, in particular when cross section data are requested with a high accuracy and low uncertainty [89]. In case of reference materials, the experimental conditions including the shape of the samples are mostly such that the methodological approach can be applied and the composition can be determined without special calibration requirements. Impurities with a high capture

cross section can be verified to a ppm level, as shown in Refs. [89, 90]. The relative amount of Ta ($\sim$ 100 ppm) and W ($\sim$ 0.05%) impurities in a Hf sample were derived by Moxon et al. [90] by a resonance analysis of capture data. Because of the extremely large capture cross section of ^{nat}Hf, such impurities are very difficult to be determined by PGA.

Moxon et al. [91] analyzed boron samples, consisting of powder boron metal cladded in aluminum, for the ^{10}B content by NRTA. The samples were used as neutron converters for absolute neutron flux measurements at a beam line of a nuclear reactor. NRTA was preferred since the resulting amount of ^{10}B is almost independent of the degree of oxidation of the sample. A similar characterisation by NRTA of a ^{10}B sample, which was used for an absolute determination of the neutron flux, has been reported by Blackmon et al. [92].

4.3 Nuclear materials

The use of NRTA for a quantitative non-destructive assay of spent and fresh nuclear fuel has been demonstrated by Priesmeyer et al. [93]. Low and high enriched samples with different burnups were characterized by transmission measurements, which were carried out at a fast-chopper time-of-flight spectrometer installed at a reactor. The areal densities of ^{131}Xe, ^{133}Cs, ^{152}Sm, ^{235}U, ^{238}U and ^{239}Pu were derived from the transmission profile below 20 eV. NRTA was also investigated at the former National Bureau of Standards [94–98], as a tool to determine the fissile content of fresh and spent fuel pins for safeguards applications. They performed measurements at a 5-m flight path of a 100 MeV linear electron accelerator and used ^{3}He one dimensional position sensitive proportional counters [94] and a two dimensional position sensitive micro-channel plate with a Li-glass as neutron converter [99]. The spatial resolution of the two dimensional detector was 0.75 mm. Using a position sensitive detector Behrens et al. [95] were able to produce quantitative two dimensional radiographs. The fresh fuel was characterized for the ^{235}U and ^{238}U areal density. For the spent fuel the relative abundances of 11 actinides and 5 fission products were derived. Schrack [96,97] applied NRTA to monitor the amount of ^{235}U in simulated nuclear waste, consisting of incinerator ash as matrix material and small concentrations of ^{235}U (between 4.8×10^{-4} g/cm^3 and 4.6×10^{-3} g/cm^3). The technique was demonstrated on sample sizes ranging from 2 liter bottles to 200 liter drums.

Noguere et al. [86] performed transmission measurements to determine the composition of a PbI_2 sample that was produced from a solution of radioactive waste originating from the French reprocessing facility at La Hague. NRTA was carried out at a 50 m transmission station of GELINA using a ^{6}Li glass scintillator. Prior to the analysis of the sample, capture and transmission measurements with a well-characterized ^{nat}I sample were carried out to determine accurate resonance parameters for ^{127}I and ^{129}I. The parameters for ^{206}Pb were taken from the work of Borella et al. [67]. For the other nuclides present in the sample the resonance parameters recommended in the JEFF-3.1.1 library were adopted. In addition to NRTA, representative samples were also analyzed by NAA and mass spectrometry. The results in Table 7 show that there is a very good agreement between the results obtained with the different methods. Table 7 also illustrates that from the results of NRTA the isotopic composition of lead could be derived. A part of the transmission that was sensitive to the presence of sulfur in the sample is shown in Fig. 39 together with the transmission only due to the sulfur.

In Ref. [89] results of NRCA on a set of well-characterized mixtures of depleted U_3O_8 powder and natural Gd_2O_3 powder are reported. The measurements were carried out at the 12.5 m capture station of GELINA following the experimental procedures recommended in Ref. [6]. The composition of each sample was derived from a resonance shape analysis with REFIT. For the analysis all parameters were taken from the JEFF-3.1.1 library. Figs. 40 and 41 show the result of such an analysis for two samples. The results from NRCA and the certified values are compared in Table 8. The certified values were based on the weight and stoichiometry of the U_3O_8 and Gd_2O_3 powder, the isotopic composition of natural Gd recommended in Ref. [100] and the isotopic composition of the depleted uranium. The latter was determined by mass spectrometry. The NRCA results are in very good agreement with the

Table 7: Elemental and isotopic composition of a PbI_2 sample that was produced from a solution of radioactive waste originating from the French reprocessing facility at La Hague deduced by NRCA, ICP-MS and NAA . Data taken from Ref. [86].

Element	Isotope	NRCA wt.%		ICP-MS wt.%		NAA wt.%	
I		20.5	±0.9	19.9	±0.5		
	^{127}I	3.4		3.4	±0.1	3.4	±0.1
	^{129}I	17.1		16.5			
Pb		53.5	±3.0	59.5	±0.2	51.1	±1.8
	^{204}Pb	0.8					
	^{206}Pb	12.8	±0.5				
	^{207}Pb	12.1	±0.3				
	^{208}Pb	27.8	±3.0				
O		15.2	±0.8	14.5	±1.5		
S		6.2	±0.4				

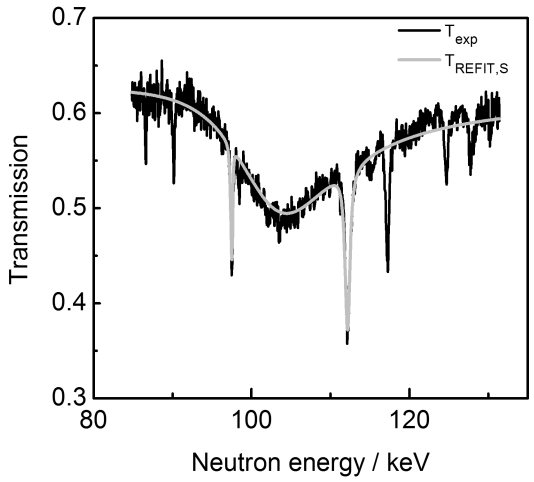

Fig. 39: Measured and calculated transmission spectra used to determine the composition of a PbI_2 sample that was produced from a solution of radioactive waste originating from the French reprocessing facility at La Hague [86].

certified values. For ^{155}Gd/^{238}U the largest deviation is 0.35%. The NRCA results for ^{157}Gd/^{238}U are systematically higher. This bias can be due to a bias in the resonance parameters for ^{157}Gd.

4.4 Fast neutron transmission

A comparison of the total cross sections for hydrogen, carbon, nitrogen and oxygen in Fig. 42 suggests that NRTA can be a valuable technique to analyse materials containing light elements [101, 102]. For such applications fast neutrons are required. Fast neutron beams can be produced at a charged particle accelerator utilizing (p,n) or (d,n) reactions. Possible candidates are D(d,n)^{3}He, T(d,n)^{4}He, ^{7}Li(p,n)^{7}Be, ^{9}Be(p,n)^{9}B and ^{9}Be(d,n)^{10}B [103–105]. Energy dependent transmission profiles can be obtained at mono-energetic neutron beams relying on the kinematics of the neutron production process or at a pulsed charged particle beam combined with the TOF technique [101, 102]. Mostly two dimensional (2D) images are produced using position sensitive neutron detectors. Therefore, these measurements are often

Table 8: Results of a characterisation of U_3O_8 and Gd_2O_3 powder mixtures with NRCA. The results obtained with NRCA are compared with the declared values. The latter are deduced from a combination of the weight, stoichiometry and isotopic composition. Data taken from Ref. [89].

U	Gd	n(^{155}Gd)/n(^{238}U))		n(^{157}Gd)/n(^{238}U))	
g	g	Declared	NRCA	Declared	NRCA
20.988	0.0536	5.77×10^{-4}	$(5.76 \pm 0.04) \times 10^{-4}$	6.10×10^{-4}	$(6.59 \pm 0.07) \times 10^{-4}$
20.608	0.5206	5.71×10^{-3}	$(5.73 \pm 0.01) \times 10^{-3}$	6.03×10^{-3}	$(6.53 \pm 0.02) \times 10^{-3}$
18.656	2.6240	3.13×10^{-2}	$(3.14 \pm 0.01) \times 10^{-2}$	3.36×10^{-2}	$(3.51 \pm 0.03) \times 10^{-2}$

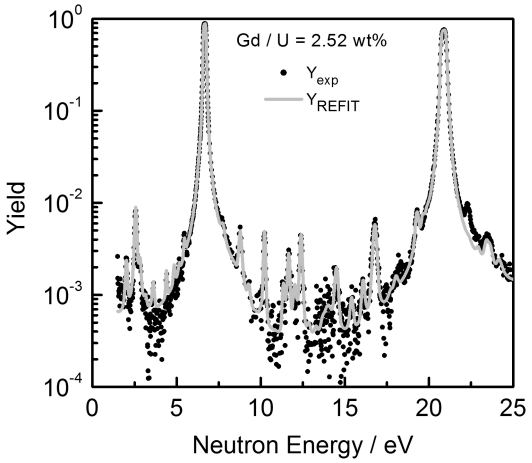

Fig. 40: Comparison of observed capture yield Y_{exp} for a U_3O_8 and Gd_2O_3 mixture with Gd/U = 2.52 wt% with the result of a RSA with REFIT. Data based on Ref. [89].

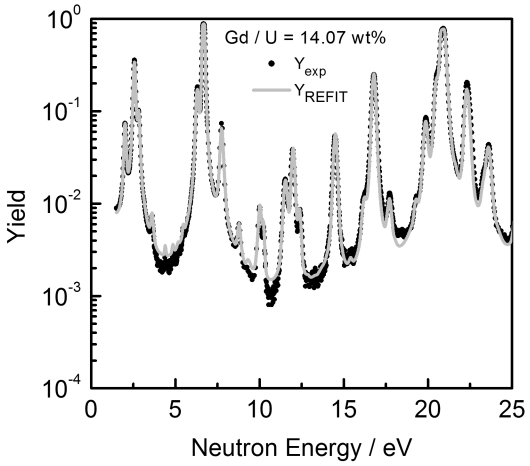

Fig. 41: Comparison of observed capture yield Y_{exp} for a U_3O_8 and Gd_2O_3 mixture with Gd/U = 14.07 wt% with the result of a RSA with REFIT. Data based on Ref. [89].

referred to as Fast Neutron Resonance Radiography [101, 102].

At the Massachusetts Institute of Technology the use of transmission profiles resulting from measurements at quasi-monoenergetic neutron beams is being investigated, mainly for the detection of explosives and contraband such as drugs [106, 107]. Neutrons are produced by the D(d,n)^{3}He reaction using a deuterium gas target [108]. The object and detector rotate together around the neutron source and are positioned at a set of angles to match the energies of resonance peaks and valleys between resonances. At each angle or energy, a 2D image is formed using a position sensitive neutron detector consisting of a plastic scintillator viewed by a CCD camera. The neutron energy resolution comes mainly from the energy loss of the charged particle in the target and is around 600 keV. The results of transmission measurements taken at different neutron energies form a set of linear equations, which are solved to derive the elemental composition. Watterson and Ambrosi [109] suggest to apply the method also for the localization of diamonds in a kimberline rock environment.

For TOF spectroscopic measurements the ^{9}Be(d,n)^{10}B reaction with deuterons of several MeV incident on a thick beryllium target [104, 110, 111] is preferred, due to its high yield and favourable thermal conductivity [105]. Metallic beryllium used as a target can be easily machined and is capable of tolerating beam currents in excess of 100 μA using conventional target designs and cooling. The reaction is exothermic with a positive Q-value of 4.36 MeV, which results in neutron spectra extending to high energies [105]. Pulsed fast neutron TOF spectroscopy, exploiting the characteristic energy dependence of the total cross sections for H, C, N and O in the 1 – 10 MeV range, was first proposed by Overley [112].

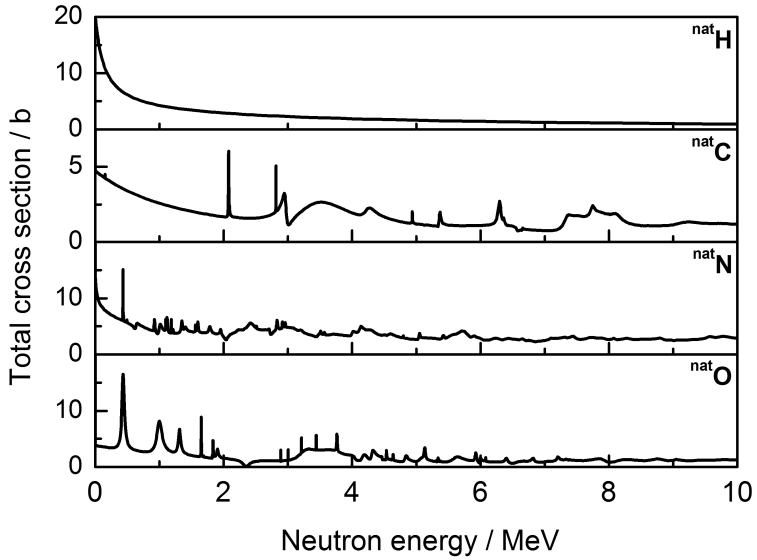

Fig. 42: Doppler broadened total cross section for neutron induced reactions in ^{nat}H, ^{nat}C, ^{nat}N, ^{nat}O at 300 K.

Overley and co-workers of the University of Oregon have studied the potential of this technique, not only for the detection of explosives and drugs but also to quantify the amount of H, C, N and O and their spatial distribution in agricultural products and organic compounds e.g. fructose, urea and melamine [112–116]. The areal density of H, C, N, and O are derived from a comparison with transmission data of pure elements. Contributions of other elements are lumped together as resulting from a fictitious element having an energy independent total cross-section. A similar TOF fast neutron spectrometer for identification of contraband in sealed containers was developed by Tensor Technology [117–119].

The systems of both the Oregon University and Tensor Technology are based on large-area detector arrays consisting of individual plastic scintillators with pixel sizes of a few centimeters. Hence, they pose an intrinsic limitation on the position resolution. To improve the position resolution for TOF spectroscopy at high intensity fast neutron beams, various detection systems have been developed and studied at the accelerator facility for fast neutron research of the Physikalisch-Technische Bundesanstalt (PTB), Braunschweig (Germany) [120]. Measurements have been carried out at the PTB using a broad-energy neutron beam produced by a nanosecond pulsed deuterium beam on a 3 mm thick Be target with a 1–2 MHz repetition rate. In addition, efforts are being made to improve the data analysis algorithms starting from nuclear data. Most of the developments are part of a collaboration between PTB and Soreq NRC (Israel). Detection systems for both time-resolved integrative and time-resolved event counting are investigated [121–123]. Progress made in the use of the time-resolved integrative optical neutron (TRION) detector has been reported in Refs. [121, 124–127]. Parameters affecting the image quality and the temporal resolution of the TRION detector are discussed in detail by Mor et al. in Ref. [126] and [127], respectively. For event-counting time-of-flight measurements, gaseous multi-step wire chambers combined with a polyethylene converter [122, 128] and a time resolved event-counting optical radiation detector [129] are studied.

4.5 Thermometry

As discussed in Sec. 2 and shown in Fig. 3 the observed resonance profile is influenced by the velocity distribution of the target nuclei in the lattice of the sample material. This distribution depends on the physical state of the sample (solid, liquid or gaseous) and its temperature. Therefore, the observed profile will be sensitive to these parameters and information about them can be derived from a resonance shape

analysis. The use of Doppler-broadened profiles for the remote determination of sample temperatures has already been demonstrated by Fowler and Taylor [130]. Other examples of the use of neutron resonance spectroscopy for thermometry are reported in Refs. [131–138].

As illustrated in Fig. 1, the cross sections for almost all nuclides show a resonance structure. However, only profiles which are dominated by the Doppler width, i.e. $\Delta_D > \Gamma$, can be used. This limits the application to low energy resonances of heavier nuclei. This problem can be solved by doping the sample of interest with an element with a suitable resonance [134]. On the other hand, since the resonance structures are due to nuclear processes, the lineshape is almost insensitive to changes in chemistry, provided that the sample temperature is high enough to avoid crystal binding effects. In addition, the technique is non-invasive, e.g. wiring of the sample, is not required [135]. Therefore, in case of high-temperature and high-pressure measurements neutron resonance spectroscopy for temperature measurements offers a number of advantages compared to the use of thermocouples [135]. Stone et al. [135] demonstrated that for sample temperatures above the Debye temperature accuracies of 10 K can be achieved independent of the sample pressure. Yuan et al. [138] applied neutron resonance spectroscopy to determine the temperature in extreme conditions. They studied the internal temperature of a system undergoing dynamic loading, i.e. the temperature behind an explosive shock. The sample was a layered disk of molybdenum doped with tungsten enriched in ^{182}W. The resonance dip of the 21.1 eV resonance of ^{182}W, resulting from transmission measurements with a ^{6}Li detector in current mode [139], was used as the thermometer.

Doppler broadened resonance profiles are also analysed to study fundamental properties of materials like effective temperatures [140–142] and statistical properties of phonon spectra [22, 23]. Neutron resonance spectroscopy has been applied in Refs. [140, 141] to determine the effective temperature in $YBa_2Cu_3O_7$ and $YBa_2Cu_3O_{6.2}$. Transmission measurements have been performed at the 80-m and 18.5-m flight path station of the ORELA facility using a ^{6}Li glass scintillator, on a $YBa_2Cu_3O_7$ and a $YBa_2Cu_3O_{6.2}$ sample, respectively. The resonance profiles of the 230 eV resonance were studied. For this resonance the Doppler width ($\sim$ 1.5 eV) is much larger than the total width Γ ($\sim$ 0.3 eV) and the width due to the resolution ($\sim$ 0.15 eV). From a resonance shape analysis they derived an effective temperature for Cu in the superconducting compound $YBa_2Cu_3O_7$ of $T_{eff} = 297 \pm 28$ K which is within uncertainties consistent with the value $T_{eff} = 314 \pm 28$ K that was found for Cu metal [140]. The latter is in agreement with the one in Table 1. Similar results were obtained for Cu in the non-superconducting compound $YBa_2Cu_3O_{6.2}$ [141]. Therefore, the authors in Refs. [140, 141] concluded that the mechanism for high-temperature superconductivity in $YBa_2Cu_3O_7$ are not due to anomalous copper vibrations and must not rely on an unusual energy scale for Cu phonons. The effective temperature for Cu in $YBa_2Cu_3O_7$ derived by Mook et al. [140] deviates from the one $T_{eff} = 750$ K measured by Ikeda et al. [143]. The latter was derived from neutron scattering experiments which are far more complicated than transmission experiments. Since the sample contained a substantial amount of oxygen, a bias due to the impact of neutron scattering in oxygen on the observed resonance profile is not excluded, as noted in Ref. [140].

4.6 Neutron resonance imaging

Neutron imaging methodologies and experimental capabilities are well-established for imaging at cold and thermal neutron beams [144–150]. In most cases only contrast figures are obtained, except when energy selective techniques are used to study Bragg-edge profiles, e.g. phase imaging using time-of-flight neutron diffraction [147] or energy selective neutron radiography and tomography [146, 150]. However, imaging applications resulting in a direct spatial dependent element distribution are rather scarce.

On the other hand, the development of position sensitive neutron detectors (PSND) for imaging at cold and thermal neutron beams [151–153] triggered the interest in imaging combined with neutron resonance spectroscopy with the objective to determine spatial dependent elemental compositions [154–157, 159]. As discussed in section 2 two approaches using the resonance structures in the epi-thermal energy region can be applied. A signal can be extracted from the beam, i.e. transmission

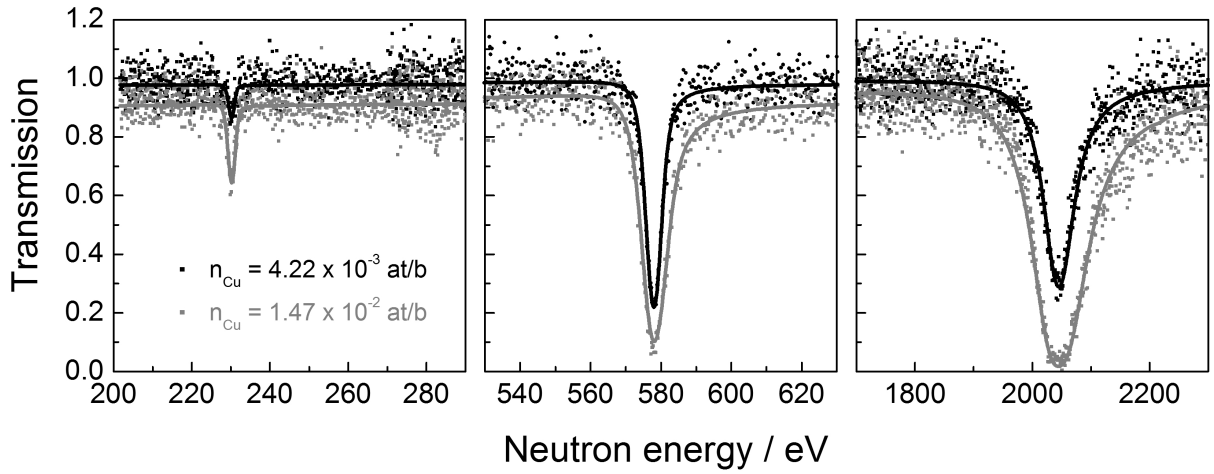

Fig. 43: Results of transmission measurements (symbols) for two disks of natural Cu with areal densities (n_{Cu} = 4.22×10^{-3} at/b and n_{Cu} = 1.47×10^{-2} at/b) together with resonance shape analysis calculation using REFIT (lines).

measurements, or from the radiation (γ-rays) induced by the neutron interaction in the sample. They rely on completely different techniques for imaging or tomography applications. Neutron resonance capture imaging (NRCI) requires time-consuming and cumbersome scanning of the sample at a collimated epi-thermal neutron beam [34,160–162]. The spatial resolution will depend on the collimation of the neutron beam. Neutron resonance transmission imaging (NRTI) is based on measurements with a 2-dimensional position sensitive neutron detector. The whole area of the object is illuminated and a two-dimensional map is produced in one measurement. Hence, NRTI is less time consuming. In addition, the data reduction and analysis procedures are less complicated. The disadvantage is that NRTI is less sensitive to impurities and trace elements compared to NRCI.

Most of the effort in the development of resonance imaging concentrated on the development of NRTI [154–159]. To exploit the resonance structures by transmission measurements a pixelated PSND has been developed by Schooneveld et al. [151]. The PSND is a 10×10 pixelated detector formed by 100 ^{6}Li-glass scintillators ($2 \times 2 \times 9$ mm^3) mounted with a pitch of 2.5 mm. The performance of the PSND for quantitative elemental analysis was assessed at the GELINA facility [5]. Results of measurements for two metal disks of natural Cu with a different areal density are shown in Fig. 43. The areal densities resulting from a resonance shape analysis with REFIT, $n_{Cu} = (4.29 \pm 0.10) \times 10^{-3}$ at/b and $n_{Cu} = (1.49 \pm 0.02) \times 10^{-2}$ at/b, are in very good agreement with the declared values $n_{Cu} = 4.22 \times 10^{-3}$ at/b and n_{Cu} = 1.47×10^{-2} at/b, respectively. It should be noted that the good agreement was only obtained by adopting the resonance parameters of ^{63}Cu and ^{65}Cu reported by Weigmann and Winter [88]. This detector was used to derive elemental sensitive contrast figures from transmission measurements at the INES beam of ISIS. Examples of such contrast figures can be found in Refs. [5, 156]. A similar PSND with comparable performance was used by Sato et al. [153, 154] to produce contrast figures for In and Ag. They also derived the spatial distribution of the temperature from an analysis of resonance profiles.

A PSND with a timing resolution of < 20 ns in the epi-thermal region and 0.5 μs in the thermal region and a spatial resolution of < 100 μm, has been developed by Tremsin et al. [149, 152]. The detector was used to measure spatial dependent transmission Bragg-edge and resonance profiles at the LANSCE [157] and J-PARC facility [159]. The results obtained at J-PARC [159] reveal that for strong absorption and for weak resonances with energies above 4 keV the profiles for Cu were not described. This is probably due to the lack of any correction for background contributions. Correction for background when performing NRTI with a PSND is not evident since there is no collimation of the neutron

Table 9: Composition of a 2.5 cm thick nuclear spent fuel sample (center cut) measured with NRTA by Behrens et al. [95].

Nuclide	Abundance 10^{-5} at/b	Nuclide	Abundance 10^{-5} at/b
^{234}U	1.481 ± 0.060	^{99}Tc	9.94 ± 0.27
^{235}U	37.67 ± 0.85	^{131}Xe	3.382 ± 0.063
^{236}U	15.79 ± 0.42	^{133}Cs	7.63 ± 0.29
^{238}U	4765 ± 27	^{145}Nd	3.096 ± 0.274
		^{152}Sm	0.694 ± 0.013
^{239}Pu	3.74 ± 0.76		
^{240}Pu	26.26 ± 0.60		
^{241}Pu	10.64 ± 0.15		
^{242}Pu	4.94 ± 0.33		
^{241}Am	5.52 ± 0.22		
^{243}Am	0.705 ± 0.058		

beam between the sample and the detector. Therefore, a special procedure to account for the sample dependent background component, as discussed in Ref. [156], is required.

5 Characterisation of melted fuel by neutron resonance densitometry

Neutron Resonance Densitometry (NRD) is being developed as a method to quantify special nuclear material (SNM) in particle-like debris of melted fuel formed in severe nuclear accidents [8, 9]. NRD is based on NRTA and a combination of NRCA with PGA. The quantification of the fissile material will be based on NRTA, while NRCA using a detector with a good γ-ray energy resolution will be applied to determine the amount of impurities. A conceptual design of a NRD facility has been presented by Harada et al. [8]. The facility consists of a transmission station with a flight path length between 5 m and 10 m combined with three beam lines for NRCA/PGA. The latter, with flight path lenghts smaller than 5m, are equipped with well-type $LaBr_3$ scintillators [163], which are used to combine TOF and γ-ray spectroscopic measurements.

The potential of NRTA for the characterisation of such samples has already been demonstrated by Priesmeyer et al. [93] and Behrens et al. [94, 95], as discussed in the previous section. However, the samples analysed in these references were all homogeneous samples. Also the feasibility study of Sterbentz and Chichester [164], which is fully based on Monte Carlo simulations, considers NRTA only for the characterisation of intact fresh and spent fuel assemblies. The analysis of particle like debris will be more complex and challenging [9]. This is mainly due to the specific characteristics of the samples, in particular, the radioactivity, sample temperature, presence of unknown matrix material including strong neutron absorbers and the diversity in shape and size of the particle like debris samples.

Theoretical transmissions as a function of neutron energy through 2.5-cm thick spent fuel samples were used to study systematic effects due to the sample characteristics. The REFIT codes was used for the calculations. The elemental and isotopic composition of the sample, given in Table 9, was based on the work of Behrens et al. [95]. The resonance parameters were taken from JENDL 4.0. The parameters for ^{235,238}U and ^{239}Pu in JENDL 4.0 [165] were adopted from Refs. [166–168]. The transmissions were calculated for an ideal transmission geometry with the sample at 400 K and the detector placed at 10 m from the neutron source. The response of the TOF-spectrometer was represented by a Gaussian distribution of the equivalent distance with a FWHM of 2.5 cm independent of the neutron energy. The

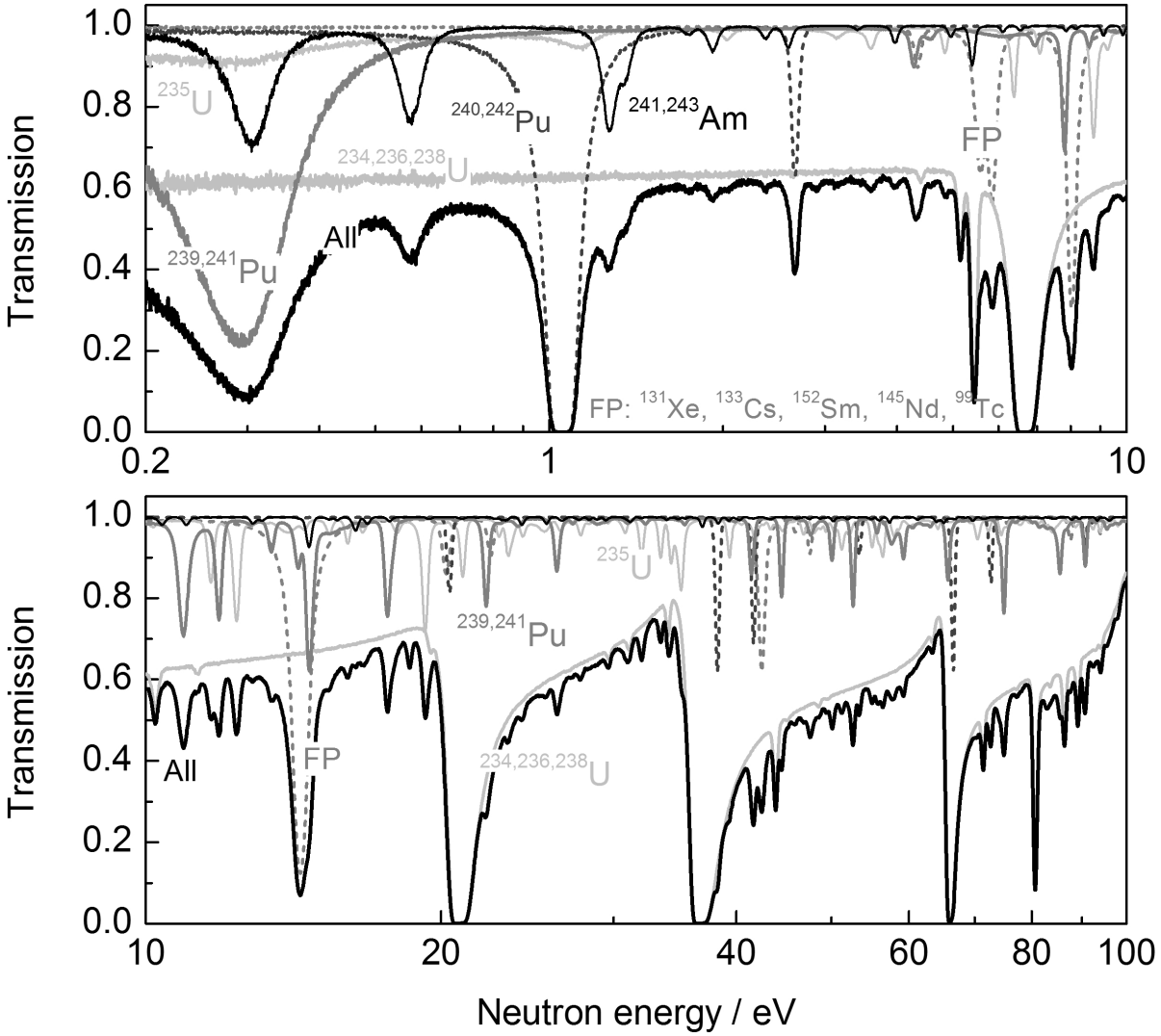

Fig. 44: Simulated transmission through a spent fuel sample at T_{eff} = 400 K resulting from measurements at a 10 m flight path distance.

contribution of the different nuclides present in the sample is shown in Fig. 44 by plotting separately the transmission due to the presence of only fission products (i.e. ^{99}Tc, ^{131}Xe,^{133}Cs,^{145}Nd,^{152}Sm); ^{234,236,238}U; ^{235}U;^{240,242}Pu; ^{239,241}Pu; and ^{241,243}Am. From a RSA of the transmission the areal densities of all these nuclides can be derived. The best accuracy will be obtained when isolated resonances are analysed (e.g. for ^{235}U the resonances at 8.77 eV, 12.43 eV and 19.32 eV), such that the results are not strongly affected by the quality of the parameters of overlapping resonances.

5.1 Temperature

As discussed in section 2 the transmission will be broadened due to the sample temperature. The temperature can be derived from a profile of an isolated resonance with a width that is dominated by the Doppler broadening. Possible candidates to act as a thermometer are the 2.67 eV, 5.16 eV and 5.45 eV resonances of ^{242}Pu, ^{234}U and ^{236}U, respectively. The sensitivity of the transmission to the temperature for these resonances is shown in Fig. 45 by comparing the transmission at T_{eff} = 0 K, 300 K and 400 K. In case the profile is dominated by the response of the TOF-spectrometer a saturated resonance can also be used to assess the effective temperature. This is illustrated by the transmission around the 80.73

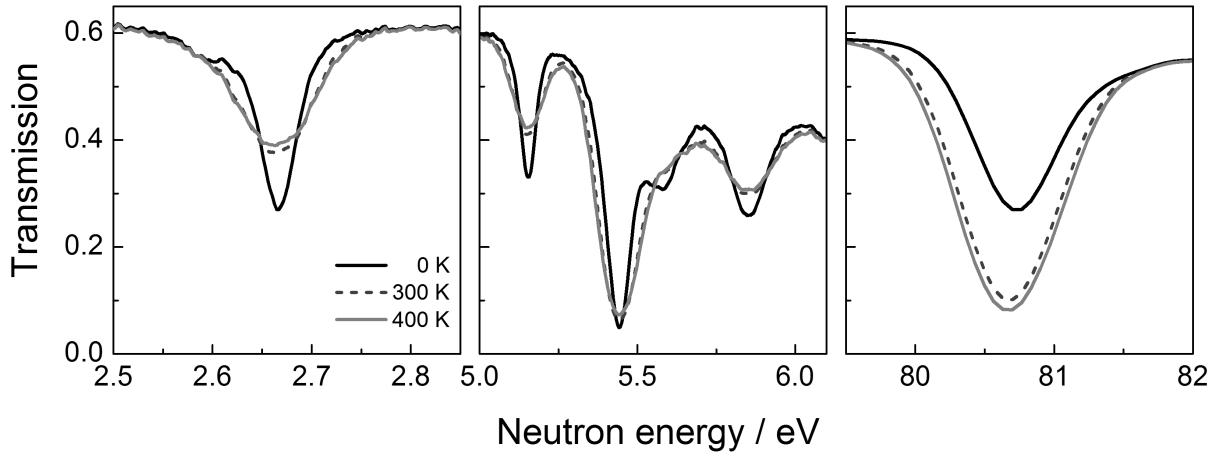

Fig. 45: Simulated transmission through a spent fuel sample at T_{eff} = 0 K, 300 K and 400 K resulting from measurements at a 10 m flight path distance.

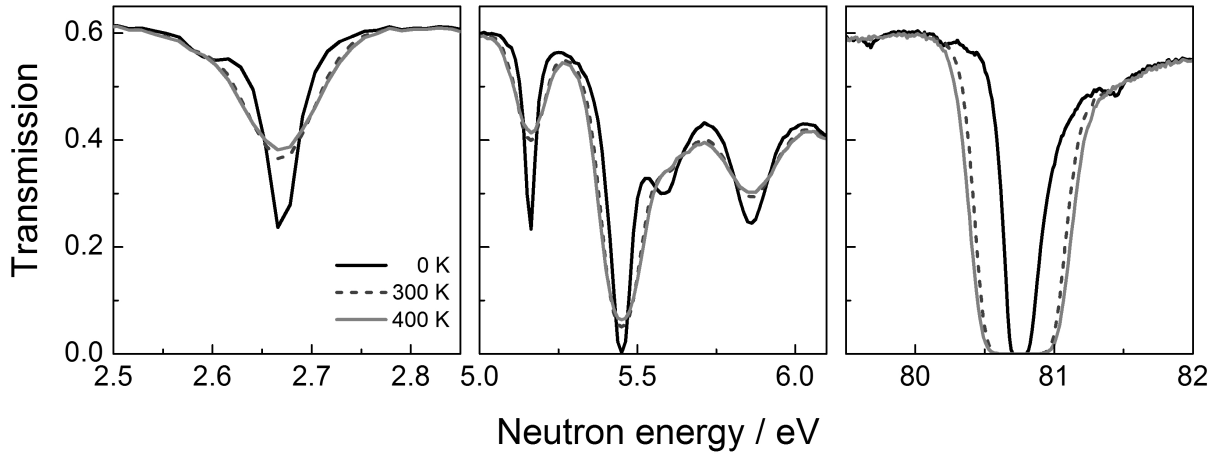

Fig. 46: Simulated transmission through a spent fuel sample at T_{eff} = 0 K, 300 K and 400 K without resolution effects.

eV saturated resonance of ^{238}U at different temperatures in Fig. 45. The unexpected behavior of the profile, i.e. decrease in transmission dip with increasing temperature, is due to the impact of the response function of the TOF-spectrometer. Fig. 46 compares the transmission for different sample temperatures without any additional broadening due to the response of the TOF spectrometer. Evidently, the accuracy of the temperature derived from such a saturated resonance profile will depend on the quality of the response function.

5.2 Matrix material

In contrast to fresh or spent fuel, information about the elemental and isotopic composition of melted fuel formed after a severe nuclear accident is rather scarce and cannot be predicted. It is expected that the melted fuel will contain water, boron, concrete and structural materials like Co, Fe, Cr and Ni. The presence of these elements will complicate the analysis. Unfortunately, for these light elements no resonances are present below 100 eV to detect and quantify them (see Table 10). The strong influence of ^{10}B on the transmission is shown in Fig. 47. The transmission spectrum has been calculated using the areal densities given in Table 9 and different additional amounts of ^{10}B with the sample at T_{eff} = 400 K. The transmission spectrum has been slightly randomized assuming an uncertainty of 0.01 for a transmission of one and a minimum uncertainty of 0.001. Two methods can be applied to account for the

Table 10: Energies of prominent prompt γ-rays and 1^{st} neutron resonances for light and medium elements.

Nucleus	Reaction	Energy of prominent prompt γ-ray	Energy of 1^{st} neutron resonance
^{1}H	^{1}H (n,γ) ^{2}H	2223 keV	–
^{10}B	^{10}H (n,$\alpha\gamma$) ^{7}Li	478 keV	170 keV
^{27}Al	^{27}Al (n,γ) ^{28}Al	3034 keV, 7724 keV	5.9 keV
^{28}Si	^{28}Si (n,γ) ^{29}Si	3539 keV, 4934 keV	31.7 keV
^{53}cr	^{53}Cr (n,γ) ^{54}Cr	835 keV, 8885 keV	4.2 keV
^{56}Fe	^{56}Fe (n,γ) ^{57}Fe	7631 keV, 7646 keV	1.1 keV
^{59}Co	^{59}Co (n,γ) ^{60}Co	230 keV, 6877 keV	0.132 keV
^{58}Ni	^{58}Ni (n,γ) ^{59}Ni	465 keV, 8999 keV	6.9 keV

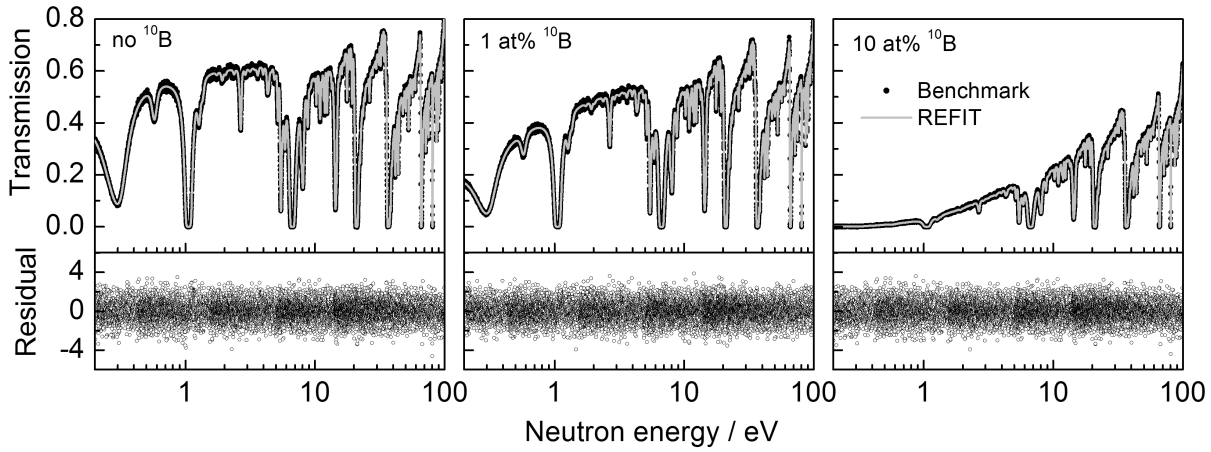

Fig. 47: Transmission as a function of neutron energy through a spent fuel sample with different relative amounts of ^{10}B. The data are compared with the results of a resonance shape analysis with REFIT. In the calculations of the transmission a dummy element is included to account for the presence of matrix materials.

contribution of these matrix materials to the observed transmission. The first is based on a direct analysis of the transmission and the second on additional measurements with a $LaBr_3$ detector.

The influence of matrix materials can be taken into account by lumping their contribution to the transmission using a single total cross section $\sigma_{tot,X}$ of a dummy element X. The energy dependence of this cross section consists of a constant and a $1/v$ contribution, such that:

$$n_X \sigma_{tot,X} = a_X + \frac{b_X}{v}. \tag{40}$$

The parameters a_X and b_X are adjusted in a least squares fit to the experimental data. This procedure has been tested on the transmissions of Fig. 47. REFIT was used to fit the areal densities, the sample temperature and the parameters a_X and b_X. The areal densities of ^{235,238}U and ^{239,241}Pu derived from the fit are compared in Table 11 with the values used to simulate the transmission data. Except for ^{241}Pu there is a very good agreement. This confirms that the use of a dummy element with a cross section given by Eq. (40) is a valuable method to account for the presence of matrix elements. The problem to detect and quantify ^{241}Pu is general and is not related to the procedure to account for the presence of

Table 11: Results of a least squares fit with REFIT to derive the areal densities of ^{235}U, ^{238}U, ^{239}Pu and ^{241}Pu from the transmissions in Fig. 47. The ratio of the fitted areal density and the value used to produce the transmission is reported.

Nucleus	Reference	Fit result / Reference		
	10^{-5} at/b	no ^{10}B	1 at% ^{10}B	10 at% ^{10}B
^{235}U	37.67	0.998 ± 0.004	0.996 ± 0.004	0.998 ± 0.006
^{238}U	4765	1.001 ± 0.001	1.000 ± 0.001	1.001 ± 0.001
^{239}Pu	26.26	0.997 ± 0.002	0.997 ± 0.002	0.993 ± 0.005
^{241}Pu	4.94	1.062 ± 0.011	1.048 ± 0.012	1.060 ± 0.021

^{10}B. The strongest contribution to the transmission due to ^{241}Pu, results from the resonance at 0.258 eV. Unfortunately, in this region the transmission is strongly influenced by ^{239}Pu.

A second method relies on NRCA combined with a spectroscopic measurement of prompt γ-rays. Most of the matrix materials are light or medium heavy elements. They emit high energetic prompt γ-rays with a significant intensity after a neutron capture reaction. In Table 10 the energies of prominent prompt γ-rays emitted after neutron absorption are listed. Except for ^{10}B all of the matrix elements emit a γ-ray with an energy that is higher on than 2 MeV. Hence, these γ-rays do not suffer from a Compton background due to the detection of the 661 keV γ-ray from the decay of ^{137}Cs. On the other hand, the detection of the 478 keV γ-ray following the ^{10}B(n,$\alpha_1\gamma$) reaction will be hampered by the presence of the Compton edge at 476 corresponding to a 661 keV γ-ray. To overcome this difficulty, a $LaBr_3$ γ-ray spectrometer with a favourable peak-to Compton ratio was designed by JAEA [163]. Since a $LaBr_3$ detector has a good time and energy resolution, it can be used for γ-ray spectroscopic TOF measurements. It was shown that the spectrometer is able to determine the contribution of the 418 keV γ-rays even under a high background caused by the presence of ^{137}Cs [8].

5.3 Sample heterogeneity

One of the main difficulties for a correct interpretation of the result of a transmission measurement is to account for any heterogeneity of the sample. The attenuation of a neutron flux in a heterogeneous sample can differ significantly from the attenuation in a homogenized medium. This occurs predominantly if the length of the microscopic structure of the heterogeneity is larger than the mean free path of the neutron. In case of heterogeneous samples, the expected transmission can be calculated as a weighted average:

$$T_{het} = \prod_k \int_0^\infty dn_k \, p(n_k) e^{-n_k \overline{\sigma}_{tot,k}} \, , \tag{41}$$

where the weights are the areal density distributions $p(n_k)$ of the different nuclides present in the sample. Only when $\sum_k n_k \overline{\sigma}_{tot,k}$ is very small, the transmission is a direct function of the average areal densities $\overline{n}_k$:

$$T_{het} \approx T_{hom} \approx 1 - \sum_k \overline{n}_k \overline{\sigma}_{tot,k} \, , \tag{42}$$

with $\overline{n}_k = \int_0^\infty dn_k \; p(n_k) n_k$ the average areal density, which can be derived from a measurement of the mass, area and average elemental, isotopic and chemical composition. Under these conditions the transmission can be considered as a homogeneous limit.

Bias effects will be introduced when the heterogeneity of the sample is not taken into account in the analysis in case $\sum_k n_k \overline{\sigma}_{tot,k}$ is not very small. The impact of a sample heterogeneity on results of

transmission measurements has been demonstrated by Kopecky et al. [170]. They measured the neutron transmission through a sample consisting of PuO_2 powder mixed with carbon powder and canned in a copper container. The measurements were carried out to deduce the resonance parameters of the 2.65 eV resonance of ^{242}Pu. The Pu in the PuO_2 powder was enriched to 99.93 wt% in ^{242}Pu. It was demonstrated that the deduced resonance parameters were significantly biased when the heterogeneity of the powder sample was not taken into account [5].

Since the calculation of the transmission of particles like neutrons through stochastic, heterogeneous media is important in different fields such as radiation protection [171, 172], nuclear engineering [173, 174], climatology [175–177] or astrophysics [178, 179], various models have been developed over the years to account for the heterogeneity.

Kopecky et al. [170] developed a model directly based on Eq. (41). Since the model relies on a macroscopic variation of the material and not on the microscopic structure of the heterogeneous sample, it can be considered as a macroscopic approximation. The transmission T_{MD} of neutrons through the sample is given by:

$$T_{MD} = \left[\int e^{-\sum\limits_k n'_k x \overline{\sigma}_{tot,k}} p'(x) dx \right] (1 - f_h) + f_h \ , \tag{43}$$

where $p'(x)$ is a probability distribution that is centered at one. The variable x reflects the variation of the areal density due to the inhomogeneity of the sample. The hole fraction f_h describes the probability that the neutrons pass the sample without intersecting any material. The average effective areal density n'_k is related to the average areal density $\overline{n}_k$, by $n'_k = \overline{n}_k/(1 - f_h)$. For a normal distribution of the areal density, the probability distribution $p'(x)$ is given by:

$$p'(x) = p_N(x) = \frac{1}{\sqrt{2\pi s_N^2}} \exp\left(-\frac{(x-1)^2}{2s_N^2} \right) \ , \tag{44}$$

with the average centered at one and width parameter s_N^2. It is assumed that all nuclides of interest form one common phase such that s_N^2 is independent of k. In case of large values for s_N, the distribution is truncated at $x \leq 0$ and $x \geq 2$ and renormalized, to prevent unphysical negative values while maintaining one as an average. Assuming a log-normal distribution of x, the distribution $p'(x)$ becomes:

$$p'(x) = p_{LN}(x) = \frac{1}{x\sqrt{2\pi s^2}} \exp\left(-\frac{\left(\ln(x) + s^2/2\right)^2}{2s^2} \right) \ , \tag{45}$$

with as average value one and a width parameter s^2 independent of k. In this case, there is no need for truncation is case of large values for s^2.

Doub [171] developed a model by introducing a so-called particle self-shielding factor f. The transmission of a monoenergetic beam through a heterogeneous sample T_{het} is then [171]:

$$T_{het} = e^{-f \sum\limits_k n_k \overline{\sigma}_{tot,k}} \ , \tag{46}$$

where f acts as a correction factor of the cross section. When the number of sample particles passed by the neutron can be described by a binomial distribution and when all particles are spherical with the same radius r, the factor f is given by [171]:

$$f = \frac{1}{\frac{2}{3} y \frac{p}{g}} \ln\left[\frac{1}{1 - \frac{p}{g} - (1 - \bar{t})} \right] \ , \tag{47}$$

with $y = 2r\Sigma$ and $\Sigma = \frac{1}{p} \sum\limits_k n_k \overline{\sigma}_{tot,k}$. The latter is the total Doppler broadened macroscopic cross section of the material and p is the volume fraction that is occupied by the sample particles. For a closely

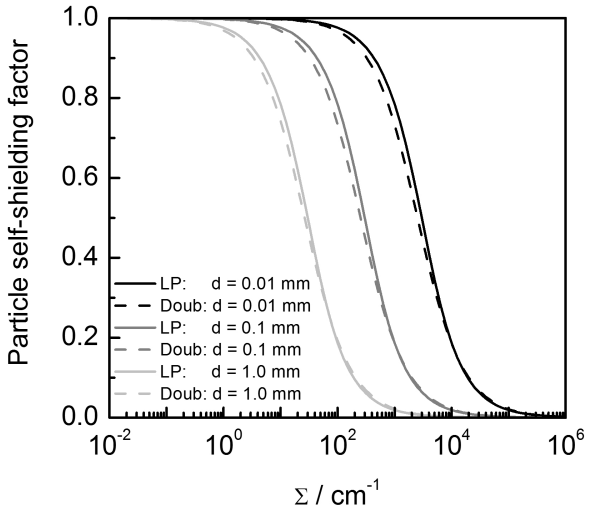

Fig. 48: Particle self-shielding factor calculated using Doub's model and the LP model as function of the total macroscopic cross section Σ of the particle material. Results are given for a 1 cm thick sample consisting of particles with diameters $d = 0.01$, 0.1 and 1 mm.

packed powder sample the parameter g can be approximated by 0.74. The average transmission through a single particle $\bar{t}$ is given by

$$\bar{t} = \frac{2}{y^2}\left[1 - (1+y)e^{-y}\right] \ . \tag{48}$$

Doub extended the model to polydisperse spheres using a volume averaged self-shielding factor $\bar{f}$ that is defined by

$$\bar{f} = \sum_j \frac{p_j}{p} \ , \tag{49}$$

where f_j and p_j are the self-shielding factor and volume fraction of a sphere with a radius r_j. Doub compared the model with the transmission of low energy neutrons through mixtures containing boron-carbite spheres [171].

Levermore et al. [180] developed a model for the neutron transport through a stationary Markovian statistical binary mixture. This model is often referred to as the LP-model. Within this model, the line segments in a particular component along a trajectory of a particle have an exponentially decaying chord length probability distribution. The transmission T_{LP} of a monoenergetic neutron beam through a sample of thickness t, consisting of a binary mixture, is given by [180]:

$$T_{LP} = \left[\frac{r_+ - \tilde{\Sigma}}{r_+ - r_-}e^{-r_+ t} + \frac{\tilde{\Sigma} - r_-}{r_+ - r_-}e^{-r_- t}\right] \ . \tag{50}$$

The decay constants $r_\pm$ are given by:

$$2r_\pm = \left[\langle\Sigma\rangle + \tilde{\Sigma}\right] \pm \left[(\langle\Sigma\rangle - \tilde{\Sigma})^2 + 4\beta\right]^{1/2} \tag{51}$$

with

$$\langle\Sigma\rangle = p_\alpha\Sigma_t^\alpha + p_\beta\Sigma_t^\beta \tag{52}$$

$$\tilde{\Sigma} = p_\beta\Sigma_t^\alpha + p_\alpha\Sigma_t^\beta + \lambda_\alpha^{-1} + \lambda_\beta^{-1} \tag{53}$$

$$\beta = (\Sigma_t^\alpha - \Sigma_t^\beta)^2 p_\alpha p_\beta. \tag{54}$$

The two components of the binary mixture are denoted by α and β. The total, Doppler broadened, macroscopic cross section and corresponding mean chord length of component i are denoted by Σ_t^i and λ_i, respectively. The volume fraction p_i is given by $p_i = \lambda_i/(\lambda_\alpha + \lambda_\beta)$. Using Eq. (46) and Eq. (50) the particle self-shielding factor based on the LP-model can be simply calculated by:

$$f_{LP} = \frac{-\ln(T_{LP})}{\sum\limits_k n_k \overline{\sigma}_{tot,k}} \,. \tag{55}$$

Fig. 48 shows the particle self-shielding factor based on the model of Doub (Eq. 47) and on the LP model (Eq. 55) as function of the total macroscopic cross section of the material for a 1-cm thick sample consisting of particles with diameters of 0.01, 0.1 and 1 mm. It was assumed that the cross section of the matrix is negligible. Both models give the same trend for the particle self-shielding factor. For small macroscopic cross sections the factor is one and the sample can be considered as being homogeneous. The factor drops rapidly with increasing macroscopic cross section. The macroscopic cross section where the particle self-shielding factor starts to drop depends strongly on the particle size.

Transmission through heteregoneous powder samples were calculated by Monte Carlo simulations to study the performance of the analytical models for NRTA on particle like debris samples [181]. To validate the models using the numerical benchmarks, they have been implemented in the REFIT code [181]. Since REFIT uses numerical derivatives for the least squares adjustment, it is rather straightforward to include the model parameters as additional adjustable parameters.

A heterogeneous sample was generated using the discrete element modeling code LAMMPS Molecular Dynamics Simulator from Sandia National Laboratory [182] by simulating the filling process of a sample. The full trajectory and interaction between different powder particles, i.e. normal and tangential forces between particles, were simulated. The sample was assumed to be 1 cm thick and 4 cm wide with cyclic lateral boundaries. Two different kinds of spherical particles were assumed: heavy metal oxide (HMO) particles consisting of a mixture of ^{235}U, ^{238}U, ^{239}Pu and ^{240}Pu - oxide and matrix material particles. The elemental composition and the isotopic vector of the actinides was based on Table 9. A density of 10.4 g/cm^3 was used. The diameter of the two kinds of particles was log-normal distributed with an average diameter of $\bar{d} = 1$ mm and a variance of $\sigma^2 = 0.25$ mm^2. A total of 4332 HMO and 4282 matrix particles were dropped into the sample. Fig. 49 shows the obtained packing bed which had a height of about 5 cm. A ray tracing method was applied to determine the cumulative thickness distribution of HMO particles and to calculate the transmission of neutrons through the stochastic mixture. Four million, parallel rays impinging on the wide side of the sample and transversing the particle mixture were simulated. Only the part of the packing bed which was settled and fully filled with particles was used. The obtained volume fraction of the HMO particles within the packing bed was deduced to be 40%. This results into an average areal density of 7.34×10^{-2} at/b. The probability that a ray does not intersects with any HMO particle was determined to be 2.6%. Finally, the result of a transmission measurement was simulated for measurements at a 10 m station with TOF channel bin widths of 512 and 1024 ns above and below 7.2 eV, respectively. All cross sections were Doppler broadened to 300 K. Resolution effects were not considered. The spectrum was slightly randomized around the average assuming an uncertainty due to counting statistics of about 0.5% for transmission equals one. Fig. 50 shows the generated transmission in the energy region 0.1 to 40 eV containing strong resonance of ^{238}U (6.67 eV 20.84 eV, 36.68 eV), ^{239}Pu (0.295 eV) and ^{240}Pu (1.056 eV).

The areal densities of ^{235}U, ^{238}U, ^{239}Pu and ^{240}Pu, together with all model parameters and a normalization constant, were adjusted in a fit to the benchmark transmission. The areal density of oxygen was not fitted. Its constant cross section in the considered energy interval leads only to a constant decrease of the transmission which was taken into account by adjusting the normalization. The same nuclear model parameters as those for generating the benchmark case were used. Fig. 50 shows the result of a fit using the LP-model and assuming a homogeneous sample. The residuals clearly indicate the significant improvement in calculating the transmission through a stochastic sample when a dedicated model is

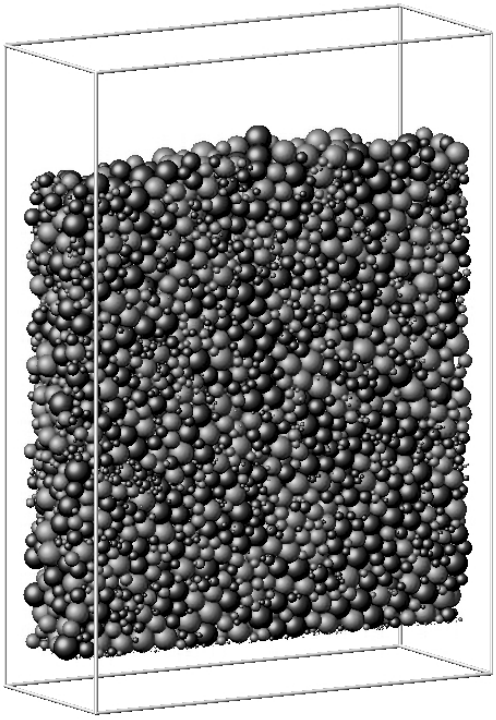

Fig. 49: Stochastic mixture of heavy metal oxide (dark gray) and matrix particles (light gray) simulated using the discrete element modeling code LAMMPS Molecular Dynamics Simulator.

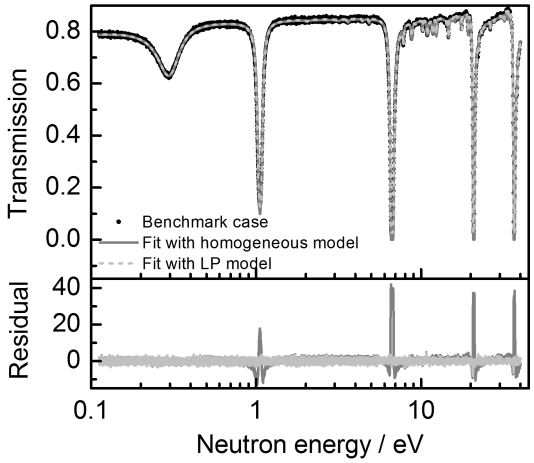

Fig. 50: Calculated benchmark transmission together with the result of a least squares adjustment with REFIT assuming a homogeneous mixture and a heterogeneous mixture based on the LP model. The residuals of the fits are shown in the lower part.

used to account for the heterogeneous character of the sample. While the homogeneous model strongly underestimates the resonance dips, with a residual largely exceeding 30, application of a heterogeneous models leads to flat residuals. Table 12 summarizes the result of the fit. The benchmark areal densities are given together with the ratio of the fitted ones and the benchmark values. The ratios are given for the densities resulting from a fit using the homogeneous assumption, the LP model and the model of Kopecky et al. [170] supposing both a normal and log-normal distribution. Assuming a homogeneous sample leads to a strong underestimation of the ^{238}U, ^{239}Pu and ^{240}Pu content of up to 23% and to an overestimation of the ^{235}U content by more than 9%. The maximum bias in case of the the macroscopic model (Eq. (43)) combined with a log-normal distribution (Eq. (45)) and a normal distribution (Eq. (44)) is 1.3% and 3.2%, respectively. In case of the LP model the maximum bias is 1.6%. Since the LP model is based on a Markovian geometry, its performance increases with non-regular shapes instead of spheres. The performance of the LP-model confirms the preliminary results obtained in Ref. [184].

6 Experimental validation of NRD for the characterisation of melted fuel

The discussion in the previous section suggests that heterogeneous samples, even in the presence of strong absorbing matrix materials, can be characterized by NRTA. However, this conclusion is mainly based on an analysis of simulated data. In this section the performance of NRTA for such samples is verified based on results of experiments carried out at GELINA.

Table 12: Ratio of the fitted areal density and the benchmark value. The fitted results were derived by assuming a homogeneous sample and by using models accounting for the heterogeneity.

	^{235}U	^{238}U	^{239}Pu	^{240}Pu
Reference areal density / (at/b)	7.677×10^{-5}	9.711×10^{-3}	5.351×10^{-5}	2.168×10^{-5}
Ratio of the fitted and benchmark areal density				
Homogeneous sample	1.094 ± 0.009	0.802 ± 0.001	0.912 ± 0.001	0.763 ± 0.001
Log-normal thickness distribution	1.000 ± 0.008	1.013 ± 0.001	1.011 ± 0.001	1.010 ± 0.001
Normal thickness distribution	1.002 ± 0.008	0.985 ± 0.001	0.982 ± 0.001	0.968 ± 0.001
LP	0.993 ± 0.008	0.997 ± 0.002	0.989 ± 0.002	0.984 ± 0.002

6.1 Characterisation of heterogeneous samples

An experimental validation of the LP-model presented in Sec. 5 was reported by Becker et al. [51]. They analyzed a sample containing a mixture of sulfur and tungsten powder by neutron transmission measurements at a 25 m station of GELINA. Neutrons were detected by a 12.7 mm thick and 101.6 mm diameter NE912 Li-glass scintillator enriched to 95% in ^{6}Li. The sample was made by mixing 14.36 ± 0.10 g tungsten powder,with nominal grain sizes of 50 – 250 μm, and 3.480 ± 0.025 g sulfur powder, with a grain size of 44 μm. The powder mixture was filled into an aluminum canning. The data were analyzed in the energy region from 3 eV to 200 eV. Fig. 51 shows a comparison of the measured transmission and the results of a fit assuming a homogeneous sample and applying the LP-model. The lower part of Fig. 51 shows the residuals. The areal density of tungsten and the normalization factor were fitted to the experimental transmission. In case of the LP-model, the model parameters $\lambda_\alpha = (54 \pm 10)$ μm and$p_\alpha = 0.26 \pm 0.03$ were also fitted. The limitations of the homogeneous assumption are clearly visible due to the pronounced fluctuating residual in the vicinity of strong resonances. In case of the LP-model a flat residual was obtained. The difference in χ^2 per degree of freedom, i.e. 2.5 for the homogeneous model and 1 for the LP-model, confirms the substantial, difference in the quality of the fit. The particle self-shielding factor was estimated using directly the experimental transmission spectrum by calculating $f_{exp.} = \ln(T_{exp.})/\ln(T_{hom})$, where T_{hom} is the transmission through a homogeneous sample calculated by REFIT. Fig. 52 shows the experimental particle self-shielding factor as a function of $-\ln(T_{hom})$ based on all data points between 3 eV and 200 eV and as grouped values with 20 values per decade. The particle self-shielding calculated based on the LP-model (Eq. (55)) is shown as well. The good agreement between the experimental and calculated data confirm the good performance of this model.

Unfortunately, a void was formed at the top of the sample. Therefore, the areal density of tungsten could not be accurately derived due to the inhomogeneous filling. An average areal density $n_W = (1.036 \pm 0.026) \times 10^{-3}$ at/b was derived by fitting only weak resonances, for which the self-shielding can be neglected and the homogeneous approximation is valid. This result was used for a quantitative validation of values that were derived from a fit to data that included strong resonances with large particle self-shielding factors. Since the values are derived from a fit with the same resonance parameters, the quality of the nuclear data does not affect such a comparison. Supposing a homogeneous sample, the areal density $n_W = (0.939 \pm 0.001) \times 10^{-3}$ at/b derived from the fit of the strong resonances is underestimated by almost 10%. On the other hand the value $n_W = (1.058 \pm 0.003) \times 10^{-3}$ at/b resulting from a fit with the LP-model is in very good agreement with the one derived from weak resonances. This agreement does not provide a direct validation of the accuracy that can be reached. However, together with the improved quality of the fit shown in Fig. 51, it provides an experimental evidence that the LP-model is well suited to account for the heterogeneous character of the powder sample.

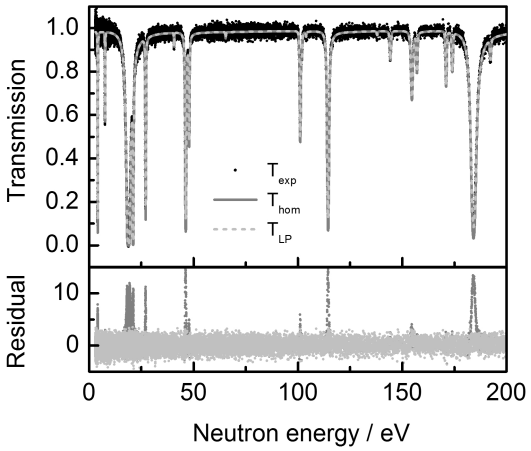

Fig. 51: Experimental transmission $T_{exp.}$ of a tungsten powder sample as a function of neutron energy. The experimental data are compared with the fitted transmission based on a homogeneous sample assumption (T_{hom}) and on the LP-model (T_{LP}). The areal density was adjusted in a fit to the data in the energy region between 3 eV and 200 eV.

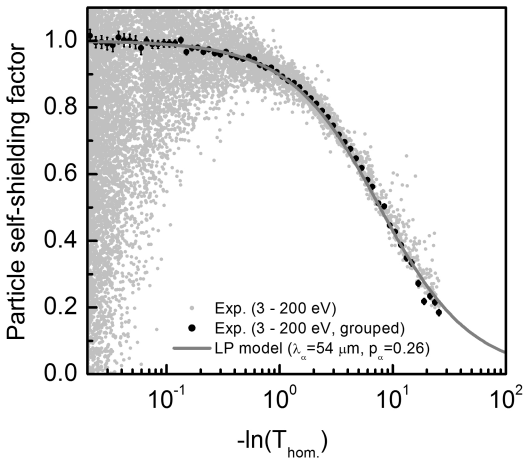

Fig. 52: Experimental and calculated particle self-shielding factor of a tungsten powder sample as a function of $\ln(T_{hom})$. The theoretical particle self-shielding factor is based on the LP model with the model parameters $\lambda_\alpha = 54$ μm and $p_\alpha = 0.26$ (see text).

6.2 Characterisation of a U_3O_8 reference material

A full quantitative validation of absolute NRTA results is obtained from measurements with a U_3O_8 reference sample, with reference CBNM 446 [183], which was enriched to 4.514 at% in ^{235}U. The areal density of ^{235}U and ^{238}U and the corresponding ^{235}U/^{238}U atomic ratio was determined by an analysis of transmission data obtained at a 25-m transmission station of GELINA. The neutron beam was collimated to a diameter of 3.5 cm at the sample position. The sample, which was originally produced as reference material for γ-ray spectroscopy as part of the EU nuclear reference material 171 set [183], is definitely not ideal for transmission measurements. The significant EPOXY content of the ultrasonic identifier, which is placed in the plug of the sample container, led to a strong attenuation of the incident neutron beam, i.e. to an extreme low transmission baseline of about 0.0075. On the other hand, it provides an ideal basis for a validation of the procedure proposed in Sec. 5 to account for the presence of matrix materials which cannot be identified and quantified by resonances.

The dead time corrected sample-in and sample-out TOF-spectra together with the background contributions are shown in Fig. 53. The sample-out measurement was done using a dummy aluminum canning without ultrasonic identifier. The experimental transmission and the result of a RSA with REFIT are compared in Fig. 54. Both Fig. 53 and Fig. 54 illustrate the strong attenuation of the neutron beam due to the EPOXY matrix. Nevertheless, transmission dips due to ^{235}U and ^{238}U could be clearly resolved as indicated in Fig. 54. To account for the contribution of the matrix, a dummy element with a cross section given by Eq. (40) was included. In addition to the areal densities of ^{235}U and ^{238}U, the model parameters a_X and b_X of the dummy element as well as the effective temperature were adjusted in a fit to the experimental data in the 2.5 eV – 40 eV energy region. The resonance parameters were taken from the JENDL 4.0 library. The fitted parameters are reported in Table 13. The quoted uncertainties are only due to a propagation of counting statistics uncertainties. The areal densities are compared with the reference values which were deduced from the the sample area, the U_3O_8 mass, the relative amount of U and the uranium isotopic composition reported in Ref. [183]. The results from a NRTA analysis are within the quoted uncertainties, which only account for the uncorrelated uncertainties due to counting statistics, in agreement with the reference values. The resulting isotopic ratio ^{235}U/^{238}U = 0.0475 ± 0.0008 is in

Table 13: Areal densities of ^{235}U and ^{238}U, model parameters a_X and b_X and effective temperature T_{eff} resulting from a fit to the experimental transmission through the reference sample CBNM 446 of the EU nuclear reference material 171 [183]. The areal densities are compared to the reference values which were deduced from the the sample area, the U_3O_8 mass, the relative amount of U and the uranium isotopic composition reported in Ref. [183].

Parameter	NRTA	Reference
Areal densities		
^{235}U	$(5.063 \pm 0.09) \times 10^{-4}$ at/b	$(5.0326 \pm 0.0080) \times 10^{-4}$ at/b
^{238}U	$(1.062 \pm 0.01) \times 10^{-2}$ at/b	$(1.0628 \pm 0.0015) \times 10^{-2}$ at/b
Additional fit parameters		
a_X	4.679 ± 0.004 eV$^{1/2}$	
b_X	$(7.3 \pm 1.3) \times 10^{-2}$	
T_{eff}	337 ± 15 K	

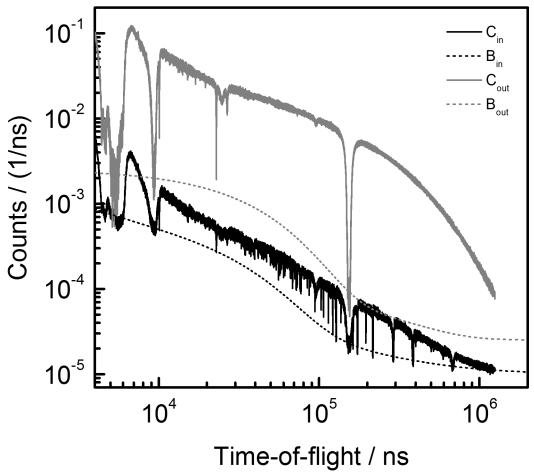

Fig. 53: TOF-spectra taken with a Li-glass detector resulting from transmission measurements at a 25 m station of GELINA of the reference sample CBNM 446 (C_{in}) and of an aluminum dummy sample (C_{out}). The TOF-spectra are shown together with the corresponding total backgrounds B_{in} and B_{out}.

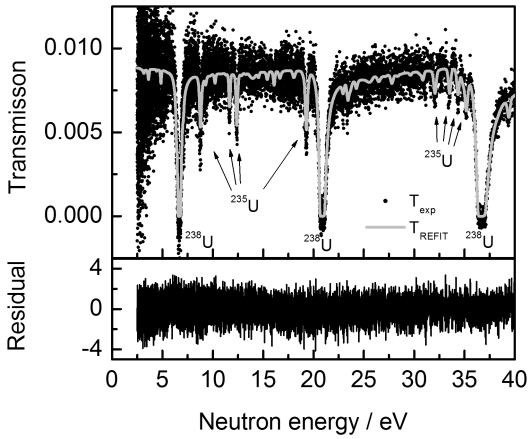

Fig. 54: Experimental transmission through the reference sample CBNM 446 together with the result of a RSA with REFIT. The residual of the fit is shown in the lower part of the figure.

very good agreement with the certified value 0.04729 ± 0.000003. This is also illustrated in Fig. 55. In addition, the fitted effective temperature T_{eff} = 337 ± 15 K is fully consistent with the Debye temperatures for a uranium oxide powder reported by Sanati et al [185]. The Debye temperature of UO_2 in Ref. [185] ranges from 390 K to 425 K, which corresponds to an effective temperature between 316 K and 321 K.

The areal densities of ^{235}U and ^{238}U were obtained with a counting statistics uncertainty of 1.6% and 0.6%, respectively. These values resulted from a 30-h measurement at a 25 m station with an effective sample diameter of 3.5 cm using an electron beam with an average energy of 100 MeV and 40 μA. A similar counting statistics uncertainty can be obtained in about 1800 s at a 10 m station using samples with a 30-cm diameter and a 1kW electron beam. This confirms the results of preliminary calculations presented by Harada et al. [8]. These authors performed calculations for a 1-cm thick and 30-mm diame-

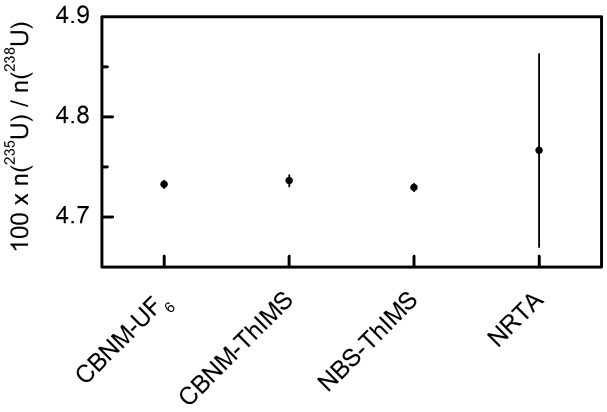

Fig. 55: Relative amount (^{235}U)/^{238}U) of the reference sample CBNM 446 measured with NRTA. The result is compared with measurements by UF_6 mass spectroscopy (UF_6) and thermal ionization mass spectroscopy (ThIMS) performed at the EC-JRC-IRMM (former Central Bureau for Nuclear Measurements (CBNM)) and at NIST (former National Bureau of Standards (NBS)). These data were used for the certification of the reference standard [183].

ter spent fuel sample with the composition defined in Table 9 with an additional amount of 2.5 wt% ^{10}B and 9 wt% Fe as matrix material. The calculations were done for a neutron source with an intensity of 10^{12} s^{-1}. As shown in Ref. [169], such an intensity can be produced by a 1 kW electron beam with a kinetic energy of $\sim$ 40 MeV, a current of $\sim$ 25 μA, an operating frequency of 250 Hz and a pulse width of 400 ns .

7 Nuclear data

A full methodological approach of NRTA and NRCA based on a resonance shape analysis, requires a good description of the measurement process and relies on accurate nuclear data. In this section bias effects and uncertainties due to nuclear data are investigated. Unfortunately covariance information in the recommended data libraries is rather scarce. Most of the covariance data for resonance parameters can be found in ENDF/B-VII.1 and JENDL 4.0.

The quality of resonance parameters recommended in evaluated data libraries and compilations was assessed by a transmission measurement on a tungsten sample. The sample consisted of a 1-mm thick homogeneous metal disc made out of natural tungsten with an areal density of $(6.389 \pm 0.001) \times 10^{-4}$ at/b. The areal density was derived from the weight (118.20 ± 0.001) g and the area (6060.55 ± 0.001) mm^2. The latter was determined by an optical surface inspection with a microscopic based measurement system from Mitutoyo. The measurements were performed at a 50-m transmission station of GELINA using a NE905 Li-glass scintillator (152.4 mm diameter and 6.35 mm thick) as neutron detector. The resonance shape analysis code REFIT was used to derive the areal density from a fit to the experimental transmission in the region of the 46.26 eV and 47.80 eV resonance of ^{183}W. Fig. 56 compares the experimental transmission with the fitted transmission using the JEFF-3.2 parameters [186]. The fit was repeated using resonance parameters recommended in independent nuclear data libraries and compilations. The results are summarized in Table 14, where the ratio of the fitted areal density of ^{183}W and the reference value is reported in the last column. In case covariance data of the resonance parameters are given a conventional uncertainty propagation (Eq. (33)) was carried out to derive the corresponding uncertainty on the areal density. In case that covariance data are not given, the stated uncertainty is only due to a propagation of the counting statistics uncertainty. Note that the resonance parameters of ENDF/B-VII.1 and JENDl 4.0 are based on JENDL-3.3. In ENDF/B-VII.1 covariance data have been added by Trkov et al. [188]. The results in Table 14 reveal large variations with a bias

Table 14: Radiative width Γ_γ and neutron width Γ_n of the 46.26 eV resonance (1) and the 47.80 eV resonance (2) of ^{183}W of different libraries or publications and the ratio of the fitted areal densities and the reference value (9.145×10^{-4} at/b). The latter was obtained from the sample mass, the sample area and the natural isotopic abundances.

		$\Gamma_n^{(1)}$ meV	$\Gamma_\gamma^{(1)}$ meV	$\Gamma_n^{(2)}$ meV	$\Gamma_\gamma^{(2)}$ meV	Fitted areal densities as ratio to reference $\times 100$
JEFF-3.2 [186]		163.4	75.3	120.8	61.5	100.2 ± 0.5
ENDF/B-VI.8 [187]		154	69	115	78	109.7 ± 0.5
JENDL-3.3 [190]		154	46	119	81	111.3 ± 0.5
ENDF/B-VII.1 [191]		154 ±0.8	46 ±2.1	119 ± 1.2	81 ± 5.1	111.3 ± 1.1
Landolt-Börnstein I/16C [192]	2004	157.2 ±0.5	71.5 ±0.2	115.8 ± 0.8	72.9 ± 0.5	106.8 ± 0.5
Landolt-Börnstein I/26A	2014	163.8 ±0.8	63.0 ±0.1	122.6 ± 1.1	59.8 ± 0.2	102.6 ± 0.8
Mughabghab and Garber [193]	1973	140 ±4	69 ±8	115 ±10	78 ±10	121.3 ± 2.2
Mughabghab [194]	1984	140 ±4	77 ±8	108 ±10	78 ±10	119.8 ± 3.4
Mughabghab [195]	2006	162 ±2	77 ±8	122 ± 2	78 ±10	99.2 ± 1.4
Lynn et al. [23]	2002	164 ±1	72	126 ± 2	72	98.3 ± 1.0

of up to 20%. However, from Table 14 one can also conclude that using the latest experimental data and the parameters recommended in JEFF-3.2 there is a very good agreement between the areal density derived by NRTA and the reference value. This indicates that the evaluated data libraries not always reflect the quality of existing experimental data. In addition, the bias in case the ENDF/B-VII.1 parameters are used, is not covered by the uncertainty of the resonance parameters. This confirms the conclusions in Ref. [6] that most of the covariance data for resonance parameters are underestimated in the recommended data libraries. Unfortunately Trkov et al. [188] do not provide any information on the production of the covariance of the parameters to validate the quality of their covariance data.

The impact of the uncertainty of the resonance parameters to characterize a spent fuel sample by NRTA was verified using the numerical study addressed in section 5. Based on a simulated transmission the uncertainties of resonance parameters of ^{235}U and ^{238}U were propagated towards the fitted areal densities. Three resonances of ^{235}U at 8.76 eV, 12.39 eV and 19.30 eV and two resonances of ^{238}U at 6.67 eV and 20.87 eV were considered. Table 15 summarizes the parameters of the considered resonances together with their uncertainties. The data were taken from the JENDL-4.0 library [165]. The parameter covariances of ^{235}U and ^{238}U were based on Ref. [189]. Fig. 57 shows the generated transmission together with the energy regions that were considered. The full covariance matrix of the resonance parameters was propagated using Eq. (33). In addition, a 5% normalization uncertainty and a 10 K uncertainty on the effective temperature were propagated. The result of this study is summarized in Table 16. The total uncertainty of the areal densities are given together with the contribution of different components. The uncertainty of the resonance parameters of ^{235}U directly lead to an increase of the uncertainty of the ^{235}U areal density. On the other hand, the impact due to the uncertainty of the resonance parameters of ^{238}U is rather low. The level to which the uncertainty on the resonance parameters propagates, strongly depends on the uncorrelated uncertainty of the experimental transmission. They are even lower compared to nominal uncertainties that can be achieved by applying destructive analytical techniques. Only when the uncertainties of both the normalization and resonance parameters are propagated the influence of the uncertainty on the resonance parameters of ^{238}U is visible. This indicates that the uncertainty of the resonance parameters, the normalization and temperature do not fully translate into an uncertainty of the areal density when they are considered individually. A similar observation was already made in Ref. [6] in a study of the impact of the normalization factor when analyzing capture

Table 15: Parameters and uncertainties of selected resonances of ^{235}U and ^{238}U taken from the JENDL-4.0 evaluated library [165].

Isotope	E / eV	Γ_γ / meV	Γ_n / meV	Γ_{FA} / meV	Γ_{FB} / meV
^{235}U	8.760	37.692 ± 0.553	0.966 ± 0.011	101.030 ± 3.432	-6.253 ± 2.731
	12.390	40.985 ± 0.686	1.371 ± 0.025	17.300 ± 10.22	-16.389 ± 10.97
	19.296	40.103 ± 0.964	2.588 ± 0.077	-32.277 ± 13.66	39.465 ± 13.02
^{238}U	6.674	23.00 ± 0.403	1.476 ± 0.020	–	–
	20.872	22.86 ± 1.719	10.094 ± 0.497	–	–

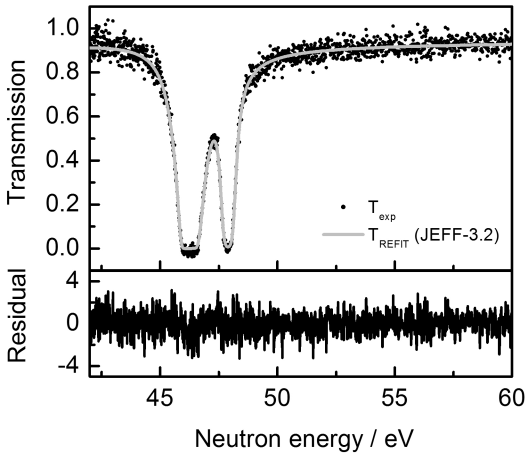

Fig. 56: Result of a transmission measurement on a natural tungsten sample together with the result of a RSA with REFIT using JEFF-3.2 resonance parameters. The residual of the fit of the areal density of ^{183}W is shown in the lower part of the figure.

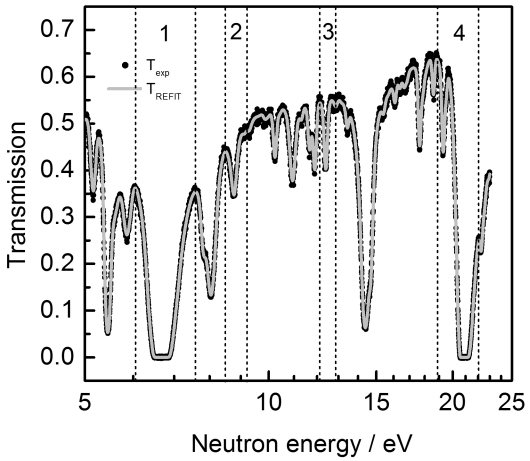

Fig. 57: Simulated transmission of an NRTA measurement of a spent fuel sample. The four energy region considered for the propagation of the resonance parameter uncertainties of ^{235}U and ^{238}U are indicated.

cross section data.

8 Summary and conclusions

Neutron resonance transmission analysis (NRTA) and neutron resonance capture analysis (NRCA) were presented as non-destructive analysis tools for a variety of applications ranging from archaeology, combating illicit trafficking of explosives and drugs, materials studies to the characterisation of nuclear materials including nuclear fuel and waste. They rely on well established methodologies of neutron resonance spectroscopy.

A study of the basic principles reveals the complexity of NRCA compared to NRTA. In most cases, additional flux and normalization measurements are required for NRCA, while NRTA can be considered as an absolute measurement. Moreover, the relation between the capture yield and areal densities is much more complex compared to the direct relation between experimental transmission and areal densities in case of NRTA. In addition, for the analysis of NRTA data only total cross sections are required as nuclear data. When NRCA data are analysed both capture and scattering cross sections are needed. The uncertainties on total cross sections are mostly considerably smaller compared to uncertainties on capture and scattering cross sections. NRTA can be considered as one of the most accurate non-destructive methods for the characterisation of materials.

Table 16: Relative uncertainty of the fitted areal densities (u_n/n) of ^{235}U and ^{238}U taking into account different uncertainty components due to counting statistics ($\boldsymbol{U}_{\vec{z}}$), resonance parameters ($\boldsymbol{V}_{\vec{RP}}$), temperature ($\boldsymbol{V}_T$) and normalization ($\boldsymbol{V}_N$).

Covariance components				$100 \times u_n/n$	
$\boldsymbol{U}_{\vec{z}}$	$\boldsymbol{V}_T$	$\boldsymbol{V}_N$	$\boldsymbol{V}_{\vec{RP}}$	^{235}U	^{238}U
×				0.51	0.08
×	×			0.55	0.10
×		×		0.62	0.13
×			×	1.30	0.25
×	×		×	1.30	0.26
×		×	×	1.30	1.15
×	×	×	×	1.31	1.16

A combination of NRTA and NRCA, referred to as Neutron Resonance Densitometry (NRD), was presented as a non-destructive method for the characterisation of melted fuel formed in severe nuclear accidents. Problems due to the sample temperature, diversity in shape and size of the samples and the presence of strong absorbing matrix materials were discussed. A model to estimate the transmission through heterogeneous samples was implemented in the resonance shape analysis code REFIT. This model together with a procedure to account for the presence of matrix materials was validated based on results of both Monte Carlo simulations and experimental data obtained at the time-of-flight facility GELINA. Finally, it was demonstrated that Neutron Resonance Densitometry can be applied to characterize debris samples of melted fuel and that an accuracy of 2% on the areal density of ^{235}U and ^{239}Pu can be reached.

Acknowledgments

The authors would like to thank M.C. Moxon for all his efforts related to resonance spectroscopy and in particular for the development of the resonance shape analysis code REFIT, and to H. Postma for his contribution to the implementation and applications of NRCA at GELINA. We are also very grateful to W. Mondelaers and A. Plompen for their critical reading of the manuscript.

References

[1] E.P. Wigner and L. Eisenbud, “Higher angular momenta and long range interaction in resonance reactions", Phys. Rev. **72**, 29 – 41 (1947).

[2] A.M. Lane and R.G. Thomas,“R-matrix theory of nuclear reactions", Rev. Mod. Phys. **30**, 257 – 353 (1958).

[3] F.H. Fröhner, “Evaluation and analysis of nuclear resonance data", JEFF Report 18, NEA/OECD (2000).

[4] H. Postma and P. Schillebeeckx, “Neutron Resonance Capture and Transmission Analysis”, Encyclopedia of Analytical Chemistry (John Wiley & Sons Ltd), pp. 1-22 (2009).

[5] P. Schillebeeckx, A. Borella, F. Emiliani, G. Gorini, W. Kockelmann, S. Kopecky, C. Lampoudis, M. Moxon, E. Perelli Cippo, H. Postma, N.J. Rhodes, E.M. Schooneveld and C. Van Beveren, “Neutron resonance spectroscopy for the characterization of materials and objects”, J. Instrum. **7**, C03009 – 18 (2012).

[6] P. Schillebeeckx, B. Becker, Y. Danon, K. Guber, H. Harada, J. Heyse, A.R. Junghans, S. Kopecky, C. Massimi, M. Moxon, N. Otuka, I. Sirakov and K. Volev, “Determination of Resonance Parame-

ters and their Covariances from Neutron Induced Reaction Cross Section Data", Nucl. Data Sheets **113**, 3054 – 3100 (2012).

[7] G.L. Molnár, "Handbook of Prompt Gamma Activation Analysis with Neutron Beams", Kluwer Academic Publishers, Dordrecht, The Netherlands, Ed. Gábor L. Molnár, 2004.

[8] H. Harada, F. Kitatani, M. Koizumi, H. Tsuchiya, J. Takamine, M. Kureta, H. Iimura, M. Seya, B. Becker, S. Kopecky and P. Schillebeeckx, "Proposal of Neutron Resonance Densitometry for Particle Like Debris of Melted Fuel using NRTA and NRCA", Proc. of the 35^{th} ESARDA Symposium on Safeguards and Nuclear Non-Proliferation, 28 – 30 May 2013, Brugge (Belgium).

[9] P. Schillebeeckx, S. Abousahl, B. Becker, A. Borella, H. Harada, K. Kauwenberghs, F. Kitatani, M. Koizumi, S. Kopecky, A. Moens, G. Sibbens and H. Tsuchiya, "Development of Neutron Resonance Densitometry at the GELINA TOF Facility", ESARDA Bulletin **50**, 9 – 17 (2013).

[10] J.A. Harvey, "Experimental neutron resonance spectroscopy", Academic Press, New York and London, Ed. J. A. Harvey, 1970.

[11] F.W.K. Firk, "Neutron time-of-flight spectrometers", Nucl. Instr. Meth. **162**, 539 – 563 (1979).

[12] H. E. Jackson and J. E. Lynn, "Resonant absorption of neutrons by crystals", Phys. Rev. **127**, 461 – 468 (1962).

[13] H.A. Bethe and G. Placzek, "Resonance Effects in Nuclear Processes", Phys. Rev. **51**, 450 – 484 (1937).

[14] H.A. Bethe, "Nuclear Physics B. Nuclear Dynamics, Theoretical", Rev. Mod. Phys. **9**, 69 – 244 (1937).

[15] W. E. Lamb, "Capture of neutrons by atoms in a crystal", Phys. Rev. **55**, 190 – 197 (1939).

[16] J.E. Lynn and E.R. Rae, "The analysis of neutron spectrometer resonance data", J. Nuclear Energy **4**, 418 – 444 (1957).

[17] N.W. Ashcroft and N.D. Mermin, "Solid State Physics", Holt, Rinehart and Winston (New York), 1976.

[18] C. Lampoudis, S. Kopecky, O. Bouland, F. Gunsing, G. Noguere, A.J.M.Plompen, C. Sage, P. Schillebeeckx and R. Wynants, "Neutron transmission and capture cross section measurements for ^{241}Am at the GELINA facility", Eur. Phys. J. Plus **128**, 86 –20 (2013).

[19] M. S. Nelkin, D. E. Parks, "Effects of chemical binding on nuclear recoil", Phys. Rev. **119**, 1060 – 1068 (1960).

[20] G.M. Borgonovi, D.H. Houston, J.U. Koppel and E.L. Slaggie, "Crystal-binding effects on Doppler broadening of neutron absorption resonances", Phys. Rev. C **1**, 2054 – 2059 (1970).

[21] D. Naberejnev, C. Mounier and R. Sanchez, "The influence of crystalline binding on resonant absorption", Nuc. Sci. Eng. **131**, 222 – 229 (1999).

[22] J.E. Lynn and W.J. Trela, "Resonance neutron methods for determining statistical properties of phonon spectra", Nucl. Instr. Meth. Phys. Res. B **108**, 147 – 158 (1996).

[23] J.E. Lynn, W.J. Trela and K. Meggers, "Neutron Doppler broadening studies of tantalum and tungsten metal", Nucl. Instr. Meth. Phys. Res. B **192**, 318 – 330 (2002).

[24] F. G. P. Seidl, D.J. Hughes, H. Palevsky, J. S. Levin, W. Y. Kato and N. G. Sjöstrand, "Fast chopper time-of-flight measurement of neutron resonances", Phys. Rev. **95**, 476 – 499 (1954).

[25] K.H. Böckhoff, A. D. Carlson, O. A. Wasson, J. A. Harvey and D. C. Larson, "Electron linear accelerators for fast neutron data measurements in support of fusion energy applications", Nucl. Sci. Eng. **106**, 192 – 207 (1990).

[26] P.E. Koehler, "Comparison of white neutron sources for nuclear astrophysics experiments using very small samples", Nucl. Inst. Meth. A **460**, 352 – 361 (2001).

[27] J. Klug, E. Altstadt, C. Beckert, R. Beyer, D. Freiesleben, V. Galindo, E. Grosse, A.R. Junghans, D. Legrady, B. Naumann, K. Noack, G. Rusev, K.D. Schilling, R. Schlenk, R. Schneider, A. Wagner,

and F.-P. Weiss, “Development of a neutron time-of-flight source at the ELBE accelerator", Nucl. Inst. Meth. A **577**, 641 – 653 (2007).

[28] W. Mondelaers and P. Schillebeeckx, “GELINA, a neutron time-of-flight facility for high-resolution neutron data measurements”, Notiziario Neutroni e Luce di Sincrotrone **11 no.2**, 19 – 25 (2006).

[29] http://www.isis.stfc.ac.uk/ (16/03/2014)

[30] F. Maekawa, M. Harada, K. Oikawa, M. Teshigawara, T. Kai, S. Meigo, M. Ooi, S. Sakamoto, H. Takada, M. Futakawa, T. Kato, Y. Ikeda, N. Watanabe, T. Kamiyama, S. Torii, R. Kajimoto, M. Nakamura, “First neutron production utilizing J-PARC pulsed spallation neutron source JSNS and neutronic performance demonstrated”, Nucl. Instr. Meth. Phys. Res. A **620**, 159 – 165 (2011).

[31] K. Kino, M. Furusaka, F. Hiraga, T. Kamiyama, Y. Kiyanagi, K. Furutaka, S. Goko, H. Harada, M. Harada, T. Kai, A. Kimura, T. Kin, F. Kitatani, M. Koizumi, F. Maekawa, S. Meigo, S. Nakamura, M. Ooi, M. Ohta, M. Oshima, Y. Toh, M. Igashira, T. Katabuchi, and M. Mizumoto, “Measurement of energy spectra and spatial distributions of neutron beams provided by the ANNRI beamline for capture cross-section measurements at the J-PARC/MLF", Nucl. Instr. Meth. Phys. Res. A **626-627**, 58 – 66 (2011).

[32] K. Kino, M. Furusaka, F. Hiraga, T. Kamiyama, Y. Kiyanagi, K. Furutaka, S. Goko, K.Y. Hara, H. Harada, K. Horose, T. Kai, A. Kimura, T. Kin, F. Kitatani, M. Koizumi, F. Maekawa, S. Meigo, S. Nakamura, M. Ooi, M. Ohta, M. Oshima, Y. Toh, M. Igashira, T. Katabuchi, M. Mizumoto and J. Hori, “Energy resolution of pulsed neutron beam provided by the ANNRI beamline at the J-PARC/MLF", Nucl. Instr. Meth. Phys. Res. A **736**, 66 – 74 (2014).

[33] H. Hasemi, M. Harada, T. Kai, T. Shinohara, M. Oi, K. Kino, M. Segawa, T. Kamiyama and Y. Kiyanagi, “Development of a method for quantitative evaluation of nuclide density by neutron resonance transmission at NOBORU instrument in J-PARC/MLF”, submitted to Nucl. Instr. Meth. Phys. Res. A.

[34] E. Perelli Cippo, A. Borella, G. Gorini, W. Kockelmaan, A. Pietropaolo, H. Postma, N.J. Rhodes, P. Schillebeeckx, E.M. Schooneveld, M. Tardocchi, R. Wynants and the ANCIENT CHARM collaboration, “A detector system for neutron resonance capture imaging”, Nucl. Instr. Meth. Phys. Res. A **623**, 693 – 698 (2010) .

[35] H. J. Groenewold and H. Groendijk, Physica **XIII**, 141 – 152 (1947).

[36] A. Michaudon, “The production of moderated neutron beams from pulsed accelerators", J. Nucl. Energy **17** (part A/B), 165 –186 (1963).

[37] M. Flaska, A. Borella, D. Lathouwers, L.C. Mihailescu, W. Mondelaers, A.J.M. Plompen, H. van Dam, T.H.J.J. van der Hagen, Nucl. Instr. Meth. Phys. Res. A **531**, 392 – 406 (2004).

[38] D. Ene, C. Borcea, S. Kopecky, W. Mondelaers, A. Negret and A.J.M. Plompen, “Global characterisation of the GELINA facility for high-resolution neutron time-of-flight measurements by Monte Carlo simulations", Nucl. Instr. Meth. Phys. Res. A **618**, 54 – 68 (2010).

[39] F. Gunsing et al. (n_TOF Collaboration), “Status and outlook of the neutron time-of-flight facility n_TOF at CERN", Nucl. Inst. Meth. Phys. Res. B **261**, 925 – 929 (2007).

[40] C. Coceva, R. Simonini and D. K. Olsen, “Calculation of the ORELA neutron moderator spectrum and resolution function", Nucl. Instr. Meth. **211**, 459 – 467 (1983).

[41] M.E. Overberg, B. E. Moretti, R.E. Slovacek and R.C. Block, “Photoneutron target development for the RPI linear accelerator", Nucl. Instr. Meth. Phys. Res. A **438**, 253 – 264 (1999).

[42] M.C. Moxon and J.B. Brisland, “GEEL REFIT, A least squares fitting program for resonance analysis of neutron transmission and capture data computer code", AEA-InTec-0630, AEA Technology, October (1991).

[43] P.E. Koehler,“A determination of the energy resolution at LANSCE”, Nucl. Instr. Methd. A **350**, 511 – 516 (1994).

[44] S. Ikeda and J. M. Carpenter,“Wide-energy-range, high-resolution measurements of neutron pulse shapes of polyethylene moderators", Nucl. Instr. Meth. Phys. Res. A **239**, 536 – 544 (1985).

[45] I. Cole and C.G. Windsor, “The lineshapes in pulsed neutron powder diffraction”, Nucl. Inst. Meth. **171**, 107 – 113 (1980).

[46] M.S. Moore, “Rate dependence of counting losses in neutron time-of-flight measurementsâĂİ, Nucl. Inst. Meth. **169**, 245 – 247 (1980).

[47] L.C. Mihailescu, A. Borella, C. Massimi and P. Schillebeeckx, “Investigations for the use of fast digitizers with C_6D_6 detectors for radiative capture measurements at GELINA", Nucl. Instr. Meth. Phys. Res. A **600**, 453 – 459 (2009).

[48] I. Sirakov, B. Becker, R. Capote, E. Dupont, S. Kopecky, C. Massimi and P. Schillebeeckx, “Results of total cross section measurements for ^{197}Au in the neutron energy region from 4 to 108 keV at GELINA”, Eur. Phys. J. A **49** 144, 1- 10 (2013)

[49] J. A. Harvey and N. W. Hill, “Scintillation detectors for neutron physics research", Nucl. Instr. Meth. **162**, 507 – 529 (1979).

[50] S. Kopecky, I. Ivanov, M. Moxon, P. Schillebeeckx, P. Siegler and I. Sirakov, “The total cross section for the 0.178 eV resonance of ^{113}Cd", Nucl. Instr. Meth. Phys. Res. B **267**, 2345 – 2350 (2009).

[51] B. Becker, S. Kopecky, H. Harada and P. Schillebeeckx, “Measurement of the direct particle transport through stochastic media using neutron resonance transmission analysis", Eur. Phys. J. Plus **129**, 58 – 9 (2014).

[52] H. Postma and P. Schillebeeckx, “Non-destructive analysis of objects using neutron resonance capture”, J. Radioanal. Nucl. Chem. **265**, 297 – 302 (2005).

[53] A. Borella, K. Volev, A. Brusegan, P. Schillebeeckx, F. Corvi, N. Koyumdjieva, N. Janeva and A.A. Lukyanov, “Determination of the ^{232}Th(n,γ) cross section from 4 to 140 keV at GELINA", Nucl. Sci. Eng. **152**, 1 – 14 (2006).

[54] C. Massimi et al. (the n_TOF collaboration), “^{197}Au cross section in the resonance region”, Phys. Rev. C **81**, 044616 – 22 (2010).

[55] B. C. Diven, J. Terrell and A. Hemmendinger, “Radiative capture cross sections for fast neutrons", Phys. Rev. **120**, 556 – 569 (1960).

[56] K. Wisshak, K. Guber, F. Käppeler, J. Krisch, H. Müller, G. Rupp and F. Voss, “The Karlsruhe 4π barium fluoride detector”, Nucl. Instr. Meth. Phys. Res. A **292**, 595 – 618 (1990).

[57] M. Heil, R. Reifarth, M.M. Fowler, R.C. Haight, F. Käppeler, R.S. Rundberg, E.H. Seabury, J.L. Ullmann, J.B. Wilhelmy and K. Wisshak, “A 4 π BaF_2 detector for (n,γ) cross-section measurements at a spallation neutron source", Nucl. Instr. Meth. Phys. Res. A **459**, 229 – 246 (2001).

[58] C. Guerrero et al. (the n_TOF collaboration), “The n_TOF Total Absorption Calorimeter for neutron capture measurements at CERN", Nucl. Instr. Meth. Phys. Res. A **608**, 424 – 433 (2009).

[59] J. Goto, H. Harada, F. Kitatani, Y. Nagai, M. Oshima, M. Segawa and Y. Toh, “Design of a 4πLaBr$_3$(Ce) spectrometer for neutron capture cross section measurements", J. Korean Phys. Soc. **59**, 1585 - 1588 (2011).

[60] M.C. Moxon and E.R. Rae, “A gamma-ray detector for neutron capture cross-section measurements", Nucl. Instr. Meth. **24**, 445 – 455 (1963).

[61] A. Borella, G. Aerts, F. Gunsing, M. Moxon, P. Schillebeeckx and R. Wynants, “The use of C_6D_6 detectors for neutron induced capture cross-section measurements in the resonance region", Nucl. Instr. Meth. Phys. Res. A **577**, 626 – 640 (2007).

[62] R.L. Macklin and J.H. Gibbons, “Capture-cross-section studies for 30- 220-keV neutron using a new technique”, Phys. Rev. **159**, 1007 – 1012 (1967).

[63] R. L. Macklin, R. B. Perez, G. de Saussure and R. W. Ingle, “High energy resolution measurement

of the ^{238}U neutron capture yield from 1 to 100 keV", Ann. Nucl. Energy **18**, 567 – 583 (1991).

[64] A. Kimura, T. Fujii, S. Fukutani, K. Furutaka, S. Goko, K. Y. Hara, H. Harada, K. Hirose, J. Hori, M. Igashira, T. Kamiyama, T. Katabuchi, T. Kin, K. Kino, F. Kitatani, Y. Kiyanagi, M. Koizumi, M. Mizumoto, S. Nakamura, M. Ohta, M. Oshima, K. Takamiya and Y. Toh, "Neutron-capture cross-sections of ^{244}Cm and ^{246}Cm measured with an array of large germanium detectors in the ANNRI at J-PARC/MLF", J. Nucl. Sci. Technol. **49**, 708 – 724 (2012).

[65] C. Guerrero et al. (the n_TOF collaboration), "Characterization of the new n_TOF neutron beam: Fluence, profile, and resolution", **59**, 1624 – 1627 (2011).

[66] A.D. Carlson, V.G. Pronyaev, D.L. Smith, N.M. Larson, Z. Chen, G.M. Hale, F.-J. Hambsch, E.V. Gai, Soo-Youl Oh, S.A. Badikov, T. Kawano, H.M. Hofman, H. Vonach, and S. Tagesen, "International evaluation of neutron cross section standards", Nucl. Data Sheets **110**, 3215 – 3324 (2009).

[67] A. Borella, F. Gunsing, M. Moxon, P. Schillebeeckx and P. Siegler, "High-resolution neutron transmission and capture measurements of the nucleus ^{206}Pb", Phys. Rev. C **76**, 014605 – 18 (2007).

[68] G. Giorginis and V. Khriatchkov, "The effect of particle leaking and its implications for measurements of the (n,α) reaction on light elements by using ionization chambers", Nucl. Instr. Meth. Phys. Res. A **538**, 550 – 558 (2005).

[69] C. Bastian, "General procedures and computational methods for generating covariance matrices", Proc. Int. Symposium on Nuclear Data Evaluation Methodology, Brookhaven National Laboratory, USA, October 12-16, 1992, pp. 642 – 649 (1992).

[70] B. Becker, C. Bastian, F. Emiliani, F. Gunsing, J. Heyse, K. Kauwenberghs, S. Kopecky, C. Lampoudis, C. Massimi, N. Otuka, P. Schillebeeckx, I. Sirakov, "Data reduction and uncertainty propagation of time-of-flight spectra with AGS", J. Instrum. **7**, P11002 – 21 (2012).

[71] F. Gunsing, P. Schillebeeckx and V. Semkova, "Summary Report of the Consultants' Meeting on EXFOR Data in Resonance Regioin and Spectrometer Response Function", INDC(NDS)-0647 (2013).

[72] N. Otuka, A. Borella, S. Kopecky, C. Lampoudis and P. Schillebeeckx, "Database for time-of-flight spectra with their covariances", J. Korean Phys. Soc. **59**, 1314 – 1317 (2011).

[73] N. Otuka (ed.), "Summary report of the IAEA technical meeting on the international network of nuclear reaction data centres, Vienna, Austria, 23-24 May, 2011", INDC(NDS)-0593, IAEA (2011).

[74] K.B. Petersen and M.S. Pedersen, The Matrix Cookbook, Version 20121115, Technical University of Denmark (2012) `http://www2.imm.dtu.dk/pubdb/p.php?3274` (16/03/2014)

[75] N.M. Larson, "Updated users guide for SAMMY: Multilevel R-matrix fits to neutron data using Bayes' equations", Report ORNL/TM-9179/R8 and ENDF-364/R2, Oak Ridge National Laboratory, USA, (2008).

[76] F. H. Fröhner,"Assignment of uncertainties to scientific data", Nucl. Sci. Eng. **126**, 1 – 18 (1997).

[77] C. De Saint Jean, G. Noguere, B. Habert and B. Iooss, "A Monte Carlo approach to nuclear model parameter uncertainties propagation", Nucl. Sci. Eng. **161** , 363 – 370 (2009).

[78] B. Habert, C. De Saint Jean, G. Noguere, L. Leal and Y. Rugama, "Retroactive generation of covariance matrix of nuclear model parameters using marginalization techniques", Nucl. Sci. Eng. **166**, 276 – 287 (2010).

[79] C. W. Reich and M. S. Moore, "Multilevel formula for the fission process", Phys. Rev. **111**, 929 – 933 (1958).

[80] P. Schillebeeckx, A. Borella, S. Kopecky, C. Lampoudis, C. Massimi, and M. Moxon, "Neutron resonance spectroscopy at GELINA", J. Korean Phys. Soc. **59**, 1563 – 1568 (2011).

[81] H. Postma, M. Blaauw, P. Schillebeeckx, G. Lobo, R.B. Halbertsma and A.J. Nijboer, "Non-

destructive elemental analysis of copper-alloy artefacts with epithermal neutron-resonance capture", Czech. J. of Physics, **53**, A233 – A240 (2003).

[82] P.A.C. Schut, W. Kockelmann, H. Postma, D. Visser, P. Schillebeeckx, and R. Wynants, "Neutron resonance capture and neutron diffraction analysis of Roman bronze water taps", J. Radioanal. Nucl. Chem., **278**, 151 – 164 (2008).

[83] H. Postma, L. Amkreutz, A. Borella, M. Clarijs, H. Kamermans, W. Kockelmann, A. Paradowska, P. Schillebeeckx and D. Visser, "Non-destructive analysis of the Buggenum sword by neutron resonance capture analysis and neutron diffraction", J. Radioanal. Nucl. Chem., **283**, 641 – 652 (2010).

[84] H. Postma, P. Schillebeeckx and W. Kockelmann, "The metal compositions of a series of Geistingen-type socketed axes", J. Archeaological Science, **38**, 1810 – 1817 (2011).

[85] H. Postma, P. Schillebeeckx and R.B. Halbertsma, "Neutron Resonance Capture Analysis of Some Genuine and Fake Etruscan Copper Alloy Statuettes", Archaeometry **46**, 635 – 646 (2004).

[86] G. Noguere, O. Bouland, A. Brusegan, P. Schillebeeckx, P. Siegler, A. Leprêtre, N. Herault, and G. Rudolf, "Neutron capture and total cross sections of ^{127}I and ^{129}I", Phys. Rev. C **74**, 054602 – 19 (2006).

[87] R.C. Perego, H. Postma, M. Blaauw, P. Schillebeeckx and A. Borella, "Neutron resonance capture analysis: improvements of the technique for resonances above 3 keV and new applications", J. Radioanal. Nucl. Chem. **271**, 89 – 94 (2007).

[88] H. Weigmann and J. Winter, "Neutron radiative capture in Cu", Zeitschrift fur Phys., **23**, 411 – 419 (1968).

[89] P. Schillebeeckx, A. Borella, J. C. Drohe, R. Eykens, S. Kopecky, C. Massimi, L. C. Mihailescu, A. Moens, M. Moxon, and R. Wynants,"Target requirements for neutron-induced cross-section measurements in the resonance region", Nucl. Instr. Meth. Phys. Res. A **613**, 378 – 385 (2010)

[90] M.C. Moxon, D.A.J. Endacott, T.J. Haste, J.E. Jolly, J.E. Lynn and M.G. Sowerby, "Differential neutron cross-sections of natural hafnium and its isotopes for neutron energies up to 30 eV", AERE – R 7864, 1974.

[91] M.C. Moxon, J.B. Brisland, S. Croft and D.S. Bond, "The measurement of the ^{10}B content of enriched samples of boron using neutron time-of-flight techniques", Proc. Int. Conf. Nuclear Data for Science and Technology, S.M. Qaim (Ed.), Jülich, pp. 442 – 444 (1991).

[92] J.C. Blackmon, A.E. Champagne, J.K. Dickens, J.A. Harvey, M.A. Hofstee, S. Kopecky, D.C. Larson, D.C. Powell, S. Raman and M.S. Smith, "Measurement of ^{7}Li(n,γ_0)^{8}Li cross sections at E_n = 1.5 – 1340 eV", Phys. Rev. C **54**, 383 – 388 (1996).

[93] H.G. Priesmeyer and U. Harz, "Isotopic content determination in irradiated fuel by neutron transmission analysis", Atomkernenergie **25**, 109 – 113 (1975).

[94] J.W. Behrens, R.A. Schrack, A.D. Carlson and C.D. Bowman, "Resonance Neutron Radiography for Nondestructive Evaluation and Assay Applications", Proc. Conf. Nuclear Cross Sections for Technology, Knoxville, Tennessee, October 22 – 26, 1979, NBS Special Publication 594, pp. 436 – 439 (1980).

[95] J. W. Behrens, R. G. Johnson and R. A. Schrack, "Neutron resonance transmission analysis of reactor fuel samples", Nucl. Technol. **67**, 162 – 168 (1984).

[96] R.A. Schrack, "Uranium-235 Measurement in Waste Material by Resonance Neutron Radiography", Nucl. Technol. **67**, 326 – 332 (1984).

[97] R.A. Schrack, "New applications of resonance neutron radiography", Int. Conf. on Nuclear Data for Basic and Applied Science, Santa Fe, May 13 – 17, pp. 1309 – 1313 (1985).

[98] R.A. Schrack, "NBS Work on Neutron Resonance Radiography", Report of a Workshop on Neutron Resonance Radiography Held at the Los Alamos National Laboratory, July 27 – 29 , 1987,

LA – 11393 – C, pp. 100 – 115 (1987)

[99] R.A. Schrack, "A microchannel plate neutron detector", Nucl. Instr. Meth. **222**, 499 – 506 (1984).

[100] K.J.R. Rosman and P.D.P. Taylor, "Isotopic compositions of the elements 1997", Pure & Appl. Chem. **70**, 217 – 235 (1998).

[101] D. Vartsky, "Prospects of Fast-Neutron Resonance Radiography and its Requirements for Instrumentation", Int. Workshop on Fast Neutron Detectors and Applications,", University of Cape Town, South Africa, 3- 6 April 2006, Proc. of Science (FNDA2006) 084, pp. 1- 13 (2006).

[102] B.D. Sowerby and J.R. Tickner, "Recent advances in fast neutron radiography for cargo inspection", Nucl. Instr. Meth. Phys. Res. A **580**, 799 – 802 (2007).

[103] W.H. Makky, T.G. Miller, D.L. Smithn, J.W. Meadows and P.T. Guenther,"Tailoring neutron spectra for fast neutron spectroscopy", Proc. SPIE, **1737**, 197 – 209 (1993).

[104] T.N. Massey, T.W. Covell, S.I. Al-Quraishi, D.K. Jacobs, C.E. Brient, S.M. Grimes, W.B. Howard, J. Yanth, D.L. Smith and B.J. Micklich, "Neutrons produced by proton and deuteron bombardment of beryllium", Fusion Eng. Des., **37**, 57 - 63 (1997).

[105] V.O. de Haan, T.H.J.J. van der Hagen, A. Fedorov, A. van Veen and P.F.A. de Leege, "Conceptual design of a novel high-frame-rate fast-neutron radiography facility", Nucl. Instr. Meth. Phys. Res. A **539**, 321 – 324 (2005).

[106] C. Chen and R.C. Lanza, "Fast Neutron Resonance Radiography for Elemental Imaging: Theory and Applications", IEEE Trans. Nucl. Sci. **49**, 1919 – 1924 (2002).

[107] W.L. Raas, B. Blackburn, E. Boyd, J. M. Hall, G. Kohse, R. Lanza, B. Rusnak and J.I.W. Watterson, "Neutron Resonance Radiography for Explosives Detection: Technical Chalelnges", IEEE Nuclear Science Symposium and Medical Imaging Conference, Fajardo, PR, US, October 23 - 29, 2005, UCRL-CONF-217017 (2005).

[108] J. Guzek, K. Richardson, C.B. Franklyn, A. Waites, W.R. McMurray, J.I.W. Watterson and U.A.S. Tapper, "Development of high pressure deuterium gas targets for the generation of intense monoenergetic fast neutron beams", Nucl. Instr. Meth. Phys. Res. B **152**, 515 – 526 (1999).

[109] John I.W. Watterson and Richard M. Ambrosi, "Some fundamental considerations in resonance imaging using fast neutrons", Nucl. Instr. Meth. Phys. Res. A **513**, 367 –373 (2003).

[110] H.J. Brede, G. Dietze, K. Kudo, U.J. Schrewe, F. Tancu and C. Wen, "Neutron yields from thick Be targets bombarded with deuterons or protons", Nucl. Instr. Meth. Phys. Res. A **274**, 332 – 344 (1989).

[111] J.W. Meadows, "The ^{9}Be(d,n) thick-target neutron spectra for deuteron energies between 2.6 and 7.0 MeV", Nucl. Instr. Meth. Phys. Res. A **324**, 239 – 246 (1993).

[112] J.C. Overley, "Element-sensitive computed tomography with fast neutrons", IEEE Trans. Nucl. Sci. **30**, 1677 – 1679 (1983).

[113] J.C.Overley, "Element-sensitive computed tomography with fast neutrons", Int. J. Appl. Radiat. Isot. **36**, 185 – 192 (1985).

[114] J.C.Overley, "Determination of H,C,N,O Content of Bulk Materials from Neutron-Attenuation Measurements", Nucl. Instr. Meth. Phys. Res. B **24/25**, 1058 – 1062 (1987).

[115] J.C.Overley, M.S. Chmelik, R.J. Rasmussen, R.M.S. Schofield and H.W. Lefevre, "Explosives detection through fast-neutron time-of-flight attenuation measurements", Nucl. Instr. Meth. Phys. Res. B **99**, 728 – 732 (1995).

[116] J.C.Overley, M.S. Chmelik, R.J. Rasmussen, R.M.S. Schofield, G.E. Sieger and H.W. Lefevre, "Explosives detection via fast neutron transmission spectroscopy", Nucl. Instr. Meth. Phys. Res. B **251**, 470 – 478 (2006).

[117] T.G. Miller and W.H. Makky, "Application of fast neutron spectroscopy/radiography to airport security", Proc. SPIE, **1737**, 184 – 196 (1993).

[118] T.G. Miller, P.K. Van Staagen, B.C. Gibson and R.A. Kraus, "Contraband Identification in Sealed Containers Using Neutron Transmission", Proc. SPIE, **2867**, 215 – 218 (1996).

[119] T.G. Miller, P.K. Van Staagen, B.C. Gibson, J.L. Orthel and R.A. Kraus, "Contraband detection using neutron transmission", Proc. SPIE **2936**, 102 – 111 (1997).

[120] H. Brede, M. Cosack, G. Dietze, H. Gumpert, S. Guldbakke, R. Jahr, M. Kutscha, D. Schlegel-Bickmann and H. Schölermann, "The Braunschweig accelerator facility for fast neutron research:1 : Building design and accelerators", Nucl. Instr. Meth. **169**, 349 – 358 (1980).

[121] V. Dangendorf, G. Laczko, G. Kersten, O. Jagutzki and U. Spilmann, "Fast Neutron Resonance Radiography in a Pulsed Neutron Beam", Contribution to the 7^{th} World Conference on Neutron Radiography, Rome, September 2002.

[122] V. Dangendorf, C. Kersten, G. Laczko, D. Vartsky, I. Mor, M.B. Goldberg, G. Feldman, A. Breskin, R. Chechik, O. Jagutzky, and U. Spilmann, "Detectors for energy-resolved fast-neutron imaging", Nucl. Instr. Meth. Phys. Res. A **535**, 93 – 97 (2004).

[123] D. Vartsky, I. Mor, M. B. Goldberg, I. Mardor, G. Feldman, D. Bar, A. Shor, V. Dangendorf, A. Breskin and R. Chechik, "Time-resolved fast neutron imaging: simulation of detector performance", Nucl. Instr. Meth. Phys. Res. A **542**, 206 – 212 (2005).

[124] D. Vartsky, G. Feldman, I. Mor, M.B. Goldberg, D. Bar and V. Dangendorf, "Signal and noise analysis in TRION – Time-Resolved Integrative Optical Fast Neutron detector", J. Instrum. **4**, P02001 – 18 (2009).

[125] I. Mor, D. Vartsky, D. Bar, G. Feldman, M.G. Goldberg, D. Katz, E. Sayag, I. Shmueli, Y. Cohen, A. Tal, Z. Vagisch, B. Bromberger, V. Dangendorf, D. Mugai, K. Tittelmeier and M. Weierganz, 'High spatial resolution fast-neutron imaging detectors for Pulsed Fas-Neutron Transmission Spectroscopy", J. Instrum. **4**, P05016 – 24 (2009).

[126] I. Mor, D. Vartsky, G. Feldman, V. Dangendorf, D. Bar, M.B. Goldberg, K. Tittelmeier, B. Broomberger, W. Weierganz and M. Brandis, "Parameters affecting image quality with Time-Resolved Optical Integrative (TRION) detectors", Nucl. Instr. Meth. Phys. Res. A **640**, 192 – 199 (2011).

[127] I. Mor, D. Vartsky, V. Dangendorf, D. Bar, G. Feldman, M.B. Goldberg, K. Tittelmeier, B. Broomberger, M. Brandis and W. Weierganz"Parameters affecting temporal resolution of Time-Resolved Optical Integrative Detector (TRION)", J. Instrum. **8**, P11012 –13 (2013).

[128] V. Dangendorf, G. Laczko, M. Reginatto, D. Vartsky, M. Goldberg, I. Mor, A. Breskin and R. Chechik, "Detectors for time-of-flight fast neutron radiography 1. Neutron-counting gas detector", Nucl. Instr. Meth. Phys. Res. A **542**, 197 – 205 (2005).

[129] M. Brandis, D. Vartsky, V. Dangendorf, B. Bromberger, D. Bar, M.B. Goldberg, K. Tittelmeier, E. Friedman, A. Czasch, I. Mardor, I. Mor and M. Weierganz, "Neutron measurements with Time-Resolved Event-Counting Optical Radiation (TRECOR) detector", J. Instrum. **7**, C04003 – 10 (2012).

[130] P.H. Fowler, "Temperature Imaging Using Epithermal Neutrons", Report of a Workshop on Neutron Resonance Radiography Held at the Los Alamos National Laboratory, July 27 – 29 , 1987, LA – 11393 – C, pp. 46 – 80 (1987)

[131] J. Mayers, G. Baciocco and A.C. Hannon, "Temperature measurement by neutron resonance radiography", Nucl. Instr. Meth. Phys. Res. A **275**, 453 – 459 (1989).

[132] J.C. Frost, P. Meehan, S.R. Morris, R.C. Ward and J. Mayers, "Non-intrusive temperature measurement of the components of a working catalyst by neutron resonance radiography", Catal. Lett. **2**, 97 – 104 (1989)

[133] Y. Le Godec, M.T. Dove, D.J. Francis, S.C. Kohn, W.G. Marshall, A.R. Pawley, G.D. Price, S.A.T. Redfern, N. Rhodes, N.L. Ross, P.F. Schofield, E. Schooneveld, G. Syfosse, M.G. Tucker and M.D. Welch, "Neutron diffraction at simultaneous high temperatures and pressures, with measurement

of temperature by neutron radiography", Mineral. Mag. **65**, 737 – 748 (2001).

[134] H.J. Stone, M.G. Tucker, Y. Le Godec, F.E. Méducin, E.R. Cope, S.A. Hayward, G.P.J. Ferlat, W.G. Marschall, S. Manolopoulos, S.A.T. Redfern and M.T. Dove, "Remote determination of sample temperature by neutron resonance spectroscopy", Nucl. Instr. Meth. Phys. Res. A **547**, 601 – 615 (2005).

[135] H.J. Stone, M.G. Tucker, F.E. Méducin, M.T. Dove, S.A.T. Redfern, Y. Le Godec and W.G. Marshal, "Temperature measurements in a Paris-Edinburgh cell by neutron resonance spectroscopy", J. Appl. Phys. **98**, 064905 –10 (2005).

[136] T. Kamiyama, J. Ito, H. Noda, H. Iwasa, Y. Kiyanagi and S. Ikeda, "Computer tomography thermometry - an application of neutron resonance absorption spectroscopy", Nucl. Instr. Meth. Phys. Res. A **542**, 258 – 263 (2005).

[137] T. Kamiyama, H. Noda, J. Ito, H. Iwasa, Y. Kiyanagi and S. Ikeda, "Remote-sensing, Non-destructive, and Computed-tomography-assisted Thermometry by Neutron Resonance Spectroscopy", J. Neutron Res. **13**, 97 – 101 (2005).

[138] V.W. Yuan, J.D. Bowman, D.J. Funk, G.L. Morgan, R.L. Rabic, C.E. Ragan, J.P. Quintana and H.L. Stacy, "Shock Temperature Measurement Using Neutron Resonance Spectroscopy", Phys. Rev. Lett. **94**, 125504 – 4 (2005).

[139] J.D. Bowman, J.J. Szymanski, V.W. Yuan, C.D. Bowman and A. Silverman, "Current-mode detector for neutron time-of-flight studies", Nucl. Instr. Meth. Phys. Res. A **297**, 183 – 189 (1990).

[140] H.A. Mook, J.A. Harvey, and N.W. Hill, "Measurement of T_{eff} for Cu in $YBa_2Cu_3O_7$ by neutron resonance absorption", Phys. Rev. B **41**, 764 – 765 (1990).

[141] N.E. Hecker, H.A. Mook, J.A. Harvey, N.W. Hill, M. Moxon and J.A. Golovchenko, "Absence of anomalous vibrations in $YBa_2Cu_3O_{7-\delta}$", Phys. Rev. B **50**, 16129 – 16132 (1994).

[142] K. Tokuda, T. Kamiyama, Y. Kiyanagi, R. Moreh and S. Ikeda, "Direct observation of Effective Temperature of Ta Atom in Layer Compound TaS_2 by Neutron Resonance Absorption Spectromoter", Jap. J. Appl. Phys. **40**, 1504 - 1507 (2001).

[143] S. Ikeda, M. Misawa, S. Tomiyoshi, M. Omori and T. Suzuki, "Copper and oxygen vibrations in La_2CuO_4 and $YBa_2Cu_3O_7$", Phys. Lett. **134**, 191– 195 (1988).

[144] S. Baechler, B. Masschaele, P. Cauwels, M. Dierick, J. Jolie, T. Materna and W. Mondelaers, "The new cold neutron tomography set-up at SINQ", Nucl. Instr. Meth. Phys. Res. A **481**, 397 – 405 (2002).

[145] S. Baechler, N. Kardjilov, M. Dierick, J. Jolie, G. Kühne, E. Lehmann and T. Materna, "New features in cold neutron radiography and tomography Part I: thinner scintillators and a neutron velocity selector to improve spatial resolution", Nucl. Instr. Meth. Phys. Res. A **491**, 481 – 491 (2002).

[146] N. Kardjilov, S. Baechler, M. Bastürk, M. Dierick, J. Jolie, E. Lehmann, T. Materna, B. Schillinger and P. Vontobel, "New features in cold neutron radiography and tomography Part II: applied energy-selective neutron radiography and tomography", Nucl. Instr. Meth. Phys. Res. A **501**, 536 – 546 (2003).

[147] M.J. Gutmann, W, Kockelmann, L.C. Chapon and P.G.. Radaelli, "Phase imaging using time-of-flight neutron diffraction", J. Appl. Crystallogr. **39**, 82 – 89 (2006).

[148] A.S. Tremsin, J.B. McPhate, J.V. Vallerga, O.H.W. Siegmund, W.B. Feller, E. Lehmann and M. Dawson, "Improved efficiency of high resolution thermal and cold neutron imaging", Nucl. Instr. Meth. Phys. Res. A **628**, 415 – 418 (2011).

[149] A.S. Tremsin, J.B. McPhate, J.V. Vallerga, O.H.W. Siegmund, W.B. Feller, E. Lehmann, A. Kaestner, P. Boillat, T. Panzner and U. Filges, "Neutron radiography with sub-μm resolution through event centroiding", Nucl. Instr. Meth. Phys. Res. A **688**, 32 – 40 (2012).

[150] J.R. Santisteba, M.A. Vicente-Alvarez, P. Vizcaino, A.D. Banchik, S.C. Vogel, A.S. Tresmin, J.V. Vallerga, J.B. McPhate, E. Lehmann and W. Kockelmann, "Texture imaging of zirconium based components by total neutron cross-section experiments", J. Nucl. Mater. **425**, 218 – 227 (2012).

[151] E.M. Schooneveld, M. Tardocchi, G. Gorini, W. Kockelmann, T. Nakamura, E. Perelli Cippo, H. Postma, N.J. Rhodes, P. Schillebeeckx and the Ancient Charm collaboration, "A new position-sensitive transmission detector for epithermal neutron imaging", J, Phys. D:Appl. Phys. **42**, 152003 – 5 (2009).

[152] A.S. Tremsin, J.B. McPhate, J.V. Vallerga, O.H.W. Siegmund, J.S. Hull, W.B. Feller and E. Lehmann,"Detection efficiency, spatial and timing resolution of thermal and cold neutron counting MCP detectors", Nucl. Instr. Meth. Phys. Res. A **604**, 140 – 143 (2009).

[153] H. Sato, T. Kamiyama and Y. Kiyanagi, "Pulsed neutron imaging using resonance transmission spectroscopy", Nucl. Instr. Meth. Phys. Res. A **605**, 36 – 93 (2009).

[154] H. Sato, O. Takada, S. Satoh, T. Kamiyama and Y. Kiyanagi, "Development of material evaluation method by using a pulsed neutron transmission with pixel type detectors", Nucl. Instr. Meth. Phys. Res. A **623**, 597 – 599 (2010).

[155] T. Kai, M. Segawa, M. Ooi, E. Hashimoto, T. Shinohara, M. Harada, F. Maekawa, K. Oikawa, T. Sakai, M. Matsubayashi and M. Kureta, "First deomonstration of neutron resonance absorption imaging using a high-speed video camera in J-PARC", Nucl. Instr. Meth. Phys. Res. A **651**, 126 – 130 (2011).

[156] E. Perelli Cippo, A. Borella, G. Gorini, W. Kockelmann, M. Moxon, H. Postma, N.J. Rhodes, P. Schillebeeckx, E.M. Schooneveld, M. Tardocchi, K. Dusz, Z. Hajnal, K. Biro, S. Porcinai, C. Andreani and G. Festa, "Imaging of cultural heritage objects using neutron resonances", J. Anal. At. Spectrom. **26**, 992 – 999 (2011).

[157] A.S. Tremsin, J.B. McPhate, J.V. Vallerga, O.H.W. Siegmund, W. Kockelmann, E.M. Schooneveld, N.J. Rhodes and W.B. Feller, "High Resolution Neutron Resonance Adsorption Imaging at a Pulsed Neutron Beamline", IEEE Trans. Nucl. Sci. **59**, 3272 – 3277 (2013).

[158] A.S. Tremsin, S.C. Vogel, M. Mocko, M.A.M. Bourke, V. Yuan, R.O. Nelson, D.W. Brown and W.B. Feller, "Non-destructive studies of fuel pellets by neutron resonance absorption radiography and thermal neutron radiography", J. Nucl. Mater. **440**, 633 – 646 (2013).

[159] A.S. Tremsin, T. Shinohara, T. Kai, M. Ooi, T. Kamiyama, Y. Kiyanagi, Y. Shiota, J.B. McPhate, J.V. Vallerga, O.H.W. Siegmund and W.B. Feller,"Neutron resonance transmission spectroscopy with high spatial and energy resolution at the J-PARC pulsed neutron source", Nucl. Instr. Meth. Phys. Res. A **746**, 47 – 58 (2014).

[160] T. Kamiyama, H. Sato, N. Miyamoto, H. Iwasa, Y. Kiyanagi, and S. Ikeda, "Energy sliced neutron tomography using neutron resonance absorption spectrometer", Nucl. Instr. Meth. Phys. Res. A **600**, 107 – 110 (2009).

[161] H. Sato, T. Kamiyama, Y. Kiyanagi and S. Ikeda, "Simulation for resonance absorption spectroscopic tomography", Nucl. Instr. Meth. Phys. Res. A **600**, 135 – 138 (2009).

[162] T. Kamiyama, N. Miyamoto, S. Tomioka and T. Kozaki, "Epithermal Neutron Tomography using Compact Electron Linear Accelerator", Nucl. Instr. Meth. Phys. Res. A **605**, 91 – 94 (2009).

[163] H. Tsuchiya, H. Harada, M. Koizumu, F. Kitatani, J. Takamine, M. Kureta and H. Iimura, "A Monte Carlo simulation to study a design of a gamma-ray detector for neutron resonance densitometry", Nucl. Instr. Meth. Phys. Res. A **729**, 338 – 345 (2013).

[164] J.W. Sterbentz and D.L. Chichester, "Neutron resonance transmission analysis (NRTA): a nondestructive assay technique for the next generation safeguards initiative's plutonium assay challenge", Report INL/EXT-10-20620, Idaho National Laboratory, Idaho Falls, Idaho (2010).

[165] K. Shibata, O. Iwamoto, T. Nakagawa, N. Iwamoto, A. Ichihara, S. Kunieda, S. Chiba, K. Furutaka, N. Otuka, T. Ohsawa, T. Murata, H. Matsunobu, A. Zukeran, S. Kamada, J. Katakura,

"JENDL-4.0: A New Library for Nuclear Science and Engineering", J. Nucl. Sci. Technol. **48**, 1–30 (2011).

[166] L.C. Leal, H. Derrien, N.M. Larson, and R.Q. Wright, "R Matrix Analysis of ^{235}U Neutron Transmission and Cross Section in the Energy Range 0 to 2.25 keV", ORNL/TM-13516, Oak Ridge National Laboratory, Oak Ridge, Tenn. (1997).

[167] H. Derrien, L.C. Leal, N.M. Larson and A. Courcelle, "Neutron resonance parameters of ^{238}U and the calculated cross sections from Reich-Moore analysis of experimental data in the neutron energy range from 0 keV to 20 keV", ORNL/TM-2005/241, Oak Ridge National Laboratory, Oak Ridge, Tenn. (2005).

[168] H. Derrien, L.C. Leal, and N.M. Larson, "Neutron Resonance Parameters and Covariance Matrix of ^{239}Pu", ORNL/TM-2008/123, Oak Ridge National Laboratory, Oak Ridge, Tenn. (2008).

[169] T. Kase and H. Harada, "An Assessment of the Continuous Neutron Source Using a Low-Energy Electron Accelerator", Nucl. Sci. Eng. **126**, 59 - 70 (1997).

[170] S. Kopecky, P. Siegler and A. Moens, "Low energy transmission measurements of ^{240,242}Pu at GELINA and their impact on the capture width", Proc. Int. Conf. Nuclear Data for Science and Technology, Nice, France, April, 2007, pp. 623 – 626 (2007).

[171] W.B. Doub, "Particle Self-Shielding in Plates Loaded with Spherical Poison Particles", Nucl. Sci. Eng. **10**, 299 – 307 (1961).

[172] C.H. Randall, "Naval Reactor Physics Handbook", Vol. 1, A. Radkowsky (Ed.), Naval Reactors, Division of Reactor Development, United States Atomic Energy Commission (1964).

[173] M.M.R. Williams, "Random Processes in Nuclear Reactors", Pergamon Press Oxford New York Toronto Sydney (1974).

[174] R. Sanchez and G.C. Pomraning, "A statistical analysis of the double heterogeneity problem", Ann. Nucl. Energy **18**, 371 – 395 (1991).

[175] G.A. Titov, "Statistical Description of Radiation Transfer in Clouds", J. Atmos. Sci. **47**, 24 – 38 (1990).

[176] F. Malvagi, R.N. Byrne, G.C. Pomraning, R.C.J. Somerville, "Stochastic Radiative Transfer in Partially Cloudy Atmosphere", J. Atmos. Sci. **50**, 2146 – 2158 (1993).

[177] A. Marshak, A.B. Davis (Eds.). "3D Radiative Transfer in Cloudy Atmosphere. XII", 686 pp, Springer, Heidelberg, Germany (2005).

[178] P. Boissé, "Radiative transfer inside clumpy media: the penetration of UV photons inside molecular clouds", Astron. Astrophys. **228**, 483 – 502 (1990).

[179] M.P. Hobson and R. Padman, "Radiative Transfer in a Clumpy Medium - Part Two - the Mega-Grains Approximation for Two-Phase Models", Mon. Not. R. Astron. Soc. **264**, 161 – 164 (1993).

[180] C.D. Levermore, G.C. Pomraning, D.L. Sanzo, J. Wong, "Linear transport theory in a random medium", J. Math. Phys. **27**, 2526 – 2536 (1986).

[181] B. Becker, K. Kauwenberghs, S. Kopecky, H. Harada, M. Moxon, and P. Schillebeeckx, "Implementation of an analytical model accounting for sample inhomogeneities in REFIT", JRC Scientific and Policy Reports, JRC 86936, ISBN 978-92-79-35095-5 (2013).

[182] S. J. Plimpton, "Fast Parallel Algorithms for Short-Range Molecular Dynamics", J. Comp. Phys. **117**, 1 – 19 (1995).

[183] P. De Bièvre, H.L. Eschbach, R. Lesser, H. Meyer, J. Van Audenhove and B.S. Carpenter, "^{235}Uranium isotopic abundance certified reference material for gamma spectroscopy - EC nuclear reference material 171 certification report", Joint Research Centre Report COM 4153 (1985).

[184] B. Becker, H. Harada, K. Kauwenberghs, F. Kitatani, M. Koizumi, S. Kopecky, A. Moens, P. Schillebeeckx, G. Sibbens and H. Tsuchiya, "Particle Size Inhomogeneity Effect on Neutron Resonance Densitometry", ESARDA Bulletin **50**, 2 – 8 (2013).

[185] M. Sanati, R.C. Albers, T. Lookman and A. Saxena, "Elastic constants, phonon density of states, and thermal properties of UO_2", Phys. Rev. B **84**, 014116 – (2011).

[186] E. Dupont, private communication (2014).

[187] CSEWG-Collaboration, âĂIJEvaluated Nuclear Data File ENDF/B-VI.8âĂİ released in October 2001

[188] A. Trkov, R. Capote, I. Kodeli, L. Leal, "Evaluation of Tungsten Nuclear Reaction Data with Covariances", Nucl. Data Sheets **109**, 2905 – 2909 (2008).

[189] L. Leal, K. Guber, D. Wiarda, G. Arbanas, H. Derrien, R. Sayer, N. Larson and M. Dunn, "ORNL Resolved Resonance Covariance Generation for ENDF/B-VII.1", Nucl. Data Sheets **113**, 3101 – 3119 (2012)

[190] K. Shibata, T. Kawano, T. Nakagawa, O. Iwamoto, J. Katakura, T. Fukahori, S. Chiba, A. Hasegawa, T. Murata, H. Matsunobu, T. Ohsawa, Y. Nakajima, T. Yoshida, A. Zukeran, M. Kawai, M. Baba, M. Ishikawa, T. Asami, T. Watanabe, Y. Watanabe, M. Igashira, N. Yamamuro, H. Kitazawa, N. Yamano, H. Takano, "Japanese Evaluated Nuclear Data Library Version 3 Revision-3: JENDL-3.3", J. Nucl. Sci. Technol. **39**, 1125 – 1136 (2002).

[191] M.B. Chadwick, M. Herman, P. Obložinský et al., M.E. Dunn, Y. Danon, A.C. Kahler, D.L. Smith, B. Pritychenko, G. Arbanas, R. Arcilla, R. Brewer, D.A. Brown, R. Capote, A.D. Carlson, Y.S. Cho, H. Derrien, K. Guber, G.M. Hale, S. Hoblit, S. Holloway, T.D. Johnson, T. Kawano, B.C. Kiedrowski, H. Kim, S. Kunieda, N.M. Larson, L. Leal, J.P. Lestone, R.C. Little, E.A. McCutchan, R.E. MacFarlane, M. MacInnes, C.M. Mattoon, R.D. McKnight, S.F. Mughabghab, G.P.A. Nobre, G. Palmiotti, A. Palumbo, M.T. Pigni, V.G. Pronyaev, R.O. Sayer, A.A. Sonzogni, N.C. Summers, P. Talou, I.J. Thompson, A. Trkov, R.L. Vogt, S.C. van der Marck, A. Wallner, M.C. White, D. Wiarda, P.G. Young, "ENDF/B-VII.1 Nuclear Data for Science and Technology: Cross Sections, Covariances, Fission Product Yields and Decay Data", Nucl. Data Sheets **112**, 2887 – 2996 (2011).

[192] A. Brusegan, F. Corvi, P. Rullhusen, Z.N. Soroko, S.I. Sukhoruchkin, H. Weigmann, "Tables of Neutron Resonance Parameters", Landolt-Börnstein: Numerical Data and Functional Relationships in Science and Technology - New Series, Subvolume 16C, Subseries: Elementary Particles, Nuclei and Atoms, Supplement to Subvolume B, Springer-Verlag Berlin, Heidelberg New York, ISBN 978-3-540-42828-2 (2004)

[193] S.F Mughabghab and D.I. Garber, "Neutron Cross Sections", BNL 325 Report, Third edition, Volume 1, Brookhaven National Laboratory (1973).

[194] S.F Mughabghab, "Neutron Cross Sections", Volume 1 Academic Press, Inc., San Diego, ISBN: 0-12-509701-8 (1984).

[195] S.F Mughabghab, "Atlas of Neutron Resonances, 5th Edition", Elsevier Science, ISBN: 0-44-52035-X (2006).

European Commission
EUR 26848 EN – Joint Research Centre – Institute for Reference Materials and Measurements

Title: Neutron Resonance Spectroscopy for the Characterisation of Materials and Objects

Authors: P. Schillebeeckx, B. Becker, H. Harada, S. Kopecky

Luxembourg: Publications Office of the European Union

2014 – 64 pp. – 21.0 x 29.7 cm

EUR – Scientific and Technical Research series – ISSN 1831-9424 (online), ISSN 1018-5593 (print)

ISBN 978-92-79-41179-3 (PDF)
ISBN 978-92-79-41180-9 (print)

doi: 10.2787/98278

LA-NA-26848-EN-N

JRC Mission

As the Commission's in-house science service, the Joint Research Centre's mission is to provide EU policies with independent, evidence-based scientific and technical support throughout the whole policy cycle.

Working in close cooperation with policy Directorates-General, the JRC addresses key societal challenges while stimulating innovation through developing new methods, tools and standards, and sharing its know-how with the Member States, the scientific community and international partners.

Serving society
Stimulating innovation
Supporting legislation

doi: 10.2787/98278

ISBN 978-92-79-41179-3